CHARACTERIZATION OF THE INTERFACE BETWEEN DETONATION PRODUCT GASES AND AMBIENT AIR IN AN EXPLOSION

by

Christian Peterson

Submitted in Partial Fulfillment
of the Requirements for the Degree of
Doctor of Philosophy in Mechanical Engineering
with Dissertation in Intelligent Energetic Systems

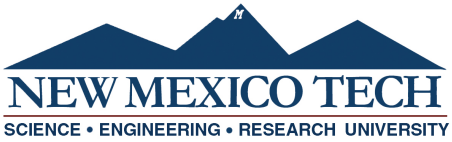

New Mexico Institute of Mining and Technology
Socorro, New Mexico
Jan, 2024

This thesis is dedicated to my family, who instilled in me the value of education for all endeavors.

Christian Peterson
New Mexico Institute of Mining and Technology
Jan, 2024

ABSTRACT

Characterization of the interface between detonation product gases and ambient air in an explosion is a complicated task due to turbulent mixing and the inherently three-dimensional expansion of the interface. This study aimed to quantify the evolution of the interface complexity and progression to turbulence as a temporally-varying fractal. Laboratory and field scale experiments were conducted to identify characteristics of an explosively driven gas cloud such as the growth as a function of time and the width of the mixing region during expansion. Experiments were conducted using several explosives in primarily spherical geometries.

In the laboratory-scale work, a shotgun primer was used to generate a repeatable explosively-driven gas cloud in varying confinement. High speed imaging captured the evolution of the product gas interface, and an automated image processing routine extracted and measured the mixing region width h. A comparison was made to a gas cloud radius based predictive model for the width of the mixing region, and a new scaling factor k was used to scale the equations for a non-zero start time. The fitting parameters c and k were found to vary with the degree of confinement as the experimental conditions diverged from the base assumptions of the model. No particular trends were found in the evolution of k, though for early times the geometric constraint c was seen to increase disproportionately with k as spacing increases. The model was also applied to mixing region growth on spherical explosive charges with known initial surface perturbations. It was found that the width of the mixing region is predicted by the analytical model at the initial stages of the blast, but transitions to non-linear turbulent mixing before the shock has detached from the fireball.

In laboratory and field-scale experiments, the Hausdorff or fractal dimension of two-dimensional slices of the explosively driven gas cloud was measured from multiple angles. Gas cloud profiles representing the contact surface were extracted using automated image processing algorithms. The Hausdorff dimension was estimated using a box counting algorithm on the extracted contours. Experiments were performed with charge mass variations to identify scaling for the Hausdorff dimension, as well as other fireball characteristics such as radius. The fractal dimension was found to not scale with shock scaling laws once the shock has detached from the fireball. Taken as a function of mixing region width, the fractal dimension was seen to begin increasing as the validity of the analytical models ends, indicating an increase in the non-linear turbulence that drives complexity on the surface of the fireball.

Keywords: mixing; explosive; turbulence; image processing

This dissertation is accepted on behalf of the faculty of the Institute by the following committee:

Michael Hargather

Academic and Research Advisor

Bin Lim

Tei Wei

Richard Sonnenfeld

I release this document to the New Mexico Institute of Mining and Technology.

Christian Peterson Nov 13, 2023

CONTENTS

LIST OF TABLES

LIST OF FIGURES

Figure **Page**

NOMENCLATURE

$< \epsilon >$	Mean energy dissipation
H_ω	Mean energy
Ω	Mean enstrophy
η	Perturbation size in the Plesset equations
γ	The ratio of specific heats
λ	Wavelength
ω	Vorticity
ρ	Density
ρ_0	Ambient air density
τ	Richtymer-Meshkov instability characteristic time
$\mathcal{A}$	Atwood number
C_0	Speed of sound
D_F	Hausdorff dimension
D_T	Topological dimension
E	Mean energy
E_{HE}	Total energy of high explosive
f	Spatial perturbation frequency for the C4 charges (rad/m)
H	Mean helicity
h	Mixing region thickness
h^*	Normalized mixing region width h/l_c
h_0	Mixing region thickness at time $t = 0$
l_c	Characteristic length
M_s	Shock wave Mach number

N	Fractal number
n	Refractive index
n_{mode}	Mode number
R	Radius
R^*	Scaled radius R/l_c
R_0	Radius at time $t = 0$
s	Fractal depth
t	Time after detonation
t^*	Scaled time after detonation t/t_c
t_c	Characteristic time
U	The shock velocity
$\mathbf{v}$	Velocity vector
W_0	Reference explosive weight
Y_n	The principal spherical harmonic describing the initial perturbation in Plesset's and Mikaelian's mixing region growth
Z	Explosive scaled distance
C4	Composition 4, a plastic bonded high explosive primarily composed of RDX
EoV	End of Validity
fps	Frames per second, a measurment of camera recording speed
HE	High explosive
PBX	Plastic Bonded Explosive
PETN	Pentaerythritol tetranitrate
RDX	Research Department Explosive, or 1,3,5-trinitroperhydro-1,3,5-triazine
RMI	Richtmyer-Meshkov Instability
RTI	Rayleigh-Taylor Instability
SoV	Start of Validity

CHAPTER 1

INTRODUCTION

1.1 Motivation

The interface between an explosively driven gas cloud and the ambient air behind a shock wave is a naturally complex and chaotic environment. Even in simplified planar environments such as shock tubes, the inherent complexity of the mixing process is a tremendous task for direct numerical simulation, and an area of vigorous study by experimentalists, computationalists, and theorists. A better understanding of how the mixing interfaces evolve with a scaling variable such as explosive charge mass is critical to developing a framework for an understanding of the process.

The transition of an explosively driven fireball from the smooth surface of expanding gas to the turbulent mixture of ambient air and cooling detonation products is a complicated three dimensional problem. The growth of turbulence, and therefore mixing, on the surface of a fireball is linked to the initial conditions of the fireball. Small initial imperfections in the surface of charges, non-uniformity in explosive composition, and slight differences in atmospheric conditions can impact the resultant mixing. The effort for analyzing the explosively driven mixing region evolution can be approached from three principal directions: the development of experimental diagnostics that can capture the desired quantities consistently; the application of existing models and theories to the data to identify areas for improvement; and the development of scaling parameters and tools to decouple the explosive mixing problem from specific circumstances and allow it to be applied more generally. This research is motivated by these approaches develop a scalable and dimensionless understanding of the interface evolution process. Two metrics, the mixing region width and the fractal dimension, were chosen to represent the interface evolution. The multi-scale nature of turbulent mixing is conducive to developing an understanding using fractals. The mixing width and fractal dimension can both be determined through direct imaging of the fireball surface. This is important, as a potential application for this research is the characterization of turbulent development from archival film of large scale explosions.

The purpose of this research is to characterize the relationship between turbulent mixing width and fractal dimension in the immediate post detonation environment. In support of that purpose, the development of diagnostic method-

ologies for identification of both mixing width and fractal dimension was required. The characterization of this relationship is intended to provide insight into the formation of surface instabilities on the fireball, and their growth towards turbulence. Connecting the change in fractal dimension to the existing explosive scaling laws is intended to give better understanding of what flow regimes can be characterized by the fractal dimension.

1.2 Turbulence and turbulent mixing

Big whirls have little whirls
that feed off their velocity
and little whirls have lesser whirls
and so on to viscosity

Lewis Fry Richardson [1]

The term turbulence is believed to have been coined by William Thomson in 1887, though it would not reach wide-spread adoption within the research community for the next 15 to 20 years [2]. In fact, in the classical turbulent research done by Osborne Reynolds, the term turbulence is not used [3]. However, nearly a century later, the field of turbulence continues to be a topic of significant scientific discussion. The high non-linearity of turbulent processes has long encouraged linearization and lower order modeling to make the complicated behavior more readily approachable for researchers and engineers alike.

Much of the study of turbulent events is the study of averages and bulk energies. The chaotic nature of a turbulent flow inhibits direct study of specific phenomena, and so research tools have been developed to characterize the turbulence in a certain flow averaged over time, space, or both. Time averaged flows are a common tool in computational fluid dynamics (CFD) to understand the generalized behavior of a system without the discussion devolving into specific cases of initial perturbation and geometry. An especially important characteristic value for a turbulent flow is the energy dissipation rate ϵ [4]. For turbulence, it is important to be aware of some notation. The angular brackets represent an average over the fundamental periodicity box. Vertical brackets represent the vector magnitude. Mean energy, E, and mean enstrophy, Ω are defined as:

$$E \equiv \langle 1/2|\mathbf{v}|^2 \rangle \tag{1.1}$$

$$\Omega \equiv \langle 1/2|\boldsymbol{\omega}|^2 \rangle \tag{1.2}$$

where $\mathbf{v}$ is the velocity vector, and $\boldsymbol{\omega}$ is the vorticity. Conservation of energy for the fluid flow can be written as:

$$\frac{\partial}{\partial t}E = 2\mathbf{v}\Omega \tag{1.3}$$

$$\frac{\partial}{\partial t}H = -2\mathbf{v}H_\omega \tag{1.4}$$

Where the mean energy dissipation ϵ is defined as:

$$\langle \epsilon \rangle \equiv -\frac{\mathrm{d}E}{\mathrm{d}t} \tag{1.5}$$

The energy dissipation is important because it provides a diagnostic number for the scales of turbulence in terms of the relative energy dissipation at each scale. The energy budget is proved on the basis of incompressibility. The underlying concepts addressed here are the injection of turbulent energy at large length scales, and dissipation of energy dominant at small scales. If energy is primarily being injected at large scales, and primarily being dissipated at small scales, there must exist some mechanism for the transfer of energy from the large scales to the small [1, 4]. Space mean measurements such as dissipation are important, as the complexity of turbulence frequently leads researchers to address turbulent behavior stochasticaly, despite the widely conjectured deterministic nature of the Navier-Stokes equations [4]. By treating turbulence as a stochastic system, a researcher derives certain benefits. The Ergodic theorem states that a time average along an orbit is equivalent to ensemble average, which justifies the use of bulk averaged terms in experimental assessments of turbulent mixing [5].

1.2.1 Early stage development of turbulent mixing

Of specific interest is how turbulence impacts the mixing of two fluids when the interface between them becomes perturbed. The mixing width is one way to characterize the evolution of that mixing. The importance of mixing width to characterizing the evolution of the mixing region comes from the study of mixing as the evolution of a surface perturbation, and is a common metric for the evaluation of linearized models [6–13]. The mixing width does not fully capture the evolution of smaller scale mixing that develop on larger length scale perturbations, but does describe the early evolution of those large perturbations [14]. Bell, in a 1951 Los Alamos technical report, derived equations for the evolution and growth of small amplitude perturbations under varying conditions and assumptions [6]. His equations, developed for both cylindrical (equation 1.6) and spherical (equation 1.7) geometries, related a perturbation size $\eta(t)$ to a radius R and a wavelength λ.

$$\lambda\eta\frac{\ddot{R}_0}{R_0} + \ddot{\eta} - \dot{\eta}\frac{\dot{\rho}}{\rho} = 0 \tag{1.6}$$

$$\eta\frac{\ddot{R}_0}{R_0} + \ddot{\eta} - \dot{\eta}\left(\frac{\dot{R}_0}{R_0} + \frac{\dot{\rho}}{\rho}\right) = 0 \tag{1.7}$$

Birkhoff published similar results in 1954 [15]. Of note is the assumption by Bell of the secondary fluid having negligible density [6]. The early work was

enhanced by Plesset, correcting an earlier error by Binnie, in a study of the stability analysis of work by G. I. Taylor [7, 10, 16]. The resulting Plesset equation and derivation serves as a basis for much of the current analytical models for turbulent mixing region growth in non-planar geometries.

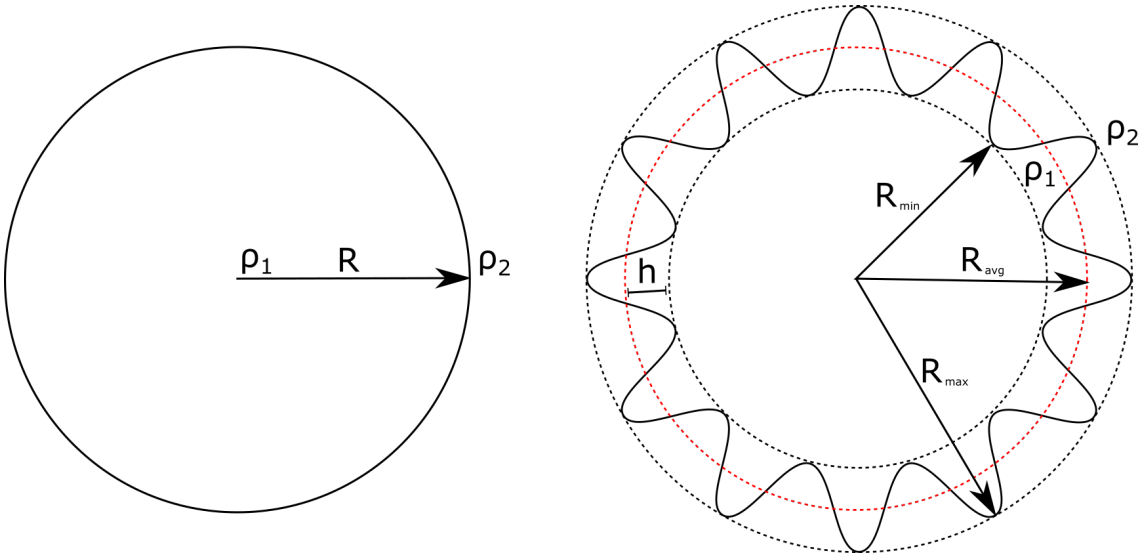

Figure 1.1: (left) A circular interface defined by radius R sparates the regions of density ρ_1 and ρ_2 and expands outward. (right) The portions of a perturbation moving in the direction of fluid acceleration are referred to as ”peaks”, while the “valleys” form against the direction acceleration. A perturbed surface may have the same nominal radius $r = r_{avg}$ with significant variation between the radii of valleys r_{min} and the radii of the peaks r_{max}. The difference between the peak or valley radii and the mean is the mixing region half-width h.

Derivation of the Plesset Equation The Plesset equations assume an incompressible, immiscible, non-viscous fluid in spherically symmetry [10]. A fluid of density ρ_1 in a radius R sphere is surrounded by another fluid of density ρ_2, such as the system seen in Figure 1.1. The origin of a spherical coordinate system is at the center of a spherical interface $R(t)$ that separates the two fluids. The velocity potential of the interface is given by

$$\varphi = \frac{R^2\dot{R}}{r} \tag{1.8}$$

This is a potential velocity field with radial velocity $-\frac{\partial\varphi}{\partial r}$. Consider a perturbation of the interface from $R(t)$ to r_s given by

$$r_s = R + \eta Y_n \tag{1.9}$$

where Y_n is a spherical harmonic of degree n and η is the amplitude of the harmonic and a function of time such that $|\eta(t)| \ll R(t)$, fulfilling the requirement that the disturbance is small relative to the radius of the sphere. By neglecting all terms in η higher than first order, the surface velocity in the radial direction u becomes

$$u = \dot{R} + \dot{\eta} Y_n \tag{1.10}$$

Across the interface, velocity must be continuous. The difference between normal surface velocity and radial velocity, however, is second order in η and is neglected. Choosing a perturbation to decrease away from the interface, the potential function for the flow is

$$\varphi_1 = \frac{R^2 \dot{R}}{r} + b_1 r^n Y_n \tag{1.11}$$

$$\varphi_2 = \frac{R^2 \dot{R}}{r} + b_2 \frac{Y_n}{r^{n+1}} \tag{1.12}$$

where b_1 and b_2 are constants that can be solved for by the requirement that the radial velocity at the interface is that given by Equation 1.10:

$$-\left(\frac{\partial \varphi_1}{\partial r}\right)_{r_s} = -\left(\frac{\partial \varphi_2}{\partial r}\right)_{r_s} = \dot{R} + \dot{\eta} Y_n \tag{1.13}$$

$$\varphi_1 = \frac{R^2 \dot{R}}{r} - \frac{r^n}{n R^{n-1}} Y_n \left[\dot{\eta} + 2\eta \frac{\dot{R}}{R}\right] \tag{1.14}$$

$$\varphi_2 = \frac{R^2 \dot{R}}{r} + \frac{R^{n+2}}{(n+1) r^{n+1}} Y_n \left[\dot{\eta} + 2\eta \frac{\dot{R}}{R}\right] \tag{1.15}$$

The Bernoulli integral is used to determine the pressure on both sides of the interface p_1 and p_2.

$$\int \frac{dp}{\rho} = \frac{\partial \varphi}{\partial t} - \frac{1}{2} |\boldsymbol{\nabla} \varphi|^2 + u + f(t) \tag{1.16}$$

$$p_1 = P_1(t) + \rho_1 \left[\left(\frac{\partial \varphi_1}{\partial t}\right)_{r_s} - 1/2 (\nabla \varphi_1)^2_{r_s}\right] \tag{1.17}$$

$$p_2 = P_2(t) + \rho_2 \left[\left(\frac{\partial \varphi_2}{\partial t}\right)_{r_s} - 1/2 (\nabla \varphi_2)^2_{r_s}\right] \tag{1.18}$$

Where $P_1(t)$ and $P_2(t)$ are spatial integration constants resulting from Equation 1.16. In Plesset's derivation, it is noted that $P_2(t)$ is the pressure at infinity. The components of Equations 1.17 and 1.18 are found to the first order:

$$\left(\frac{\partial \varphi_1}{\partial t}\right)_{r_s} = \frac{1}{R} \frac{\mathrm{d}}{\mathrm{d}t} \left(R^2 \dot{r}\right) - \frac{\eta Y_n}{R^2} \frac{\mathrm{d}}{\mathrm{d}t} \left(R^2 \dot{R}\right) - \frac{\ddot{\eta}}{n} R Y_n + \frac{n-3}{n} \dot{\eta} \dot{R} Y_n - \frac{2\eta}{n} \left(\ddot{R}\right) Y_n + \frac{2\eta \dot{R}^2}{R} Y_n \tag{1.19}$$

$$\left(\frac{\partial \varphi_2}{\partial t}\right)_{r_s} = \frac{1}{R}\frac{\mathrm{d}}{\mathrm{d}t}\left(R^2\dot{r}\right) - \frac{\eta Y_n}{R^2}\frac{\mathrm{d}}{\mathrm{d}t}\left(R^2\dot{R}\right) + \frac{\ddot{\eta}}{n+1}RY_n + \frac{n+4}{n+1}\dot{\eta}\dot{R}Y_n + \frac{2\eta}{n+1}\left(\ddot{R}\right)Y_n + \frac{2\eta\dot{R}^2}{R}Y_n \quad (1.20)$$

$$\left(\boldsymbol{\nabla}\varphi_1\right)^2 \approx \left(\boldsymbol{\nabla}\varphi_2\right)^2 \approx \dot{R}^2 + 2\dot{\eta}\dot{R}Y_n \quad (1.21)$$

The two pressures are joined by surface tension σ

$$p_2 = p_1 - \sigma(1/R' + 1/R'') \quad (1.22)$$

where R'' and R' are principal radii of curvature of the interface. Combining and reducing to the first order terms this becomes

$$p_2 = p_1 - \frac{2\sigma}{R} - \frac{(n-1)(n+2)}{R^2}\sigma\eta Y_n \quad (1.23)$$

Using Equation 1.23 to join Equations 1.17 and 1.18, plugging in values from Equations 1.19, 1.20, and 1.21, then simplifying gives

$$R\ddot{R} + 3/2\dot{R}^2 = \frac{P_1(t) - P_2(t) - \frac{2\sigma}{R}}{\rho_2 - \rho_1} + Y_n\left[\ddot{\eta} + \left(\frac{3\dot{R}}{R}\right)\dot{\eta} - A\eta\right] \quad (1.24)$$

Grouping the terms proportional to Y_n, the resulting differential equation describes the perturbation growth $\eta(t)$

$$\ddot{\eta} + 3\frac{\dot{R}}{R}\dot{\eta} - A\eta = 0 \quad (1.25)$$

where

$$A = \frac{\left[n(n-1)\rho_2 - (n+1)(n+2)\rho_1\right]\ddot{R} - n(n-1)(n+1)(n+2)\sigma/R^2}{R\left[n\rho_2 + (n+1)\rho_1\right]} \quad (1.26)$$

It is worth remembering that the Plesset equations are not based in first principals, and the mixing width equations developed using its approach are ultimately models for the underlying behavior.

The Mikaelian Model The Plesset equations form the basis of the azimuthal model developed by Mikaelian, again separately for cylindrical (equation 1.33) and spherical (equation 1.32) geometries [8, 9]. Mikaelian restated Equation 1.25 as

$$\frac{\partial^2\eta}{\partial t^2} + 3\frac{\dot{R}}{R}\frac{\partial\eta}{\partial t} - nA(n)\frac{\ddot{R}}{R}\eta = 0 \quad (1.27)$$

Where, after taking the surface tension σ to be zero,

$$nA(n) = \frac{n(n-1)\rho_2 - (n+1)(n+2)\rho_1}{n\rho_2 + (n+1)\rho_1} \tag{1.28}$$

Equation 1.27 can be written as

$$\frac{1}{R^3}\left[R^3\frac{\mathrm{d}\eta}{\mathrm{d}t}\right] - nA(n)\frac{\dot{R}}{R}\eta = 0 \tag{1.29}$$

Again, a two fluid system is assumed, such as detonation products impinging into air. It is then assumed that Plesset's equation represents the growth of the mixing region width h after taking the limit

$$n \to \infty, \quad \eta \to 0, \quad \frac{n\eta}{R} \to c = constant \tag{1.30}$$

which yields

$$\frac{1}{R^3}\frac{\mathrm{d}}{\mathrm{d}t}\left[R^3\frac{\mathrm{d}h}{\mathrm{d}t}\right] - c\mathcal{A}\ddot{R} = 0 \tag{1.31}$$

Where $\mathcal{A}$ is the Atwood number. No assumptions are placed on the history of R. By integrating with respect to time, the mixing region thickness $h(t)$ can be found explicitly given a time history of the radius $R(t)$ for spherical geometries:

$$h(t) = h(0) + R_0^3\frac{\mathrm{d}h_0}{\mathrm{d}t}\int_0^t \frac{dt}{R^3} + c\mathcal{A}\int_0^t\left(\frac{1}{R^3}\int_0^t R^3\ddot{R}dt'\right)dt \tag{1.32}$$

Figure 1.1 demonstrates the features on an evolving perturbation that are used to identify the mixing region. Using a similar derivation, the mixing region thickness for a cylindrical geometry can be shown to follow a similar form [9]:

$$h(t) = h(0) + R_0^2\frac{\mathrm{d}h_0}{\mathrm{d}t}\int_0^t \frac{dt}{R^2} + c\mathcal{A}\int_0^t\left(\frac{1}{R^2}\int_0^t R^2\ddot{R}dt'\right)dt \tag{1.33}$$

Mikaelian's results were compared to simulations, and found to have good agreement with ideal case scenarios. However, the limitations of an azimuthal only model are significant for real world applications. Lombardini and Pullin derived an expression for the asymptotic growth rate for the combination of axial and azimuthal perturbations, which returns the Mikaelian equations in addition to Richtmyer's model for perturbation growth on a plane in the limiting cases [17].

In further analyses, Mikaelian investigated the constant acceleration Rayleigh-Taylor instability (RTI) case and the impulsively driven Richtmyer-Meshkov instablity (RMI) case and derived analytical expressions for mixing region thickness as expressions of time. The expressions so derived only require a given Atwood number, initial perturbation, and assumed radius history based on the chosen instability. As expansions of Bell's work, the base assumptions of irrotational flow

and a small initial amplitude are continued. Additionally, the tuning parameter c has been postulated to act as a geometric constant [9].

The topic of perturbation growth rate is critical to the development of a mixing region, as the perturbation is the basis for the classical instabilities that drive mixing, particularly for the RTI and RMI. Both instabilities exists on the interface between two fluids of differing densities, and form characteristic spike and bubble flow features that drive the mixing. These two instabilities share significant features, but the differentiating factor is the driving force behind their growth. The RTI instability occurs when a less dense fluid is accelerated into a denser fluid [11]. The classical example is a layer of water suspended above a layer of oil, where mixing results from the unstable equilibrium of the buoyancy forces once a perfectly planar interface is perturbed. RMI, on the other hand, arises from an impulsive or shock acceleration of two fluids [12]. RMI is less naturally common, as shock acceleration of a fluid interface is relatively infrequent on Earth. However, inertial confinement fusion sees significant RMI growth in the fuel layer, as does the study of supernova formation [18–20]. Of importance to RMI is that it is density gradient agnostic, and will form regardless of whether or not the impulsive acceleration is going from a less dense to more a dense fluid, or vice versa [21].

The dominant instability that drives mixing on the surface of a fireball is not constant with time. After the detonation wave passes through the interface, the surface of the rapidly expanding product gas cloud is RT unstable [22]. After the initial expansion, the secondary shock passes through the interface, driving the formation of RM features on the existing RT structures.

1.2.2 Other models and methods for mixing region and instability growth

The growth of RMI amplitude is the subject of experimental and theoretical work. Richtmyer, as part of his impulse model for the instability[12], proposed a growth rate that connected the post shock perturbation amplitude h to the initial post shock size h_0^+,the wave number k, the change in velocity across the shock Δu, and the post-shock Atwood number $\mathcal{A}^+$.

$$\frac{\mathrm{d}h}{\mathrm{d}t} = k\Delta u \mathcal{A}^+ h_0^+ \tag{1.34}$$

This equation does not take into account any pre-shock conditions, which has been found in experiments to not always be an accurate approach. In an early hydrocode simulation of the instability, it was found that the fit could be improved by taking the mean of the shocked and unshocked initial amplitudes h_0^- and h_0^+ [23]. The impulsive model for RMI is only valid for when the behavior of the interface remains approximately linear [24]. This is true for perturbations that remain small relative to their wavelength ($\eta(t) << \lambda$). Some early results studied flows outside of the linear regime using linear models, and observed poor

agreement between data and prediction. When working with very early time growth, or with very strong shocks, use of a linearized model will likely produce disappointing results [24].

The evolution of the interface between the explosive product gases and the ambient air behind the shock is dominated by the development of instabilities on the initial interface. Work on the three-dimensional instabilities is driven by study of supernova formation and inertial confinement methods [19, 25]. As such, the bulk of the experimental literature is focused on the implosion case, where an external shock source collapses into a central body of different density gas. The primary instabilities typically investigated in the context of explosively driven events are the RTI and RMI [26]. Research on this area has made significant use of simulation to investigate the growth rates of the instabilities, though there have been recent advances in the analytical theory for RMI [27]. The high computational cost of direct numerical simulation (DNS), combined with the difficulties of numerical artifacts when working with the near instantaneous discontinuity of a shock wave, has meant that significant amounts of computational resources have been committed to the study of RMI and RTI [28, 29].

In an effort to improve the baseline understanding of the mechanisms behind RMI, analytical models with modifications on existing one-dimensional models to approximate multidimensional effects have been validated against simulation [25]. Other one-dimensional models have been developed to study the evolution of the shock front in shock driven multi-phase mixing, and integrated varying temperature and velocity in the two mixing fluids [30]. Research suggests that even one-dimensional models with components of multidimensional effects will have significant differences from two-dimensional (2D) hydrodynamic models [19], which is of importance to three dimensional events like explosively driven gas clouds. The impact of those three dimensional effects were found to cause the growth of RT instabilities on spherically expanding clouds to vary from the classical instability when accounted for in one-dimensional models [31, 32]. The proposed parallel between planar and spherical instability growth, linking the volume of the perturbed fluid to the growth rate [17], has primarily been compared to resolved numerical simulations of the implosion case. As model complexity increases, so too does the difficulty found in applying that model to experimental data. More complicated analytical models have been developed to segment shock driven mixing into time scales based on characteristic time scales of differing wave number turbulent lengths scales [33]. These models begin to bridge the gap between the impulsive linear theory of RTI and a full direct numerical simulation of the instability, but are too complex for expedient analytical manipulation. While important, this work does not negate the need for experimental studies on non-planar geometries, despite the difficulties in replicating ideal analytical and model conditions in experimental testing [34].

1.2.3 Experimental methods

Experimental studies frequently utilize shock tubes to generate planar gas interfaces for ease of analysis and comparison [35]. Proper shock tube design is critical to achieve usable RTI results. Shock waves generated by a shock tube differ fundamentally from a shock wave generated by a gaseous explosive due to the lack of a Taylor expansion wave trailing the shock in shock tube studies, which transitions the already generated RMI to an RTI regime [24]. Figure 1.2.3 shows a schematic wave diagram for both a shock tube and an idealized spherical detonation [22]. The time period of interest in a shock tube is the time between initial shock interaction and re-shock by the reflection of the initial shock off the end of the tube. In a spherical detonation, the re-shock occurs when the secondary shock wave formed from the end of the Taylor expansion wave due to the rapid expansion of the detonation products passes through the expanding gas cloud and interacts with the contact surface [36].

Establishing well characterized initial perturbation is also critical, and the method of perturbation establishment is an important functional component of shock tube design. The ability to tightly control initial surface perturbations differentiates shock tube testing from the explosively driven interface of a product gas cloud or "fireball". Some experiments have been conducted attempting to replicate the clean shock tube environment using pressurized spheres, but control over initial perturbations in these tests is limited [37].

The diagnostics applied to RMI and RTI experiments endeavor to establish two primary components: the location and complexity of the interface, and the necessary thermodynamic flow properties to establish the state of the system. In shock tubes, techniques such as Planar Laser Induced Fluorescence(PLIF), two-dimensional (2D) and three-dimensional (3D) particle image velocimetry (PIV), and other flow seeding methods are popular, as the controlled environment of a shock tube enables good seeding and even distribution [24]. For non-planar testing, such as in an explosively driven gas cloud, direct imaging and refractive imaging techniques remain popular, with recent developments in high speed tomography showing promise for future work [38]. The integrated nature of refractive imaging techniques does typically limit their application to bulk averaged diagnostics.

The cascade of energy down the turbulent length scales, which can cover numerous orders of magnitude, makes the turbulent flow an inviting area for the application of fractal analysis [39]. Identification of traceable scalars within flows is a continuing challenge for researchers, with many experimentalists using dye doped flows [40], fluorescent gases [35], or just relying and simulation results [41].

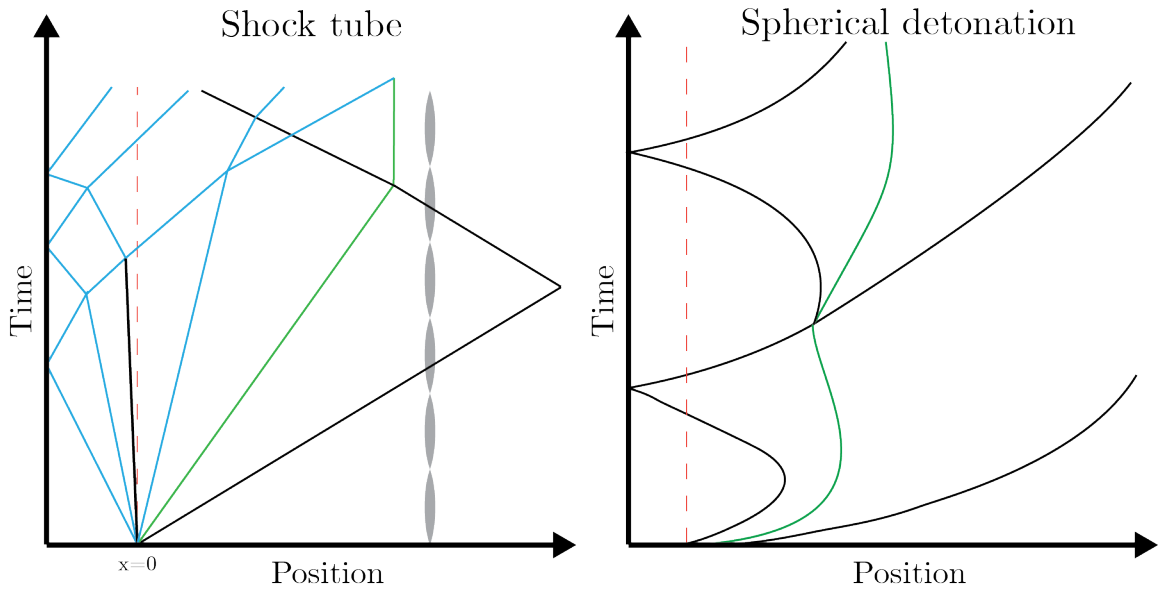

Figure 1.2: The wave diagram of a shock tube (left) compared to a spherical explosion (right) highlights the major differences between the behaviors of the shock waves (solid black), and the contact surfaces (solid green). In a shock tube, the studied interface (grey), is external to the shock producing gas, whereas in the spherical explosion the region of interest is the contact surface. In the shock tube the rarefaction waves (blue) traveling back into the driver section can also impact late time diagnostics. The over-expansion of the gas near the center of the blast in a spherical detonation causes the expansion waves to coalesce into a secondary shock wave, seen here turning towards the origin.

1.3 Fractals

Fractals provide a workable new middle ground between the excessive geometric order of euclid and the geometric chaos of roughness and fragmentation.

- Benoit Mandelbrot [42]

A fractal is a shape whose features, be they roughness or splintering, do not vary under a symmetry of dilation or contraction. The field of fractal geometry is a relatively fresh one for the field of mathematics, formalized by B. B. Mandelbrot in his work *The Fractal Geometry of Nature* [42]. While the description may seem far distant from any description of reality, natural patterns are frequently seen to be simply described by fractal expressions such as the appearance of broccoli, the organization of river networks, or the dynamics of a heart beat[43–45]. The basic concept of a mathematical fractal may be interpreted as a measure of complexity, and a measure of the rate at which larger length scales devolve to and are consumed by small scale motion.

A critical component for the use of fractals as a scientific tool is the fractal dimension, most commonly characterized as the Hausdorff dimension D_F. These two terms will be used interchangeably here. When dimensionality is discussed, it is typically in the form of the positive integers of topological dimension D_T, i.e., 1 dimensional model, 2 dimensional image, 3 dimensional reconstruction. A fractal however, is best described by a dimension in the space between the integers. If $D_F > D_T$, then by definition the set is a fractal. The Hausdorff fractal dimension is calculated by:

$$D_F = \frac{\ln N}{\ln s} \tag{1.35}$$

From a generalized view, N is the number of characteristics at a certain level of a fractal, while s is the "depth" of a fractal. More practically, N is a measure of length or size, and $1/s$ is the scaling ratio associated with that length. The quintessential fractal is the Koch curve, a continuously subdividing triangle that serves as a simple visual introduction to the concepts. Figure 1.3 shows the generation of a Koch curve. This process, repeated to infinity, is the basis of mathematical fractals. The Koch curve is a very simple fractal with a defined mathematical formula for it's constructions. As such, it's fractal dimension can be exactly calculated $D_{Koch} = \frac{\ln 4}{\ln 3} = 1.26$. Natural fractals rarely have exact mathematical constructions, and so must rely on varying methods of fractal dimension estimation.

Box counting, or the generalized dimension, estimates the fractal dimension by determining the space filling capabilities of a set [46, 47]. Box counting, taken to the limit of box size $s \to 0$ determines the Minkowski-Bouligand dimension, which in standard use is equivalent to the Hausdorff dimension. However,

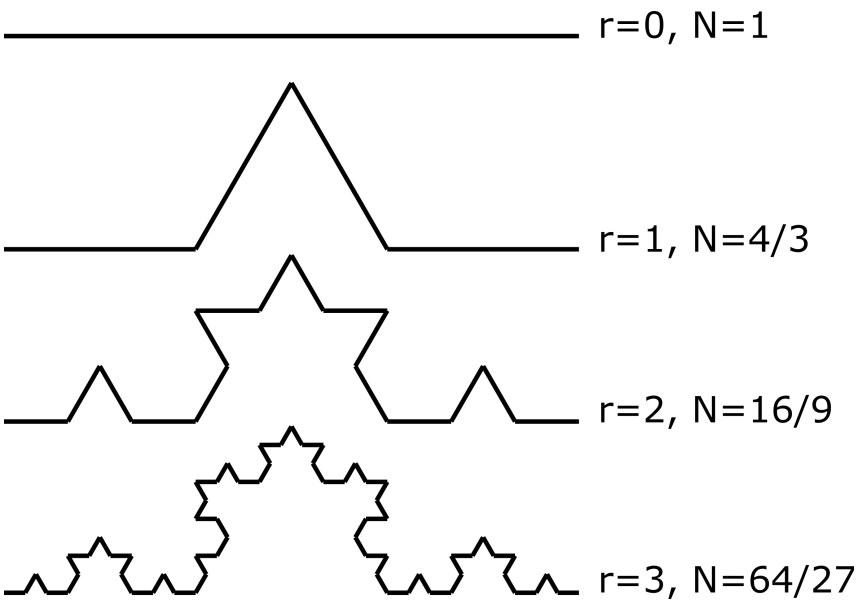

Figure 1.3: The first 4 steps to the generation of the Koch Curve, where r is the refinement level, and N is the normalized length of the curve. The top row is the basis object, in this case a flat line. The second step shows the generator function, where a straight line is broken into 4 lines of length 1/3 of the original line. The generator is then recursively applied to all straight lines, creating the increasingly complex objects on lines 3 and 4. As r increases, the total length also increases, demonstrating the property that fractals change length depending on the precision of the tool measuring them.

in cases where it is not equivilant to the Hausdorf dimension, the Minkowski-Boulingand dimension obeys the strict inequality

$$D_F \leq D_{L,BC} \leq D_{U,BC}$$

where $D_{L,BC}$ and $D_{U,BC}$ are the upper and lower limits of the box counting dimension [48]. This methodology translates well to digital images, where information is inherently quantized along pixel divisions [49]. Efficient box counting algorithms for digital images are available for images of many types, and fractal dimension estimation is typically a robust component of a fractal analysis framework [50].

Fractals in turbulence Fractals have been speculated to have some application in the realm of turbulence [42]. The lack of any clear scale in a turbulent flow encourages the postulation that the scales of turbulent eddies can be better described using that language of fractals. Turbulent systems are stochastically chaotic, and the fractal dimension has a history of being applied to understand chaotic systems [47]. Attempts have been made to describe the turbulent mixing of gases using a fractal model, and have seen some success in determining a point of convergence for the Hausdorff dimension of a mixing layer [35, 40]. Several studies have arrived at a values of 1.36 to 1.3 for the evolution of the isosurfaces in the mixing region on a slice of a jet flow imaged by PLIF [35, 51]. The mathematical theory for 3D turbulence predicts a Hausdorff dimension or $5/2$ or $8/3$ for nonpersistent and antipersistent turbulence [42]. Historically many aspects of turbulence have been approached through a fractal lens [52]. These surfaces are difficult to measure, experimentally in a turbulent environment, and several techniques have been developed to optically approximate them [35, 40, 53, 54]. Successful measurement of the fractal dimension of an evolving surface using optical diagnostics has been made in a shock tube [35, 53]. Ng et. al. determined that the interface between a block of SF6 trended towards a fractal dimension of 1.39 when driven by a shock to RMI [53]. Several studies have arrived at a value of $4/3$ for the evolution of the isosurfaces in the mixing region on a slice of the flow imaged by PLIF [40].

Current research has attempted to address other facets of the fractal nature of turbulent structures, such as the evolution of a turbulent mixing flow generated via a fractally refined grid [55]. The determination of fractal dimension for a turbulent flow is greatly dependent on the fractal dimension of the chosen scalar metric, and is an area of continued development [40, 41, 56, 57].

For energetic and combusting flows, there is precedent for the application of the Hausdorff dimension for the analysis of flame front growth both in classical turbulence [57] and in analysis of gas cloud explosions [41]. Bambauer et. al. has continued the application of fractal dimension to gas cloud explosions, working with simulations of H_2/air mixtures and measuring the Hausdorff dimension of the flame surface to identify dependencies of the Hausdorff dimension on fuel

air mixture [58]. The indication is that the flame front surface evolution, as represented by the Hausdorff dimension, is dependent on the energy release in the combustion process. Recent work by Gomez et. al. studied the fractal dimension of the early time detonation products in a blast chamber, and concluded the fractal behavior was asymptotic, converging towards a Hausdorff dimension $D_F \approx 1.9$ [54]. The Hausdorff dimension extracted by Gomez et. al. is estimated with respect to the occluded area of the product gases, not solely the boundary of the flow. The fractal dimension of a shock accelerated particle interface was studied by Rodriguez et. al. [59]. They found that the particle interface asymptotically approached a value of 1.4 as the surface instabilities drove the mixing of the particle cloud into turbulence. Ouellet et. al. simulated a similar experimental configuration to to Rodriguez et. al., and identified a convergent Hausdorff dimension of 1.6 for uniform particulate packing [60]. However, the Hausdorff dimension of perturbed particle packings, where lower volume fraction particle packings where introduced, a lower fractal dimension was observed, converging to between 1.1 and 1.2. The previous work has emphasized the shock acceleration of particles to create Richtmyer-Meshkov instabilities. Gomez et. al. began to address the direct fractal dimension of the explosive product gases, but did not study the effects of initial perturbations on the surface of the charges. The present work seeks to study the fractal evolution of the detonation product gas interface as it initially evolves in order to characterize the development of multi-scale mixing during early time evolution.

1.4 Refractive imaging

Seeing is understanding

Ernest Mach

In order to capture the fluid dynamics occurring in the region around a detonation, imaging techniques that can visualize the changes in air density around an explosion are used. These refractive imaging techniques provide additional information about the state of the flow near the expanding fireball that is not readily recoverable by direct imaging alone. Throughout this research, techniques such as schlieren photography, shadowgraphy, and background oriented schlieren have all been used to identify features in and around the expanding fireball.

1.4.1 Schlieren

Schlieren imaging is a refractive imaging technique that captures changes in refractive index along the path of a light beam [61]. The basic schlieren technique

gathers light from a point or approximately point source and directs it through a collimating optic, typically a parabolic mirror or plano-convex lens. The collimated light passes through the test section before entering another optic that refocuses the light down to a point. A cutoff, typically a razor blade, is placed at the focal point in such a manner to obscure a portion of the point. Passing the cutoff, the light goes into the camera. A diagram of a typical schlieren system is seen in Figure 1.4. Schlieren images the first derivative of the refractive index, n, which is related to the density, ρ, of a gas via the Gladstone-Dale law [62]:

$$\frac{n-1}{\rho} = \text{constant} \tag{1.36}$$

The direction of the derivative is controlled by the orientation of the cutoff, with the derivative imaged being perpendicular to the cutoff blade. The schlieren technique refers specifically to the use of the cutoff, so while the collimated method is the most common, it is not the only way to construct a schlieren system.

Schlieren is frequently used for the detection and tracking of density variations in a gas, either from pressure [63] and temperature [64] variation or from differing gas species [65]. A significant advantage of the technique is the high light efficiency, allowing extremely fast camera shutter speeds and frame rates while retaining sufficient illumination for imaging. To maximize the field of view available, collimating lenses are commonly used, but the field view of an imaging system is still limited by the size of the optics available [66]. Using symmetry assumptions, quantitative information about density can be extracted from a calibrated schlieren image [67].

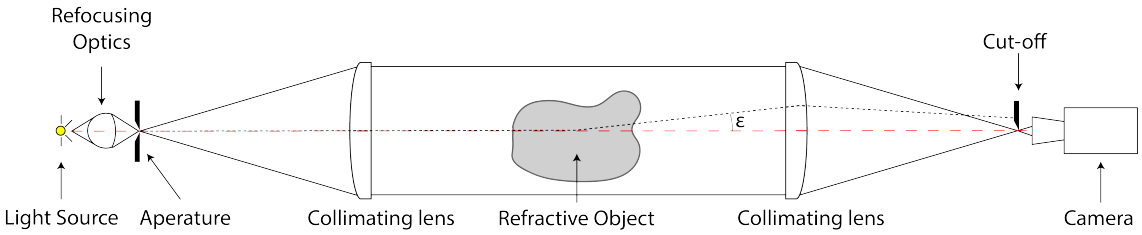

Figure 1.4: Line diagram of a typical lens based schlieren system. The light is emitted at the source and refocused onto an apperature to achieve a small point size. The light is then collimated by a lens, typically a large plano-convex achromat. The collimated light passes through the test section and is refocused by another plano-convex achromat. Light that passes through a change in refractive index is deflected, and enters the refocusing optic at an angle. The refocused light passes by a knife edge cut-off at the focal point, blocking light that has been deflected towards the knife edge. The light is then focused onto a camera sensor, producing a schlieren image.

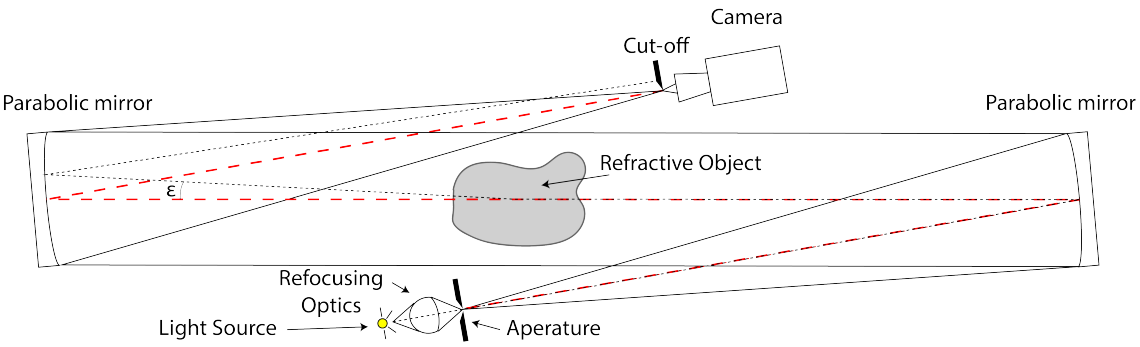

Figure 1.5: Line diagram of a typical Z-type schlieren system using parabolic mirrors. The light path is very similar to that described in Figure 1.4. The principal differences are the collimating optics being mirrors, and the offset angle of the light source and cameras. Because mirrors "fold" the system, short systems can be achieved with very high focal lengths, which is critical for large diameter optics.

1.4.2 Shadowgraphy

Shadowgraphy is a related technique that uses the same collimated light setup, but without the cutoff [68]. Instead of imaging the first derivative of refractive index, shadowgraph photography images the Laplacian for the refractive index field [66]. The primary impact of the this difference is the removal of the directional component from schlieren, which makes numerically reversing the process impossible. However, because shadowgraphy shows gradients free of directional information, it detects gas boundaries regardless of orientation, which is beneficial for imaging the complicated structures found in turbulent mixing. Figure 1.6 shows a shadowgraph system and example image. Much like schlieren, variations of shadowgraphy exist that do not rely on collimated light. In particular, retroreflective shadowgraph utilizes a light source super-imposed on a camera in conjunction with a retroreflective screen to achieve high light transmission without large collimating optics [69].

In application, shadowgraphy is more versatile than schlieren due to the lower difficulty in setup. As the Laplacian is not invertible, shadowgraphy is typically a qualitative diagnostic for gas dynamics. The imaging typically thickens sharp discontinuities to a greater degree than schlieren which can smudge out fine detail.

1.4.3 Background oriented schlieren

Background oriented schlieren (BOS) is an imaging method that utilizes computational post processing to identify the displacement of a background in an

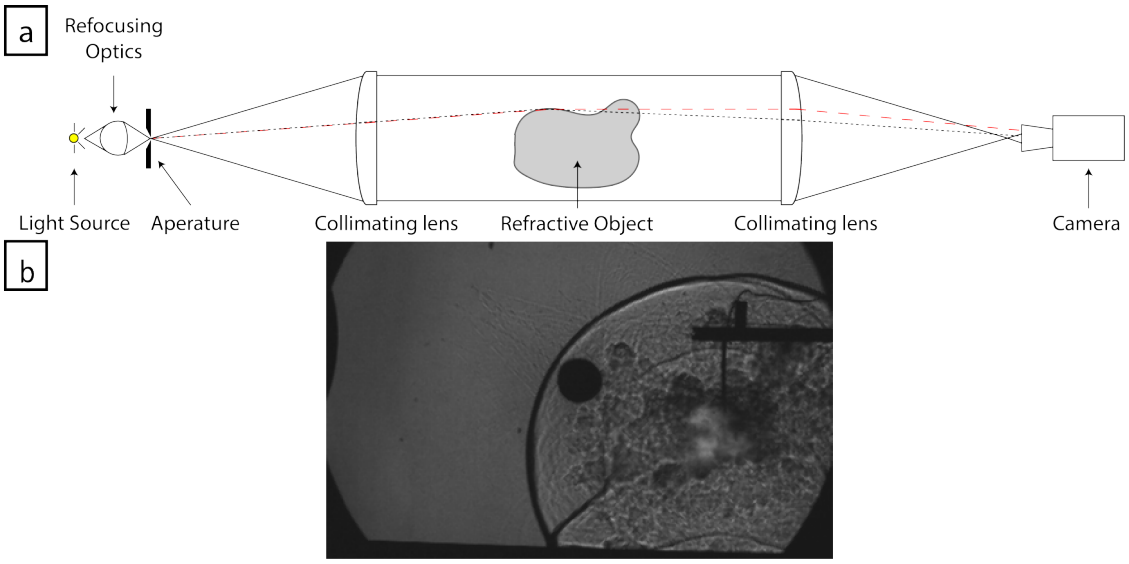

Figure 1.6: (a) A schematic of a collimated shadowgraph system. The refractive object casts a physical shadow onto the camera sensor. (b) A representative collimated shadow graph image. Note the strong demarcation of the shock location, as well as the omni-directional detection of the shock, in contrast to the directional nature of schlieren.

image to identify changes in refractive index on a large scale. BOS has been famously applied by NASA for capturing shock waves of supersonic planes in flight [70]. BOS is not reliant on collimated light, so can scale indefinitely as long as the resolution of the imaging device is sufficient [71]. The algorithms applied to generate BOS images can come from two primary lineages, optical flow algorithms and correlation based algorithms [38, 71]. For direct imaging of fireballs, BOS is a useful technique for the timing of shock interactions with the fireball surface.

1.5 Image processing

You don't take a photograph, you make it.

Ansel Adams

The advent of the digital high speed camera has significantly changed the field of high resolution photographic diagnostics. With cameras capable of frame rates in excess of 1 million frames per second (Mfps), and sensor resolutions in the megapixel range, the barrier to high quality scientific imaging has been significantly lowered. That being said, there are still significant challenges with the application of high speed cameras to turbulence research.

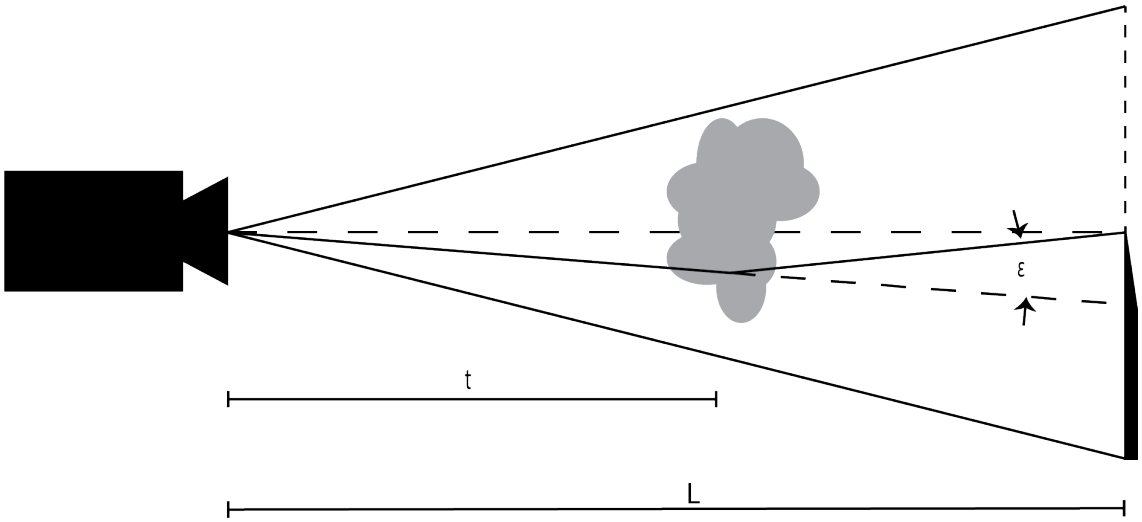

Figure 1.7: A line diagram of BOS. BOS scales well with increasing event size, but is reliant on post processing to accurately identify flow features and changes in refractive index.

1.5.1 Edge detection and image segmentation

The successful detection and characterization of edges is critical to the identification of a gas cloud interface from high speed photography. Edge detection algorithms vary from relatively simple derivative filters to detailed algorithms. Canny edge detection uses a series of thresholds and filters to identify and connect edges of different characters and forms while rejecting background noise and information [72]. The Canny algorithm is a 4 step process:

1. Low-pass Gaussian filtering is applied to the base image to reduce noise. The appropriate size of the filter is context dependent. Here, x and y are the horizontal and vertical distance respectively from the given center pixel.

$$G(x) = \frac{1}{\sqrt{2\pi\sigma^2}} \exp\left\{ -\frac{x^2 + y^2}{2\sigma^2} \right\} \tag{1.37}$$

2. The image is convolved with a derivative of the Gaussian filter from step 1, giving image gradients I_x and I_y.

3. Non-edge pixels are rejected by identifying values with very low derivatives.

4. A two stage filtering process is applied to identify two categories: strong and weak edges. Strong edges, or edges with a value greater than the predetermined threshold value, are always marked as edges. Weak edges are checked for connectivity with strong edges. Connected edges are added, and non-connected weak edges are rejected.

The MATLAB implementation of the Canny algorithm uses two thresholds to distinguish between the weak and strong edges. Starting with strong edges, the weak edge result is used to establish continuous edges that exist in an image [73]. This pairs well with schlieren imaging, as the sharp boundary between the discontinuous densities of two mixing gases is highlighted by the derivative, creating strong edges for detection. Znamenskaya and Doroshchenko applied machine learning and neural networks to develop edge detection techniques specifically for schlieren and shadowgraphy that rely heavily on the Canny edge detection algorithm [74]. Rigby et. al. used a combination of thresholding algorithms and Canny edge detection to identify and track the fireball from several PE-4 charges, and relied on the intense light emission of the explosive event to establish the boundaries of the fireball [75]. This combined approach is applicable for direct imaging of explosive tests.

Other methods exist for the extraction of gaseous boundaries from schlieren images. Lazzaro et. al. applied curvature filters as developed by Gong and Sbalzarini to schlieren images of diesel injection plumes to achieve effective segmentation of the images [76, 77]. Curvature filtering is a variational method that achieves a similar goal as edge detection by segmenting off regions of the images with differing properties.

1.5.2 Filtering and noise rejection

A significant portion of successful fireball segmentation and edge detection is the rejection of background noise. The techniques discussed above commonly detected edges not associated with the desired object or image segment. The Gaussian filtering used in Canny suppresses some imaging noise, but is not always sufficient. Background subtraction is commonly applied to remove or reduce background noise and highlight regions of significant change [63, 78]. A wide variety of background subtraction techniques exist for computer vision, but in the context of high speed imaging tare and sequential subtraction are commonly used [63, 79].

Morphological image processing manipulates binary images using binary filters to identify, isolate, and refine markers for object identification [80]. This is commonly applied as an image segmentation technique, and can be used to identify larger objects that may be broken up upon a more refined examination. Recent developments use morphological operations on thresholded fireball images ot produce a best estimate fireballs for events shrouded in particulate matter and reflections [81]. Morphological filters avoid the edge softening common in general spatial filtering, which is important for retaining maximum detail on the fireball contour.

1.5.3 Fireball identification

The explosive fireball is a complex rapidly evolving environment encapsulating the high temperature detonation products and their interaction and reaction with the ambient environment. The distinction between fireball and non-fireball in the detonation environment is not always consistent in literature [82–84].

Phenomenology of fireballs A consistent definition of the fireball is important to a meaningful diagnostic interpretation of fireball evolution. Some treatments have used the fireball as an abstract concept, and segmented the image based on other metrics, such as modeling results [34, 83], absorption or emission spectroscopy [84–86], or estimated temperature [82]. Much of the characterization of fireball phenomenology is focused on the remote sensing aspects of fireball detection [84, 86], or developed in the discussion of nuclear weapons research [83, 87]. The temperature approach taken by Brode in numerical models and Slaughter using image analysis has a strong basis in the physical event, but still decouples the fireball from the detonation product gases, a problem for implementation on conventional explosives where product gases are principal driving factor in expansion [22, 82, 83].

Works studying the surface mixing of high explosive fireballs have historically used either simulation results identifying product gas location [34, 88], or visual indicators of combustion or gas species variation [34, 37, 75]. Others have used particulate matter resultant from the detonation process in conjunction with particle image velocimetery to attempt a velocity based fireball segmentation[54] or to identify the product gas state by soot location estimation [89]. The lack of a consistent fireball definition is product of the difficulty in unifying the properties diagnostics can readily detect such as light intensity, emission or absorption wavelength is representative of the different goals of the explosive researchers.

Imaging detection of fireballs Imaging based methods identify a combination of the principal fireball components. The use of high intensity pixels to identify the boundary of the fireball is in line with best practice in the literature [75, 79]. The fireball is optically distinguished by the high and low intensity regions corresponding to luminescent and sooty areas respectively on the surface of the fireball. In early time evolution, the fireball has not cooled, and imaging is dominated by high brightness [79, 83]. It identifies the region of high temperature gas such that the optical depth of the fireball is great enough to present as an opaque surface to a camera [81]. Late time exact identification of the fireball is optically difficult due to the combination of high contrast areas of combustion with low contrast soot and particulate clouds [81].

1.6 Scaling

In the study of physical phenomena it is often advantageous to connect the behavior of small events to bigger ones, and vise versa. These connections are often achieved through the development of scaling laws, or non-dimensional relationships between critical characteristics of an event. Scaling criteria are used extensively in fluid dynamics, from aerodynamics to intense flood models [90]. The study of explosive effects has a long history of developing and applying scaling laws.

1.6.1 Dimensional analysis and nondimensionalization

Dimensional analysis is a frequent tool for the derivation of scaling laws. It is build upon the assertion that the behavior of the physical world should not depend upon arbitrary units, and therefore the functions that express that behavior should be functions of fundamental properties [91]. The methodology for building nondimensional terms is formalized in the Buckingham-Pi theorem [92], though the concept was not new, having previously been used in the identification of flow stability criteria by Lord Rayleigh [11]. The basic concept is to take a census of critical variables for the problem at hand, and to reduce those variables in to non-dimensional Π terms in such a way as to reduce the total number of controlling variables of a function.

1.6.2 Scaling of explosive behavior

It is important to understand the contextual background of scaling in energetics to justify the development of a scaling law for the gas cloud evolution. Historically, dimensional analysis and similarity solutions have been applied to develop models linking the evolution of Mach-radius curves, times of arrival, and delivered shock impulse. The most famous similarity solution is Taylor's solution for the blast wave from very large explosions [93].

For an explosive event, the relationship between atmospheric conditions, charge weight, and external geometry are significant factors for the evolution of explosive effects such as the shock wave. Normalizing the initial conditions of an explosion so that its effects can be predicted based on results from other explosive tests is central to explosive engineering doctrine. Early work includes the foundational Sachs scaling, which has three primary components, scaled distance, scaled time, and scaled impulse [94]. For explosions in free air, scaled distance can be recovered from the assumption that the intensity of a shock wave will be related to the cube root of the energy release scaled by the density of the

atmosphere at which the explosion takes place [95]. The concept that shock intensity is a functional form of the cube root of a relationship between energy release W and atmospheric density ρ give the most basic distance scaling,

$$Z = \frac{r\rho^{1/3}}{W^{1/3}}$$

where Z is the scaled distance equivalent to the actual distance r. Applications of this scaling frequently express atmospheric density and explosive energy release in terms of a ratio to a reference value, ρ_0 and W_0 respectively,

$$Z = \frac{(\rho/\rho_0)^{1/3} \cdot r}{(W/W_0)^{1/3}} \tag{1.38}$$

An important consideration for utilizing scaled distance is the impact of the ratio between the pre-detonation explosive radius and the shock wave radius. For nuclear explosions, the charge radius is effectively zero, whereas two different explosive compositions might have radically different densities and therefore charge radii. Equations similar to Equation 1.38 can be made for scaled time. Shock arrival time t_a can be computed as a function of Mach number M and local speed of sound C.

$$t_a = \frac{1}{C}\int_0^r \frac{dr}{M}$$

Mach number is a function of shock radius r. Substituting the scaled distance Z in for r time of arrival equation, and dividing both sides by a reference atmospheric speed of sound C_0,

$$\frac{t_a(\rho/\rho_0)^{1/3}(C/C_0)}{(W/W_0)^{1/3}} = \frac{1}{C_0}\int_0^Z \frac{dZ}{M}$$

It is clear that Equation 1.6.2 is of the same form as the time of arrival equation for any scaled radius Z, so scaled time may be writtten as,

$$\tau = t\frac{(\rho/\rho_0)^{1/3}(C/C_0)}{(W/W_0)^{1/3}} \tag{1.39}$$

The simplicity of this scaling has allowed it to stand the test of time with relatively minor adjustment. Wei and Hargather summarize the history, with the major adjustments begin in the choice of new repeating variable for the dimensional analysis argument. The Wei-Hargather new scaling uses control parameters of explosive energy E_{HE}, fluid density ρ_0, speed of sound C_0, radius R, and t [96]. With repeating variables E_{HE}, ρ_0, C_0, they arrive at Equation 1.40 for scaled distance:

$$R^* = \frac{RP_0^{1/3}}{m_{HE}^{1/3}}\frac{\gamma^{1/3}}{e_{HE}^{1/3}} \tag{1.40}$$

The time variable also scales with explosive energy:

$$t^* = \frac{tC_0}{(E_{HE}/(\rho_0 C_0^2))^{1/3}} \tag{1.41}$$

At early times, the shock wave remains attached to the gas cloud, but as the energy driving the rapid gas expansion is expended, the gas cloud separates from the shock wave. The air which the gas cloud expands into has been first processed by the shock so the ambient conditions governing its evolution are not the same conditions as the shock wave is traveling through. There is currently a gap in the understand of the explosive event when it comes to the scaling of the fireball after the separation from the shock wave.

Historically, the evaluation of fireball size was largely empirical, with approximate equations given by Glasstone for the radius of a nuclear fireball in free air,

$$R_{fireball} = 90W^{0.4}$$

where radius R is in feet and weapon yield W is in Kilotons TNT equivalent [97]. Glasstone also references an approximate radius for shock detachment from the fireball,

$$R_{breakaway} = 110W^{0.4}$$

again using feet and Kilotons TNT [97]. Of note for these equations is the lack of time dependence, as the expectation was these equations would be applied to the late time fireball, after the majority of its expansion. Recent work has built on the early work of Sedov to establish a direct scaling of the turbulent combustion fields, with validation against simulation [34]. It found that all aspects of the fireball scale with a cube root scaling law. Important for the present work is the functional scaling of the fireball radius as a function of the scaled time and characteristic length scale R_0. The turbulent combustion of the fireball, as identified by RMS velocity fluctuations, also scaled with respect to R_0. However, it is directly noted that certain aspects of real fireballs, such as mists and particles, deviate from the scaling found through simulation.

1.6.3 Scaling of surface instabilities and mixing

In research on mixing, characteristic time scales have been proposed for different growth regimes. Scaling attempts for this region have tended to build the scaling variables around the wave number and amplitude of the initial perturbation in conjunction with a characteristic velocity to arrive at a scaled time. By basing a scaling in the Richtmyer implusive model as seen in Equation 1.34, McFarland arrived at a scaled time of,

$$\tau = k\dot{h}_0(t - t^*) \tag{1.42}$$

where

$$\dot{h}_0 = kh_0' A' \Delta u \tag{1.43}$$

and t^* is an offset time defined by the amount of time taken for a shock of velocity U to cross the interface at an angle θ[98]:

$$t^* = \frac{\lambda}{2U \tan\theta} \tag{1.44}$$

The reported effectiveness of this scaling is marginal beyond low values for τ, highlighting multi-timescale interactions of even relatively simple shock driven mixing. A characteristic timescale has been proposed for the early development of RMI,

$$\tau = \frac{1}{2k}\left(\frac{1-A^*}{U_{S_2}} + \frac{1+A^+}{(-U_{S_1})}\right) \tag{1.45}$$

where A^+ and A^- are the pre and post shock Atwood numbers, U_{s_1} and U_{s_2} are shock velocities from the transmitted and reflected shock respectively, and k is the perturbation wave number[99]. Scalings for instability growth are predominately developed in the context of a shock tube experiments, and have limited validation against perturbation growth in spherical geometries. Additionally, much of the experimental validation of these models occurs at relatively low mach numbers, not the relatively high Mach number environment encountered in a detonation environment [98, 100].

1.7 Research objectives

Mixing on the surface of an explosively driven fireball is important for post detonation fluid-dynamic models and understanding the expansion of product gases. The mixing width of an evolving contact surface is representative of the evolution of the driving instabilities. The evolution of the mixing width has been analytically characterized, and can be measured optically. The fractal dimension has been applied to the study of high speed turbulent mixing in shock tubes and at a small scale for explosive characterization. The fractal dimension represents the development of multiple length scales that are characteristic to the evolution of fully developed turbulence. The nexus of these is the foundation for the present research.

The purpose of this research is to characterize the relationship between turbulent mixing width and fractal dimension in the immediate post detonation environment. Analytical models and experimental studies are utilized to analyze the growth of mixing on the surface of early time fireballs from varied high explosive charges. The characterization of this relationship is intended to provide insight into the formation of surface instabilities on the fireball, and their growth towards turbulence. This research will connect the change in fractal dimension to the existing explosive scaling laws to give better understanding of what flow regimes can be fractally characterized. The answers to three questions form the core of this effort:

- How well do existing analytical models for the growth of the mixing width in high explosives represent the detonation product gas expansion for real explosives?
- What is the utility of shock focused non-dimensionalizations and scaling criteria when applied to non-shock aspects of the fireball process?
- Does the fractal dimension of a fireball contour connect to the evolution of surface mixing?

The hypothesis here is that the evolution of mixing on the surface of an explosively driven fireball is related to the variation in the fractal dimension of that surface, as imaged by the projected contour of that fireball.

CHAPTER 2

EXPERIMENTAL CONFIGURATIONS

Four test series were used in this research. The study of variably confined explosive product gases utilized shotgun primers to develop methodologies for the identification of the mixing region width. A test series previously conducted at Eglin Air Force Base (AFB) was used to determine the consistency of the fractal measurement with multiple camera views on a single explosive event. Small scale tests were conducted using single grams of explosive material in a collimated imaging system to study fireball segmentation through the refractive differences between explosive products and air. A final test series was conducted using two masses of charges with dominant surface perturbations.

Each series is broken down into four sections. First, the characteristics of the explosive charges used are described, such as material and explosive energy. Second, the testing apparatus is described, including physical layout of explosive charges, support structures, and any confining geometry. This section also includes discussion of number of repetitions. Third, the imaging diagnostics are described, including any camera settings, external illumination, or supporting optics. Finally, the image processing used to extract the fireball profile is detailed.

2.1 Variable confinement of explosive gases

Shotgun primers were used to produce a repeatable point source explosively driven gas cloud [101]. The primers were fired into a semi-confined region enclosed on two sides with acrylic panels. Schlieren imaging was used to capture the expansion of the gas cloud. An automated image processing method, validated against manual tracking, extracted the mixing region width as a function of time in addition to time resolved gas cloud radius data.

2.1.1 Explosives used

Winchester 209 shotgun primers were initiated using a pneumatic cylinder and vented into a confined gap between two parallel acrylic plates. The shotgun

primer contained approximately 50 mg of explosive material consisting of 45% lead styphnate, 37% barium nitrate, and 18% antimony sulfide by weight. The primers are approximately cylindrical, with a diameter of 6.4mm and a height of 7.8mm. Upon initiation the primers vent the produced gases along the axis of the primer through a hole with a diameter of 2.4mm. The exit diameter is used throughout the primer analysis as the effective charge diameter (CD) for scaling.

2.1.2 Experimental Apparatus

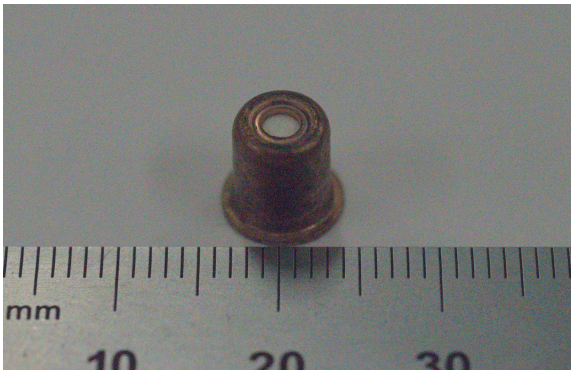

Figure 2.1: A Winchester 209 shotgun primer. The vent hole is the the white circular region on top of the primer.

The shotgun primers vented explosive product gases through a 2.4 mm-diameter hole on the end of the cylinder. An example shotgun primer is shown in Figure 2.1. The primer was retained in a test fixture that directed the venting gases into a confined volume between two acrylic plates, as shown in Figure 2.2. The test fixture directed the axis of the explosion into the acrylic plates, forming a uniform expansion radially away from the primer axis. The separation of the plates was varied to control the degree of three-dimensionality of the expanding gas front. The spacing between the acrylic plates was set by 3D-printed spacers at increments of 1, 2, 5, 10, and 15 charge diameters, 2.4 mm, 4.8 mm, 11.9 mm, 23.8 mm, and 35.7 mm, respectively. An unconfined configuration removed the lower acrylic plate, allowing free expansion of the gases along the axis of the primer. The high confinement cases are representative of the cylindrical case. As confinement is reduced, the flow becomes more three-dimensional and ultimately approximates a spherical expansion, as shown schematically in Figure 2.3.

The primers were initiated by a pneumatically driven firing pin actuated by a solenoid valve connected to the camera trigger circuit. The pneumatic cylinder was supplied by a cylinder of dry air regulated to 1034 kPa. The delay time from triggering to first visible gas in the test section was between 10 ms and 20 ms. The firing circuit is shown in Figure 2.4.

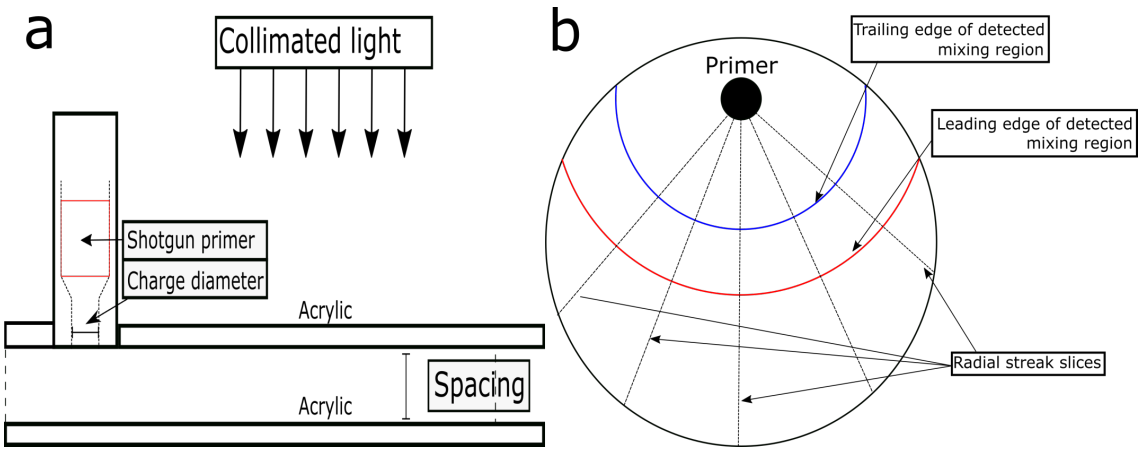

Figure 2.2: (a) Cross sectional diagram of the shotgun primer test section. The shotgun primer drives gas into the expansion volume between the two acrylic plates. (b) The imaging field of view through the top of the acrylic. The radial streaks used for locating the leading and trailing shocks are shown schematically.

2.1.3 Imaging

A lens type, parallel light schlieren system was used to image the explosive events. To allow the test section to be oriented horizontally, the collimated light was passed through two turning mirrors in a periscope configuration, as shown in Figure 2.4. Images were captured on a Photron SA-X2 high speed camera at 200,000 frames per second (fps) with a resolution of 256x152 pixels. The camera settings were chosen to maximize frame rate while retaining an effective spatial resolution of less than 1 mm/px on the radius of the gas cloud. The minimum time between the gas cloud exiting the primer gun and exiting the field of view was approximately 150 μs. At 200 kfps, there were 30 event frames for the fastest event, which was considered satisfactory for the determination of an acceleration profile. The camera was exposed using a 10 ns pulsed SI-LUX spoiled coherence laser illumination at 640 nm wavelength. The schlieren imaging light was passed through a 640 nm band-pass filter before passing the knife edge cut-off. Refractive imaging was used to identify the interface between the explosive products and ambient air by the strong density gradient between the two species. Figure 2.5 shows a representative time series of images from the shotgun primer expansion. The gray semi-circle at the point of origin is the imaging axis being occluded by the shadow of the primer gun, which is 28.8 mm in diameter.

2.1.4 Image Processing

Two imaging processing techniques were used for this work: an automated technique based on edge detection and morphological processing and a manual

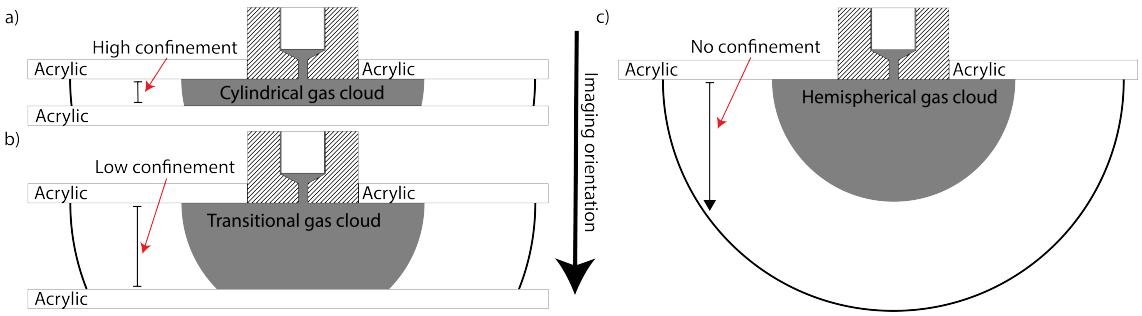

Figure 2.3: The shotgun primer explosive products were driven into the expansion volume between two acrylic plates. In (a) the high confinement configuration, the expanding products have an approximately cylindrical expansion. As the plates were separated, (b) the shape of the explosive product gas interface began to transition from a cylinder to a (c) hemispherical cloud once the opposing plate was fully removed.

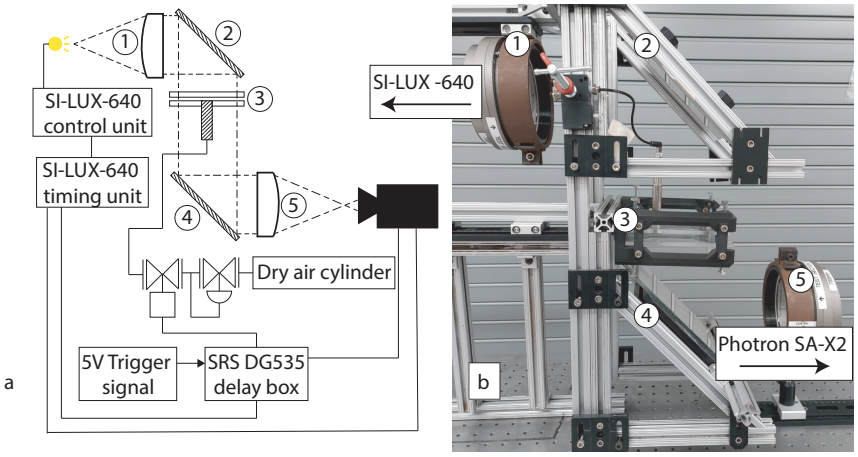

Figure 2.4: (a) Schematic diagram and (b) labeled image of the testing setup. Light passing through the collimating lens (1), was turned 90 degrees by a first surface turning mirror (2), and passed through the acrylic test section(3). It was then turned 90 degree by a second turning mirror (5), and focused onto a knife edge by another collimating lens (5).

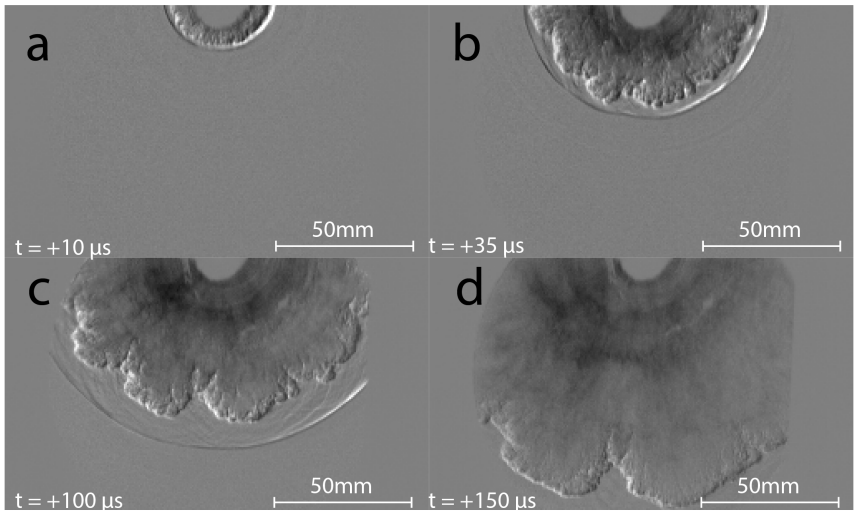

Figure 2.5: Schlieren image sequence of the product gas cloud in the two charge diameter case evolving from (a) the initial stages, where the shock and product gas clouds are visually indistinct and partially occluded by the primer gun to (b) a developing boundary with discernible peaks and valleys. The close proximity of the shock during this time differentiates it from the (c) mid-time, where the shock has fully separated from the gas cloud, and significant gas front evolution has occurred. (d) The gas cloud continues to expand and eventually passes out of frame.

peak and valley tracking process. The manual tracking was used as a baseline measurement for the automated technique.

Manual tracking of the shotgun primer mixing region width was performed by two individuals to compare to the automated extraction. The individuals were trained in the definition and appearance of "peaks" and "valleys" in turbulent mixing, then instructed to locate the "peaks" and "valleys" of the expanding product gas cloud in each image. No fixed number of points was prescribed for each image, and individual discretion was applied to determine the extent of the gas clouds. The product gas cloud was tracked from the first frame it became distinct from the shock wave until either reshock off the testing apparatus or exit of the product gas cloud from the frame. The manual tracking data was found to be consistent with the automated techniques for tracking.

An automated method of thresholding and edge detection was applied to the primer product gas cloud images to identify the boundaries of the mixing region in the flow. The original images I_{base} are processed in MATLAB. First, a reference image I_{ref} is subtracted from each image in the set to regularize the background and create the set of images I_{sub}. For each time step, the previous image in I_{sub} is subtracted from the current image, creating the difference image I_{dif}. The image I_{dif} is added to I_{sub} to form I_{HL}, highlighting areas of change between the images, such as the mixing region. A Canny edge detection is then applied and a morphological close operation is performed to connect nearest neighbor pixels in the mixing region. The closed image I_{closed} is then eroded by a larger disk structural element to remove noise and weak waves behind the shock front, producing I_{erode}. A morphological reconstruction I_{recon} is created, using I_{erode} as the marker and I_{closed} as the mask image. The edge binary image I_{recon} is taken to represent the boundary of the mixing region.

$$I_{sub} = I_{base} - I_{ref} \tag{2.1}$$

$$I_{dif} = I_{sub,n} - I_{sub,n-1} \tag{2.2}$$

$$I_{HL} = I_{sub} + I_{dif} \tag{2.3}$$

To differentiate the front of the mixing region from the back, rays are traced out from the explosion center, and the first intersection with the gas cloud edge is marked as the "valley", or back of the mixing region. The intersection furthest from the center is taken as the "peak" or front of the mixing interface. Figure 2.6 shows the process, along with the end result. All distances are measured as a radius from the center axis of the shotgun primer. The bulk radius for the expanding gas cloud is taken as the average radius across the region of interest. The region of interest is the 90° arc centered at the primer and swept from -45° off vertical to 45° off vertical, measured clockwise.

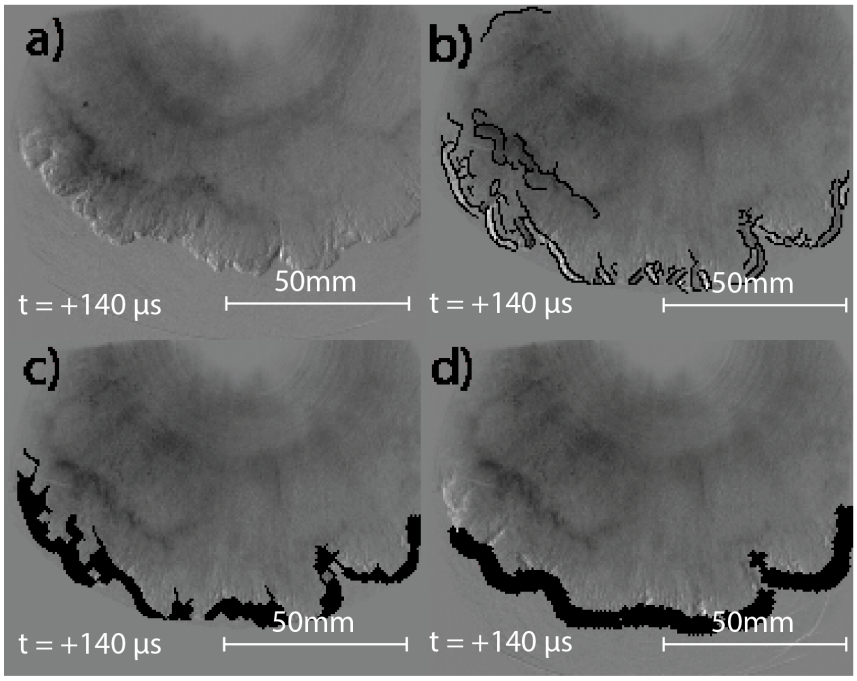

Figure 2.6: Processing flow for morphological thresholding method, exemplified on the 1 CD case. The (a) original highlighted image I_{HL} was first processed with (b) a Canny edge detection algorithm. (c) The detected edges were morphologically opened and closed to merge 8-neighborhood adjacent boundary pixels, making I_{recon}. (d) The furthest extent radially from the center of the explosion was extracted, and treated as the beginning of the mixing interface.

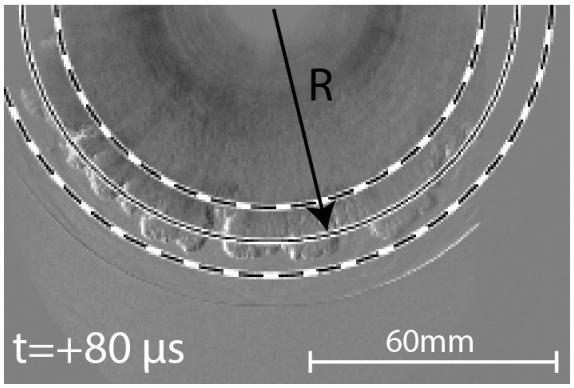

Figure 2.7: The mixing region width is typically measured from a center line of the interface, with peak and valley distances measured from that radius. This image is from the two charge diameter separation case and highlights the average location (black line), the bottom of the valleys (innermost dashed line) and top of the peaks (outermost dashed line).

Table 2.1: Camera settings for the 1.32 kg PBXN-113 tests. Angle is clockwise relative to the 0° camera.

Camera	Frame Rate (fps)	Resolution (pixels)	Angle (degrees)
Phantom v1212	50000	512x320	0
Phantom v1212	50000	512x368	45
Phantom v611	50000	304x216	60
Phantom v711	50000	400x216	299
Phantom v711	50000	384x304	315

2.2 Multi-camera imaging of an explosive event

To assess the validity of the symmetry assumptions for fractal dimension analysis, a test series with multiple camera views was required. A test series conducted at the Eglin Air Force Base Advanced Warhead Experimentation Facility (AWEF) satisfied this requirement. This test series was from a study of shock interactions, and reshock of the gas cloud was unavoidable [102]. The primary use of the Eglin data was analytical method development and initial fractal dimension extraction considerations.

2.2.1 Explosives used

The tests conducted at Eglin Air Force Base used PBXN-113, a plastic bonded explosive with an energetic makeup of 45% 1,3,4,5-Tetranitro-1,3,5,7-tetrazocane (HMX), 20% hydroxy-terminated polybutadiene (HTPB) binder and 35% Aluminum by weight [103]. For scaling purposes, PBXN-113 is estimated to have a heat of detonation of 2.76 MJ/kg. The charges has a diameter of 58.3 mm. Each charge was initiated with a RP-1 detonator and small PBXN-5 booster [102]. Testing at Eglin AFB consisted of 1.32 kg spherical charges suspended above a reflection platform.

2.2.2 Experimental Apparatus

The PBXN-113 tests were conducted with multiple cameras arrayed in an arc around the explosive event to capture as much three dimensional information as possible. Analysis of the multiple camera views was used to justify the symmetry arguments for the three-dimensional extrapolation of fractal dimension. Table 2.1 lists the camera setups for each testing series. Charges were suspended 1160 mm above the reflecting plate.

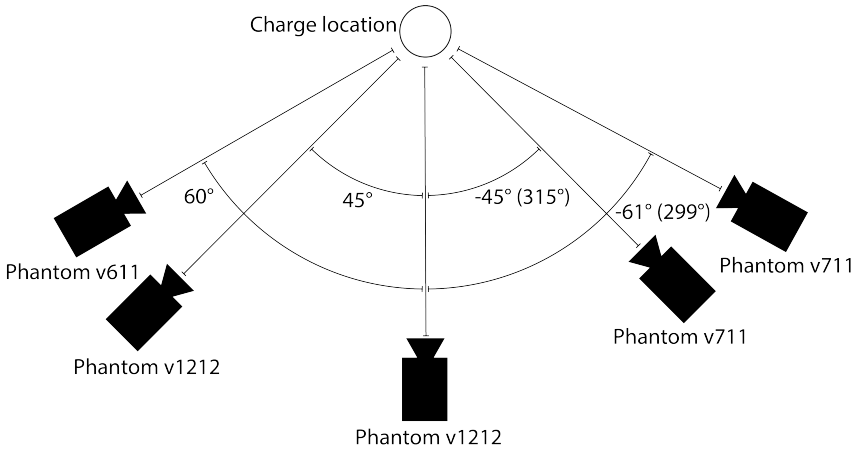

Figure 2.8: Layout of cameras for the PBXN-113 test series. Camera angles are referenced from the center camera clockwise.

2.2.3 Imaging

During testing, five high speed cameras were arrayed in an arc around the event. These tests captured early time gas cloud development, including significant impact from reflected ground shock with the fireball. The center camera used retroreflective shadowgraphy, the other cameras were set up for direct imaging of the explosion. Figure 2.8 shows the layout of the cameras, and Figure 2.9 shows representative images from each camera.

2.2.4 Image processing

For the kilogram scale tests using PBXN-113, image processing was simplified by the high contrast between the light production of the high temperature fireball and the dark background. The base image I was binarized directly using Otsu's method to get I_{binary}. To account for dark spots on the fireball surface, a morphological fill operation was used to get I_{filled}. To reduce noise, the binarized fireball was morphologically reconstructed using the charge center as the marker for reconstruction, producing I_{recon}. The reconstruction step was limited to 4-connectivity to limit the detection of bright surface reflections immediately adjacent to, but not part of, the fireball. The MATLAB *edge* function extracts the boundary of the binarized fireball, getting I_{out}.

2.3 Large scale schlieren imaging of small charges

Tests were conducted to evaluate the identification of detonation products, here representative of the explosive fireball, by using schlieren imaging to iden-

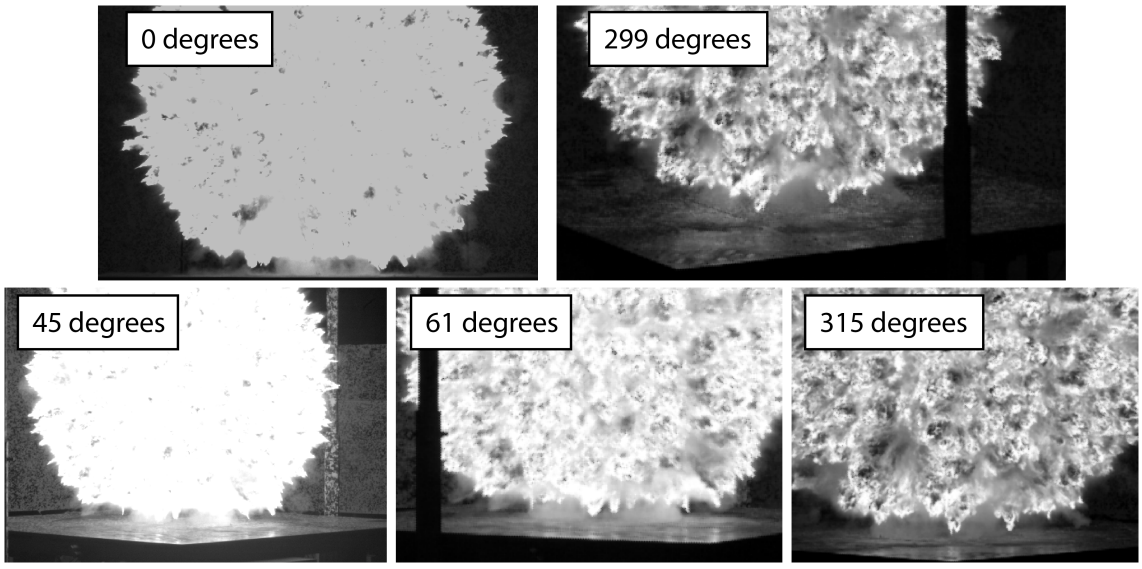

Figure 2.9: A representative image set from the PBXN-113 tests demonstrating the high contrast fireball images. The five available camera views cover a total angle of 122 degrees. These images are at t=1.42 ms from initiation.

tify regions of significant change in refractive index. Full field imaging of the explosive event was achieved using 1 m diameter mirrors in a modified z-type setup. A variety of explosive materials were tested, with Primasheet providing the clearest fireball. The fireball contour was extracted from images and used to calculate fractal evolution.

2.3.1 Explosives used

Gram scale charges were made of a variety of explosives, including pentaerythritol tetranitrate (PETN), 1,3,5-trinitroperhydro-1,3,5-triazine (RDX), and Ensign-Bickford Primasheet 2000 (88.2% RDX by weight) , also known as detasheet, to explore the impact different explosive formulations have on ease of image processing. PETN has a heat of detonation of 6.32 MJ/kg, RDX has a heat of detonation of 6.19 MJ/kg, and Primasheet 2000 has an estimated heat of detonation of 5.45 MJ/kg[104]. Charges were constructed by pressing the explosives into an approximately spherical pellet and inserting either a Teledyne RISI RP-2 exploding bridgewire (EBW) detonator containing 32 mg of PETN and 18 mg of RDX and binder or a Teledyne RISI RP-3 EBW detonator containing 27 mg PETN [105]. Schematic drawings of the pellet can be found in Appendix A. PETN and RDX experienced issues with pressing consistency and mechanically failing pellets. The surface of the Detasheet charges had more visible imperfections and surface artifacts, but the produced gas clouds do not seem to be adversely impacted by the initial surface geometry. Pellets of all four materials can be seen in

Figure 2.10. The RDX and PETN pellets were a pressed powder with no binding agent, while the Primasheet charges were formed with hand pressure in the same dies. The RDX and PETN pellets were mechanically fragile, and charge assembly was difficult without damaging or destroying the pellets.

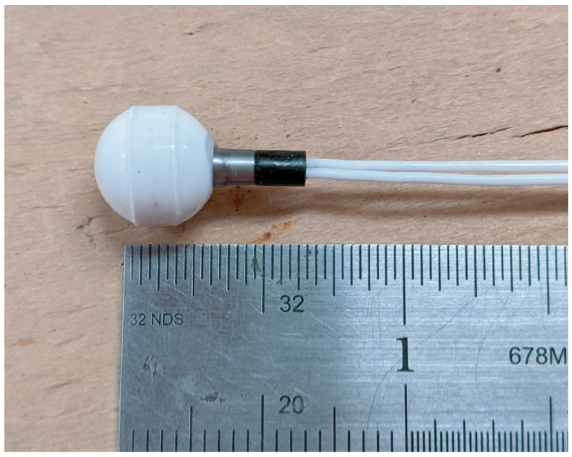

Pressed PETN

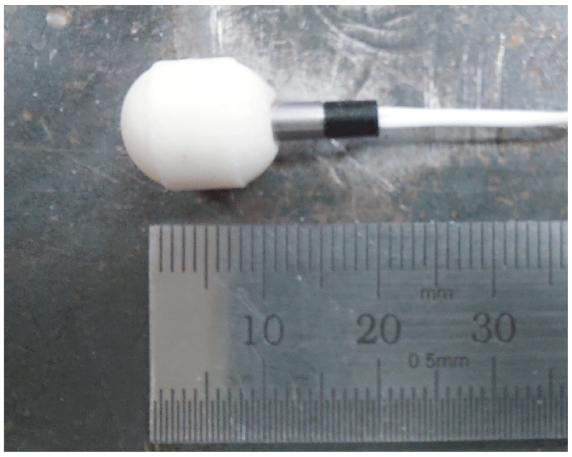

Pressed RDX

Formed Detasheet C1

Figure 2.10: The three different explosives used for 1 g charges. The pressed powder charges had good surface finish, but suffered mechanical failure more frequently compared to the charges formed from plasticized explosives. The scale for the PETN charge is in inches, the scale for the RDX and Primasheet charges is in mm.

2.3.2 Experimental apparatus

Gram scale experiments were performed at New Mexico Tech in the Ballistic Sciences Laboratory (BSL) located in the Energetic Materials Research and Testing Center (EMRTC) field lab. The experiments used a gantry system to suspend the charges to ensure the gas cloud would not experience reshock from a ground reflection until the experiment had ended. The pellet geometry is approximately spherical, but has a flat walled shoulder for ease of pressing and to mitigate the risk of explosive pellets becoming stuck in pressing dies. Detonators were used to initiate the explosive from approximately the center of the spherical shape. Charges were oriented so that the bottom of the detonator was facing perpendicular to the optical axis. This limited asymmetry effects due to both the bottom of the detonator and the shoulder of the pressed pellet. Figure 2.11 shows a one-gram charge hanging from the gantry in position to be fired. The long axis of symmetry for the detonator was aligned with the optical axis of the 1 m schlieren system in order to present the most symmetrical fireball to the camera.

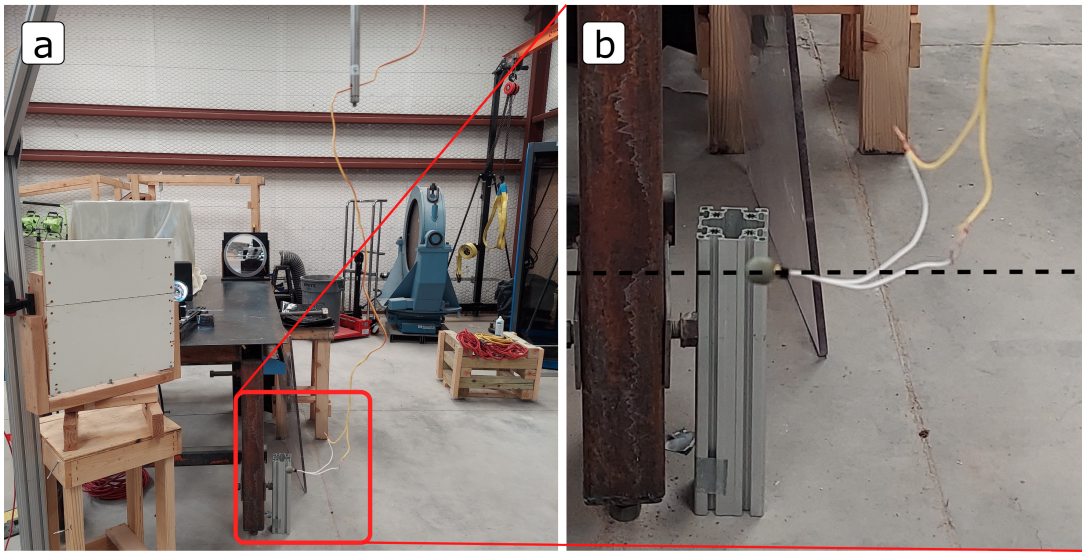

Figure 2.11: (a) A 1 gram charge of Primasheet 2000 hanging from the explosive gantry. The charge (b) was oriented to align the axis of symmetry of the detonator, shown here as a dashed black line, with the optical axis of the 1 m schlieren system.

2.3.3 Imaging

The gram scale tests used two schlieren imaging systems as shown in Figure 2.12; a standard z-type with 300 mm field of view and a modified double-pass

folded z-type with 1 m mirrors. The modified z-type system is necessary due to availability of 1 m optics, limiting the setup to a single flat mirror and a single parabolic mirror at that size. The system is designed using WinLens to limit the coma and aspheric distortion in the image by turning the image using flat mirrors [106]. The imaging systems both used Shimadzu HPV-X2 ultra high speed cameras, operating at 100 kfps and 500 kfps, respectively. The HPV-X2 has an imaging resolution of 400 x 250 pixels, and captures 128 images per test. The 1 m system was illuminated using a SI-LUX640 spoiled coherence pulsed imaging laser with 10 ns pulse width. The optical train for the laser system included a 640 nm bandpass filter and neutral density filter to reduce the effects of direct illumination. The 300 mm system was illuminated using a SugarCUBE Ultra white light illumination system, and relied on the 200 ns shutter speed of the camera for exposure control. No neutral density filters were used with the SugarCUBE. The 300 mm system used a -1 m focal length meniscus lens to bring the center of the test section into sharp focus as described by Torres et. al. [107].

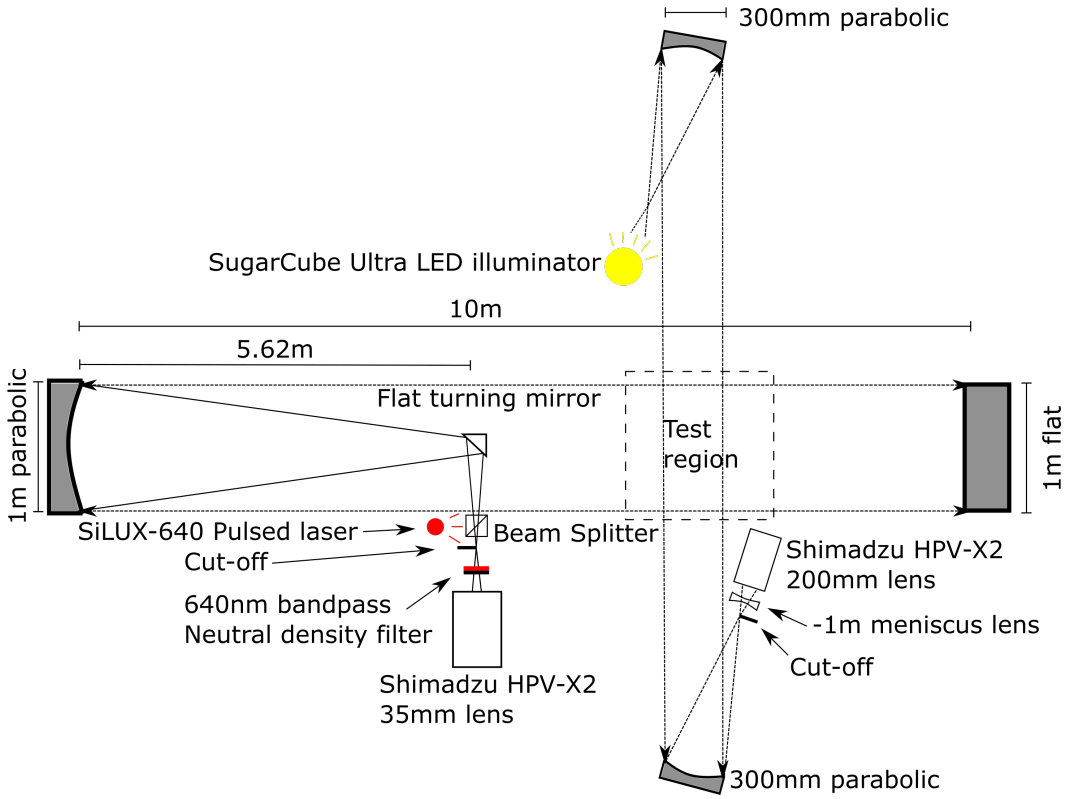

Figure 2.12: A schematic of the double-pass schlieren system used to image the gram scale explosive charges. The primary system using the 1 m mirrors has a 75 mm hole in the primary optics. An effort was made to align the flat turning mirror with the optics center hole to minimize the impact on the overall image.

2.3.4 Image processing

The image processing flow for the gram scale charge data is similar to the process developed for the primer analysis. A graphical outline of the processing is shown in Figure 2.13. A baseline cold image I_{cold} is created from the first image in the data set. Two masks are created: a mask identifying the center of the explosion I_{center}, and a circular mask identifying the boundary of the mirrors in the image I_{mirror}. First, the target image I_{hot} is filtered with a Gaussian filter to make I_{gauss}. I_{gauss} is then binarized and cropped using I_{mirror}. Final noise is rejected by morphologically reconstructing only the gas cloud using I_{center} as the marker, forming I_{cloud}. Using I_{cloud} as a masked, an edge detection is performed on the gas cloud, making $I_{cloudEdge}$. For all images beyond I_{cold}, $I_{cold,cloudEdge}$ is subtracted from $I_{cloudEdge}$ to remove static elements of the image such as the turning mirror stand. The output image I_{out} is processed to determine the fractal dimension.

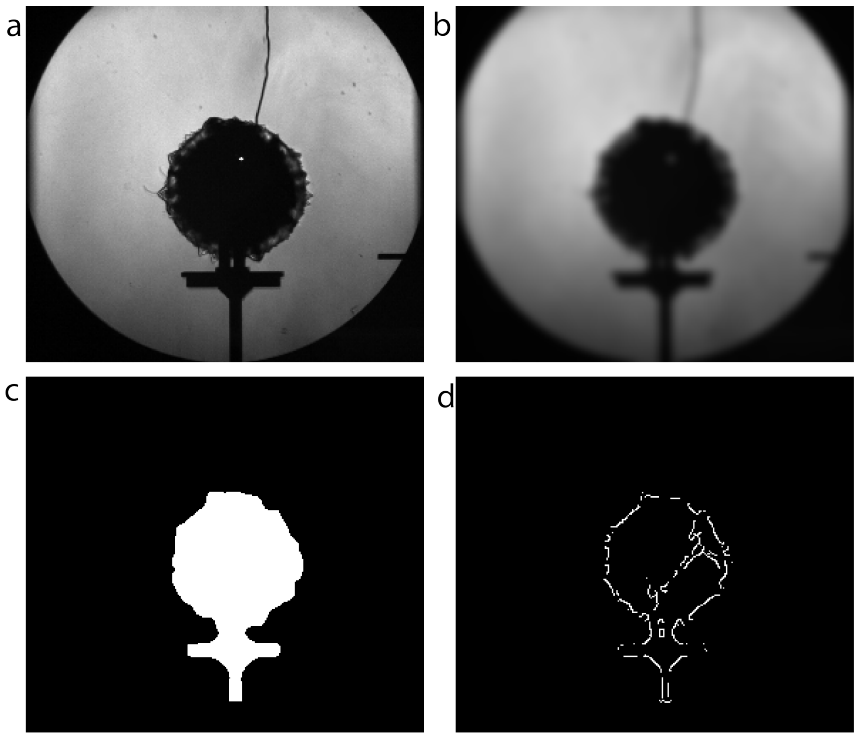

Figure 2.13: The image processing for edge extraction begins with (a) I_{hot} which was is processed with a Gaussian filter to make (b) I_{gauss}. Morphological operations are conducted to identify the (c) gas cloud I_{cloud}. A final edge detection finds the (d) gas cloud interface $I_{cloudEdge}$.

2.4 Field scale perturbed sphere test cases

Explosive tests were conducted using C4 spheres with known surface perturbations to identify changes in early time mixing evolution. Events were captured by three cameras recorded at different frame rates from the same position relative to the detonation. The fireball contour was extracted and the mixing region calculated for all cameras.

2.4.1 Explosives used

Tests conducted at EMRTC used composition C-4 (C4) hand tamped to a density of 1.5 g/cc into 3D printed spherical molds. The density of 1.5 g/cc is considered normal for hand packed C4 charges [108]. C4 is 91% RDX, 2.1% Polyisobutylene, 1.6% Motor Oil, and 3.5% di(2 ethlhexyl) sebacate by weight [104]. C4 has a heat of detonation of 5.86 MJ/kg [104].

2.4.2 Experimental apparatus

Twenty two C-4 charges were detonated in free air at the New Mexico Tech (NMT) Energetic Materials Research and Testing Center (EMRTC). Charges were suspended 2.5 m off the ground to delay the arrival of the reflected shock wave from the ground. Three high speed cameras imaged the detonation and subsequent fireball expansion. Spherical explosive charges were molded out of C4 with

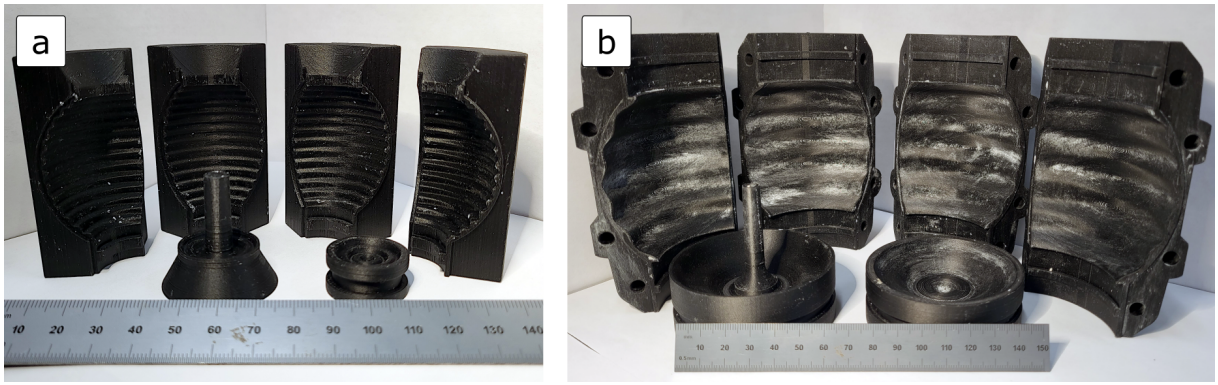

Figure 2.14: The 3D printed molds for (a) the 105 g, $f = 20$ charge and the (b) 880 g, $f = 10$ charge. The white substance on the molds is residual mold release.

smooth and sinusoidally perturbed surfaces using 3D printed negative molds with the desired perturbations. As shown in Figure 2.14, the molds consisted of 6 interlocking pieces externally clamped around the charge. The radius of the non-smooth charges was perturbed in the azimuthal direction to generate a known

Table 2.2: Six different configurations of perturbed spheres were tested. The $f = 0$ case is a baseline smooth sphere with no artificially dominant surface perturbations.

Charge mass	f	k	Repetitions
105 g	0	N/A	4
105 g	10	785.4 rad/m	4
105 g	20	1574 rad/m	4
880 g	0	N/A	4
880 g	10	384.6 rad/m	3
880 g	20	769.2 rad/m	3

initial gas cloud interface variation. The profile of the perturbed spheres was defined by

$$r(\phi) = R + \sin(f \cdot \phi) \tag{2.4}$$

where r is the charge radius at a given azimuthal angle ϕ. R is the radius of the unperturbed sphere, and f is the number of complete cycles per hemisphere. The radial wavenumber k of the charges is defined as:

$$k = \frac{2\pi}{f/(\pi R)} \tag{2.5}$$

For physical scaling purposes, f was kept at 10 and 20 for both the small and large charges. Table 2.2 summarizes the tested configurations in terms of wavenumber. Two masses were tested, 105 g charges with a base radius $R = 25.4$ mm, and 880 g charges with base radius $R = 50.4$ mm. Figure 2.16 shows the 6 charge configurations. Charge mass of the perturbed spheres compared to the smooth ones varied less than 1.8% of the total mass. The greatest variation was with the nominal 105 g, $f = 10$ charge, which had a mass of 106.9 g. The number of waves per revolution was kept constant, as well as initial perturbation amplitude. Amplitudes and frequencies were chosen to maintain an order of magnitude difference between the spatial resolution of the printed molds (0.1mm) and the spatial characteristics of the perturbations.

To suspend the 880 g charges without external support, a thin 0.8 mm acrylic plate of diameter 25 mm was embedded approximately 10 mm below the detonator well to attach the suspending cord. Charges were initiated using RP-83 detonators which were inserted from the top and embedded up to the center plane of the spheres, or a depth of 25.4 mm for the 105 g charges and 50.4 mm for 880 g charges.

Charges were suspended 2.5 m above the ground using 22.7-kg-test fishing line and a gantry as shown in Figure 2.16. This was done to delay the influence of any ground reflections until after the data collection period had elapsed. Charges were oriented as best as possible to align the axis of symmetry of the charge with the imaging plane of the cameras, or normal to the ground plane.

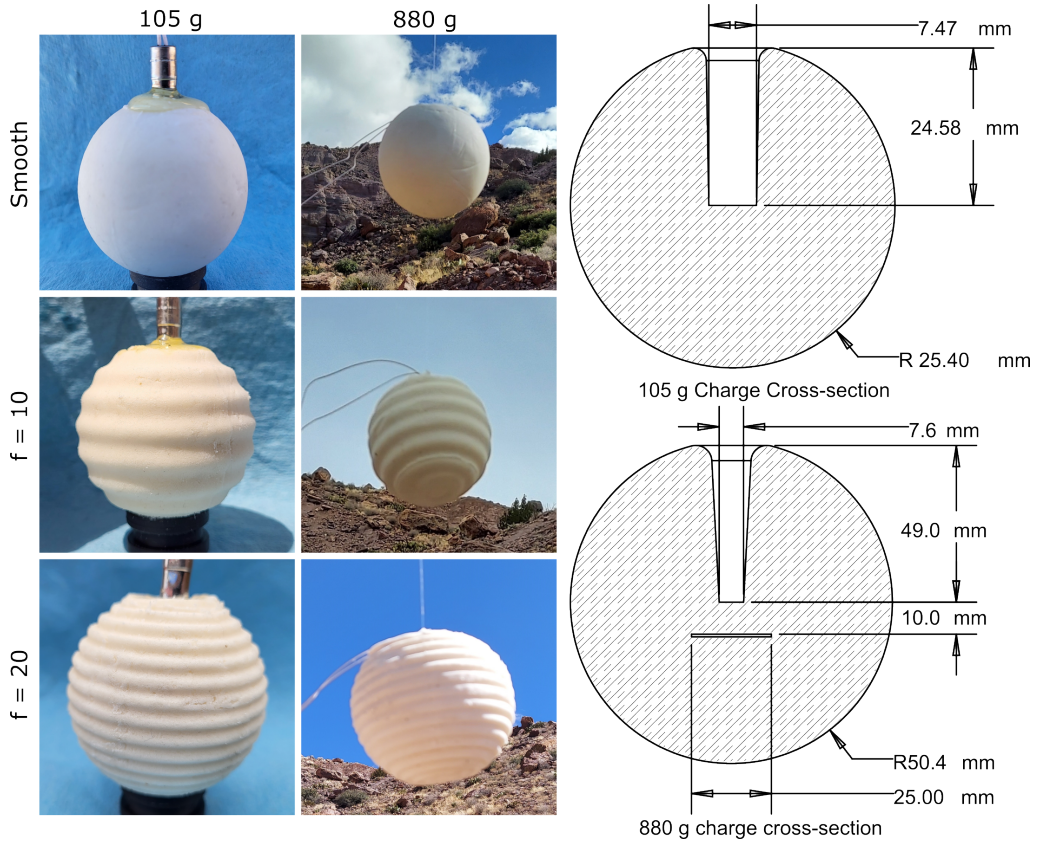

Figure 2.15: Six variations of charges were constructed across 2 masses and 3 perturbations. The nominal radius for the perturbed and non-perturbed charges remained the same. All charges were center detonated with the detonator entering through the top of the charge. The 880 g charges use a plastic support, 10 mm below the end of the detonator well, embedded in the explosive during molding to take the weight of hanging the charge off the detonator cables.

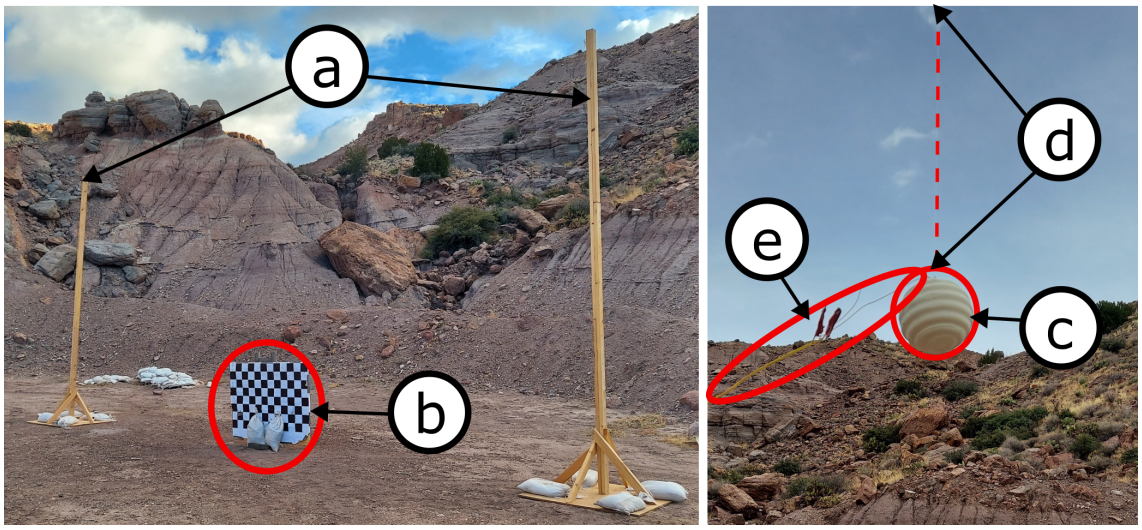

Figure 2.16: The gantry used to suspend the charges consisted of (a) 2 vertical posts 5 m in height separated by 10 m. (b) A stadia board was used to calibrate all cameras for each test. The (c) explosive charges were suspended at a height of 2.5 m from the ground by (d) line strung between the two uprights, while (e) the cabling for the RP-83 EBW detonator was strung off to the side to avoid interference with the perturbed surface.

2.4.3 Imaging

Three cameras were used to capture the event. Two Shimadzu HPV-X2 cameras, camera 1 and camera 2, were used for primary data collection. One Photron Nova S-16, camera 3, was used to maintain a long temporal record of the event. The two primary diagnostic cameras had resolutions of 400 pixels x 250 pixels and were run at 1,000,000 fps and 400,000 fps for the 105 g cases, and 800,000 fps and 200,000 fps for the 880 g cases, respectively. Both camera 1 and camera 2 are limited to 128 frames, resulting in a record time of 128 μs/320 μs for the 105 g charges and 160 μs/640 μs for the 880 g charges. Camera 3 recorded at 50,000 fps with a resolution of 512 pixels x 512 pixels, and collected data for 10 ms. The primary shock reflects off the ground at 4 ms, well after cameras 1 and 2 were done recording. The cameras were co-located 35 m from the charge. All cameras were calibrated using a stadia board at the imaging plane. The stadia board was a 1524 mm x 1219.2 mm checkerboard with alternating black and white 127-mm-wide squares, and can be seen in Figure 2.16.

2.4.4 Image processing

Images were processed to extract the most accurate representation of the gas cloud interface. Images from camera 1 and camera 2 were binarized to isolate the

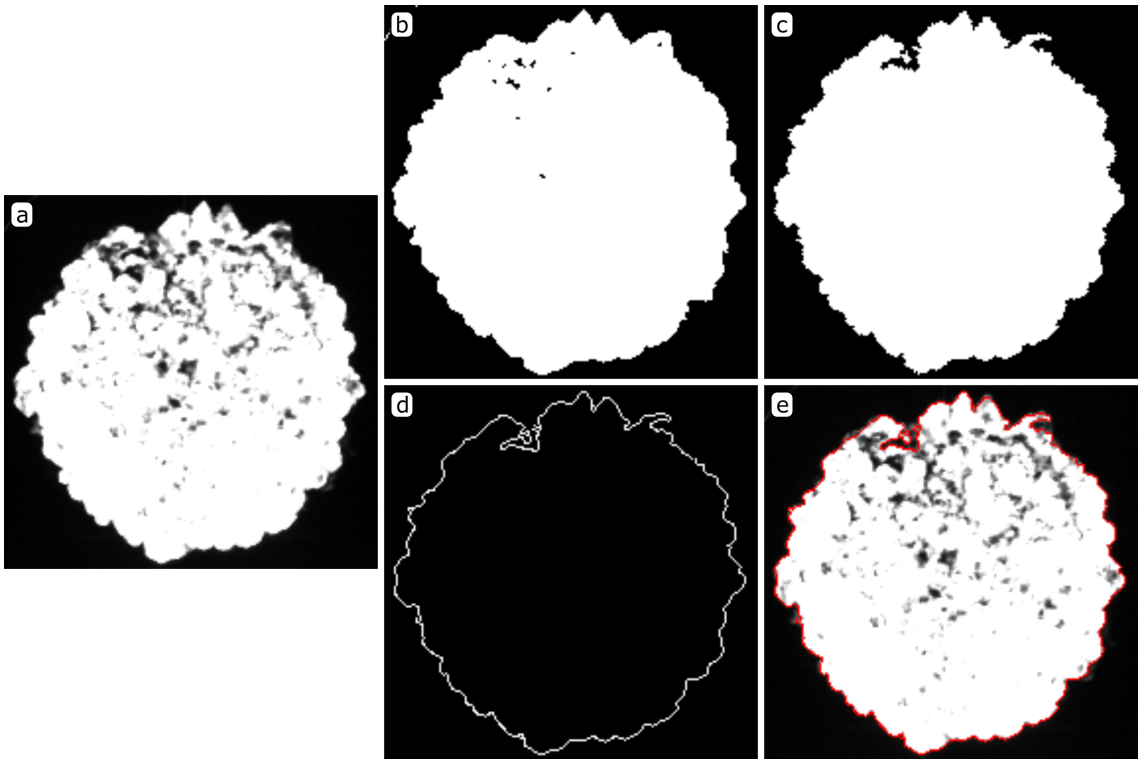

Figure 2.17: (a) An original image is first (b) binarized to highlight the still bright fireball. (c) A morphological filling operation is used to remove internal holes in the binarized image, and (d) the edge of the fireball region is extracted. (e) A final extracted edge is overlaid on the original image to verify the extraction.

high pixel intensity fireball, then morphologically filtered to reduce the impact of random noise and non-fireball objects. A morphological fill operation ensured that the detected fireball contour did not include interior changes in intensity, such as from the soot on the surface seen in Figure 2.17. The edge of the resulting binary object was extracted using the MATLAB *edge* command to create the fireball edge data. Figure 2.17 shows an example extracted fireball contour overlaid onto the source image.

To identify the time the shock wave detaches from the fireball, images from camera 3 were sequentially differenced to isolate changes between frames, then normalized between 0 and 1 to prevent over ranging. The density increase caused by the shock wave changes the index of refraction of the air. The distortion of the background image of the test site as a result of the shock wave caused refractive index change created a BOS effect [71, 109, 110]. The distinction between shock attached and shock detached frames allowed the identification of shock detachment time from the fireball. Figure 2.18 shows an example of the sequentially differenced frames highlighting the shock wave against the natural background.

The extracted fireball profile for the $f = 384.6$ rad/m 880 g charge at five

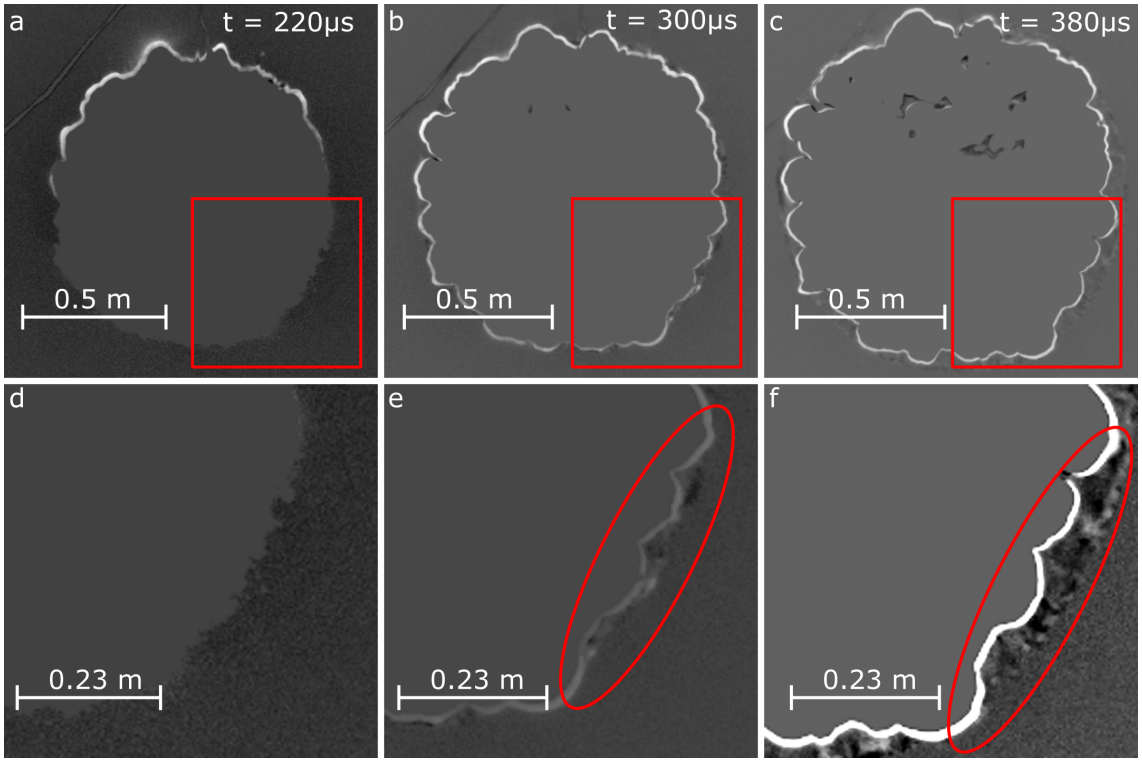

Figure 2.18: (a) Immediately before the shock begins separating from the fireball, there is no distortion of the background image, identifiable in background subtracted image by the smooth and consistent color gradient outside the fireball. (b) As the shock begins separating from the fireball, a distortion of the background can be seen between the peaks of the interface. (c) After a short time the shock is fully separated from the product gases and is fully visible around the perimeter of the fireball. (d, e, f) Zooming in to the indicated 160 pixel by 160 pixel region and performing a histogram stretch highlights the shock detachment process.

different time steps is plotted in Figure 2.19. The radius profile shows peaks and valleys roughly corresponding to the charge perturbation frequency. There was a broad variation that is attributed to the charge not being perfectly spherical. This variation was subtracted by calculating a local mean radius $\bar{R}_{loc}$ over the nearest 60 radii, and subtracting that average from each point, returning the zero centered variation in radius about a local average. The overall average radius for each time step $\bar{R}$ was then re-added to the variation to recover the corrected radii R_{adj}.

$$R_{adj} = R - \bar{R}_{loc} + \bar{R} \tag{2.6}$$

The $f = 384.6$ rad/m 880 g charges exhibited this phenomena particularly strongly. The evident change in average radius near 0 radians is removed while maintaining both the surface perturbations and overall average fireball radius. This process is applied uniformly to all perturbed sphere mixing region data.

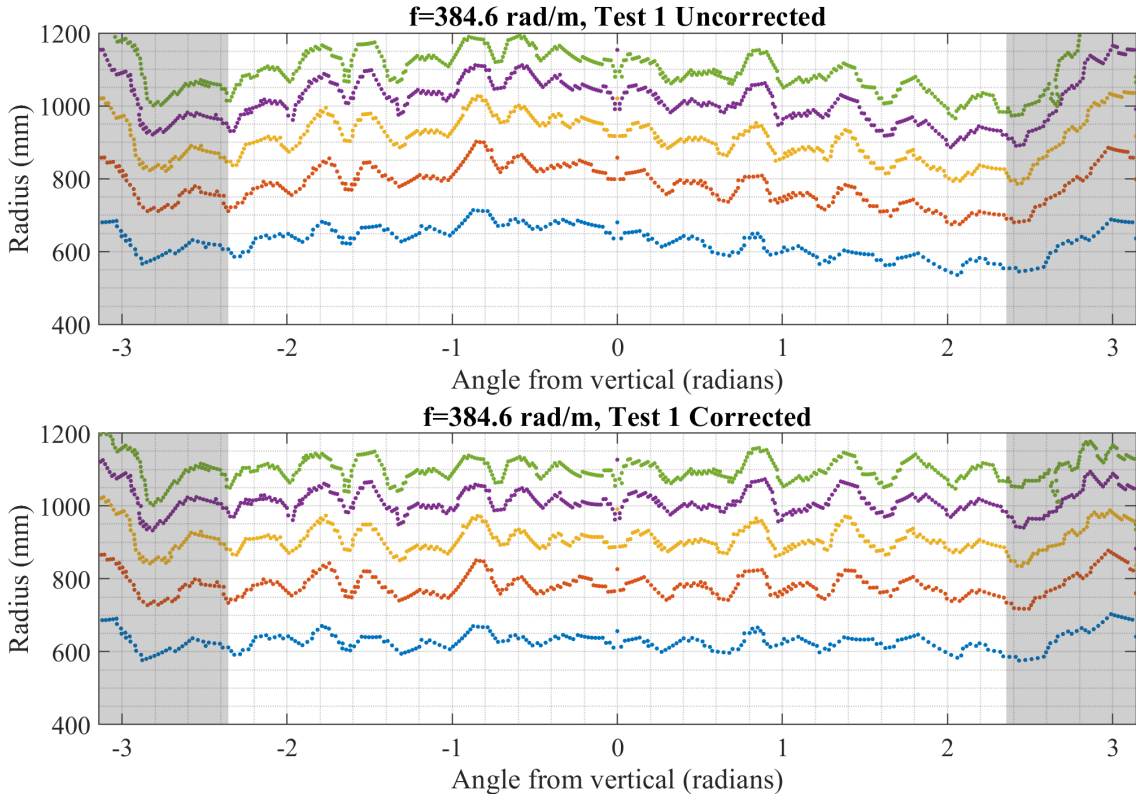

Figure 2.19: The extracted fireball contours for a 880 g $f = 384.6$ rad/m test before (top) and after (bottom) the moving average processing was applied. The contours shown are taken at $t = 0.15$ ms, $t = 0.225$ ms, $t = 0.3$ ms, $t = 0.375$ ms, and $t = 0.45$ ms (frame 30, 45, 60, 75, and 90). The shaded regions cover the position of the detonator, which is removed from radius and mixing calculations to avoid geometric effects.

The mixing region estimation methods used for the shotgun primer flows are relied on a optically transparent flow but the C4 fireball was optically opaque, which thus required a different estimation technique. To estimate the mixing region, the extracted radii were sorted by angle relative to the vertical. Radii within $\pi/4$ radians of the top of the charge were removed to limit the impact of the detonator well geometry on the results. The top and bottom 5% of radii were removed to limit the impact of singular jets on the overall measure. The mixing region width h for each time step was then calculated using Equation 2.7.

$$h = \frac{R_{max} - R_{min}}{2} \tag{2.7}$$

The intent was to mitigate the impact of a single peak or valley on the mixing width for the entire flow, while still capturing the behavior on the extremes. This measure also corresponds roughly to the 5%-95% rule for mixing width descriptions in modeling [98, 111]. Figure 2.20 shows the mixing widths overlaid onto the data from the same $f = 384.6$ rad/m 880 g charges shown in Figure 2.19. The mixing width was seen to be well described by this method.

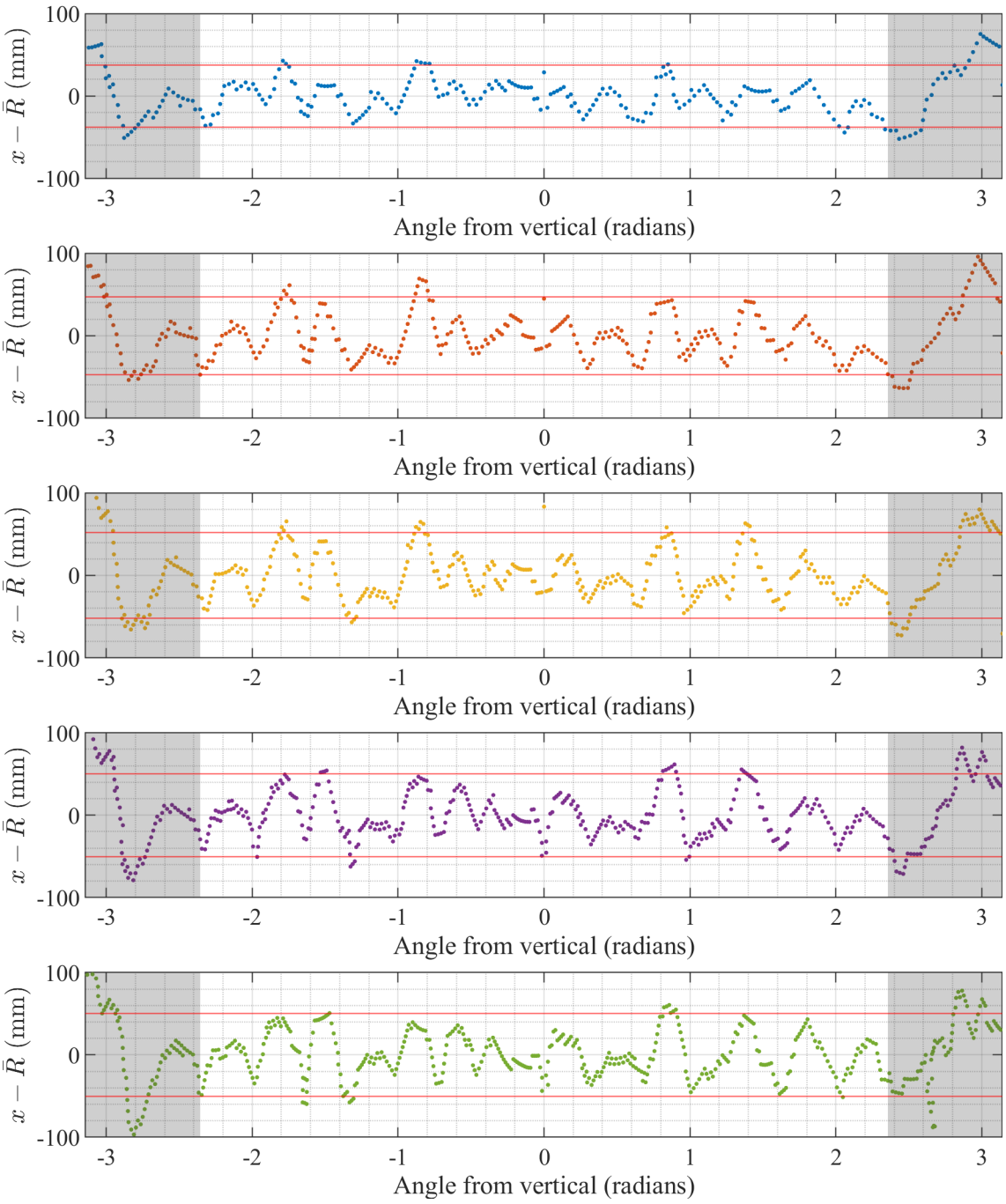

Figure 2.20: The mixing widths (red lines) for the fireball radii shown in Figure 2.19. From top to bottom, $t = 0.15$ ms, $t = 0.225$ ms, $t = 0.3$ ms, $t = 0.375$ ms, and $t = 0.45$ ms. The fireball radii are plotted relative to the mean radius for that frame.

CHAPTER 3

CONSIDERATIONS FOR THE ESTIMATION OF THE FRACTAL DIMENSION

Digital image processing techniques were developed to identify the contour of the fireball, which was then examined to determine the fractal dimension as a function of time.. Three-dimensional data was used to validate the 3D isotropy of the fractal measurement to within its error. Experiments were conducted with explosive masses of 1 g, 105 g, and 880 g scales to study the impact of scale on the evolution of the fractal dimension.

3.1 Computation of the fractal dimension for high speed images

High speed cameras have both advantages and disadvantages for the successful estimation of fractal dimension. The low pixel resolution of imaging sensors increases in the uncertainty in the estimated fractal dimension, as many desired spatial scales may fall below the imaging resolution of the cameras. Low exposure times allow the capture of sharp boundaries not blurred by motion, making the best use of the available resolution. The dimensional symmetry properties of fractals enables a single camera view to capture a fractal dimension that is representative of the entire flow.

3.1.1 Box counting methods

The fractal dimension of all tests was computed using a standard two dimensional fixed grid box counting algorithm. In box counting, an evenly spaced grid is placed over a fractal, and the number of boxes containing the fractal is counted. This processes is repeated using progressively finer grids until the spacing of the grid $s \rightarrow 0$. For digital images, the grid is refined by the pixel resolution of the imaging sensor. Images that have been processed by edge detection routines were used, and a fractal dimension D_F was estimated with

$$D_F = \lim_{s \to 0} \frac{\log(n(s))}{\log(1/s)} \tag{3.1}$$

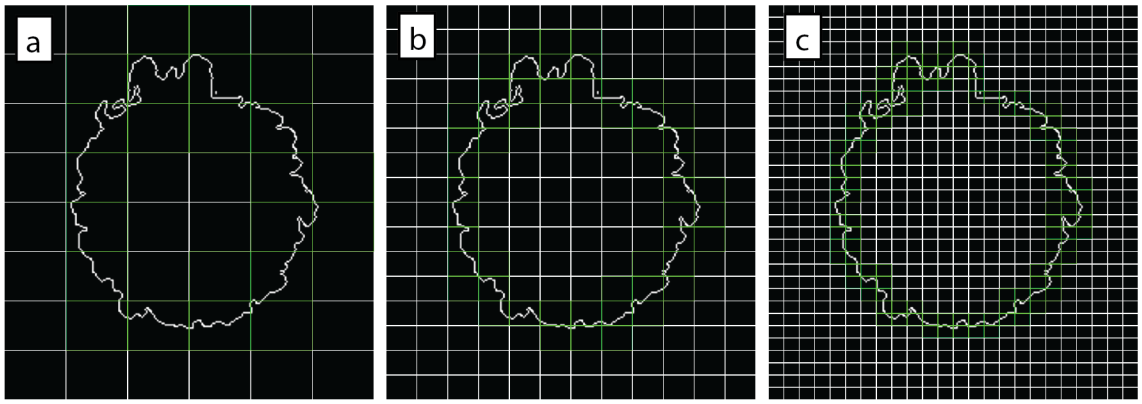

Figure 3.1: The progression of the box counting algorithm on a fireball from a perturbed sphere. The boxes progress from (a) a large size box down to an (b) intermediate and (c) small sized box. The green boxes represent a portion of the white grid which contains a section of the fractal. The image has been cropped tightly to the fireball for the purposes of this figure.

which is a discrete derivative of Equation 1.35. Where $n(s)$ is the number of boxes containing the curve at box scale s. The box scale s is the side length, in pixels, of the boxes at that scale, and is a function 2^x, where x is the depth. Figure 3.1 shows an example of several intermediate steps of a box counting algorithm. The limit was estimated by the inverse slope of a linear least squares fit in the log-log space as shown in Figure 3.2. The box counting dimension, or Minkowski-Bouligand dimension, is analogous to the Hausdorff dimension for fractals that satisfy the open set condition. Being natural fractals, it is not known if fireball contours satisfy this condition. However, the box counting dimensions is a strict upper bound on the Hausdorff dimension when converged, so its use here is appropriate [48].

3.1.2 Fractal uncertainty

The fractal dimension is calculated by computing a least-squares best fit of a line to a number of data points equal to the number box counting scales. The uncertainty in the fractal measurement was identified in the uncertainty of the least squares fit to the data. The y-intercept of the fit was not used in these analyses. The uncertainty of the slope σ_B of the least-squares fit is a function of the number of samples N and of the data points (x_i, y_i) being fit[112],

$$\sigma_B = \sqrt{\frac{1}{N-2}\sum_{i=1}^{N}\left(y_i - \frac{\sum x^2 \sum y - \sum x \sum xy}{\Delta} - \frac{N\sum xy - \sum x \sum y}{\Delta} x_i\right)^2}\sqrt{\frac{N}{\Delta}}$$

where

$$\Delta = N\sum x^2 - (\sum x)^2$$

The uncertainty of the fractal measurement is therefore directly related to the size of the image and the number of fractal scales that can be represented. This means that the overall uncertainty is relatively constant throughout the evolution of the fireball. Figure 3.2 shows a representative fractal fit with the 95% confidence bounds overlaid. The box counting algorithm works best with square images

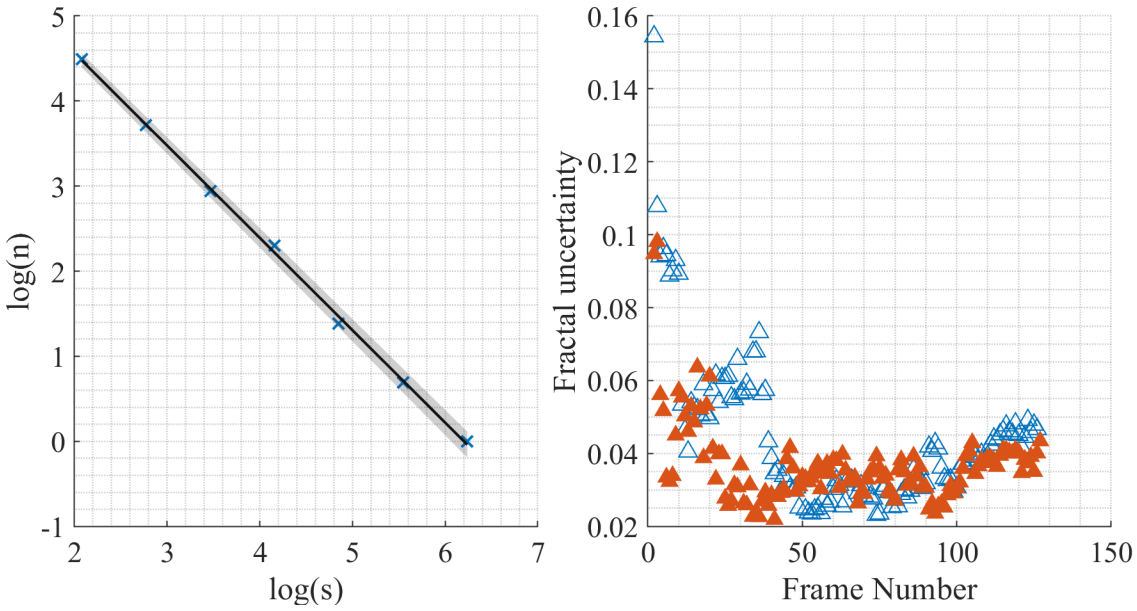

Figure 3.2: The uncertainty of the fractal dimension is tied to the goodness of fit parameters for the linear regression of the slope between fractal scale and fractal counts. The 95% confidence interval of the fit (left) is seen in the outer shaded region. The maximum uncertainty (right) across all tests for each frame number shows that the systematic uncertainty due to fitting drops as the fireball expands to cover more of the image.

with side lengths of 2^x pixels. When images are not square, the algorithm pads the images with black pixels. The 400 x 250 pixel images used in this study were padded to 512 x 512 before processing. This has the effect of slightly reducing the estimated dimension, but was minimal here and within the calculated uncertainty.

3.1.3 Sensitivity of box counting methods to image size

The Shimadzu HPV-X2, the primary diagnostic camera used in this study, has a sensor size of only 400 x 250 pixels. The impact of low resolution images on

the measured fractal dimension was studied using multiple images of the same known fractal at different resolutions. Three fractals where chosen for analysis. The Sierpinski's Carpet fractal and the Vicsek fractal, both shown in Figure 3.3, were chosen for their ease of generation and square aspect ratio. The third fractal is the Douady rabbit, a member of the Julia set. The Julia set is a set in complex dynamics where a small perturbation can cause large variance in the computed value of a function, and is a common source for generating fractals.

To generate a Sierpinski's Carpet, an area is sub-divided into 9 equal areas, and the center area is removed. In matrix form,

$$\begin{Bmatrix} 1 & 1 & 1 \\ 1 & 0 & 1 \\ 1 & 1 & 1 \end{Bmatrix} \rightarrow \begin{Bmatrix} 1 & 1 & 1 & 1 & 1 & 1 & 1 & 1 & 1 \\ 1 & 0 & 1 & 1 & 0 & 1 & 1 & 0 & 1 \\ 1 & 1 & 1 & 1 & 1 & 1 & 1 & 1 & 1 \\ 1 & 1 & 1 & 0 & 0 & 0 & 1 & 1 & 1 \\ 1 & 0 & 1 & 0 & 0 & 0 & 1 & 0 & 1 \\ 1 & 1 & 1 & 0 & 0 & 0 & 1 & 1 & 1 \\ 1 & 1 & 1 & 1 & 1 & 1 & 1 & 1 & 1 \\ 1 & 0 & 1 & 1 & 0 & 1 & 1 & 0 & 1 \\ 1 & 1 & 1 & 1 & 1 & 1 & 1 & 1 & 1 \end{Bmatrix}$$

The processes is recursively repeated. The exact Hausdorff dimension of Sierpinski's Carpet is 1.8928, calculated by

$$D_F = \frac{\log 8}{\log 3} = 1.8928$$

The Viscek fractal is generated by taking a plus sign, and recursively replacing the arms with smaller plus signs. In matrix form,

$$\begin{Bmatrix} 0 & 1 & 0 \\ 1 & 1 & 1 \\ 0 & 1 & 0 \end{Bmatrix} \rightarrow \begin{Bmatrix} 0 & 0 & 0 & 0 & 1 & 0 & 0 & 0 & 0 \\ 0 & 0 & 0 & 1 & 1 & 1 & 0 & 0 & 0 \\ 0 & 0 & 0 & 0 & 1 & 0 & 0 & 0 & 0 \\ 0 & 1 & 0 & 0 & 1 & 0 & 0 & 1 & 0 \\ 1 & 1 & 1 & 1 & 1 & 1 & 1 & 1 & 1 \\ 0 & 1 & 0 & 0 & 1 & 0 & 0 & 1 & 0 \\ 0 & 0 & 0 & 0 & 1 & 0 & 0 & 0 & 0 \\ 0 & 0 & 0 & 1 & 1 & 1 & 0 & 0 & 0 \\ 0 & 0 & 0 & 0 & 1 & 0 & 0 & 0 & 0 \end{Bmatrix}$$

The exact fractal dimension of the Vicsek fractal is 1.465, calculated by

$$D_F = \frac{\log 5}{\log 3} = 1.465$$

Both the Sierpinski carpet and Vicsek cross fractals use generators represented on a 3 by 3 matrix, and are well suited to matrix based computation.

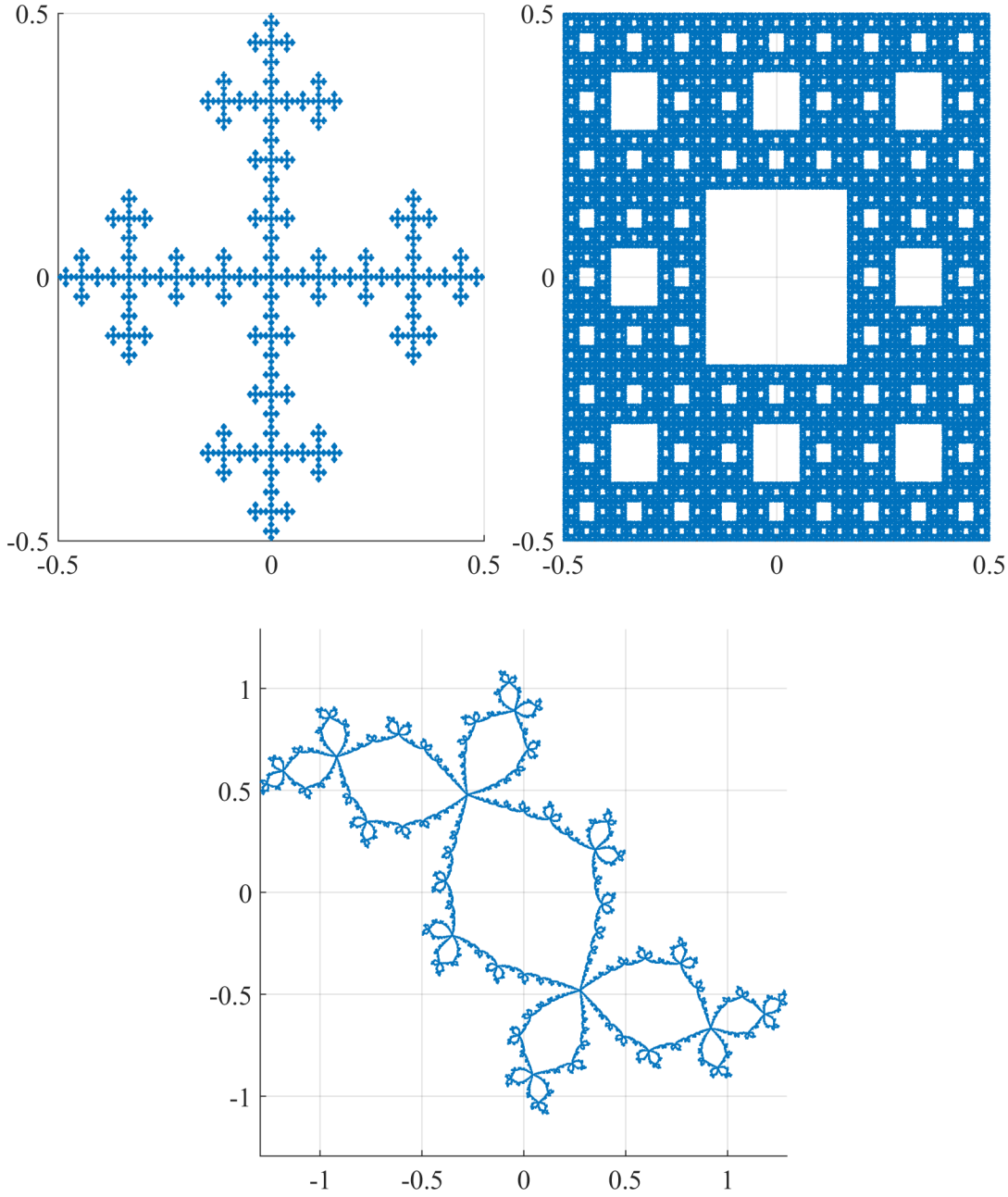

Figure 3.3: The Vicsek fractal (Top left) and Sierpinski Carpet fractal (Top right) are presented normalized between -0.5 and 0.5 in both x and y. The Douady rabbit (bottom) normalized between [-1.5,1.5].

The Douady rabbit generated by iterating the Mandelbrot set map,

$$z = z^2 + c$$

where c is a fixed complex number. In this case, $c = -0.123 + 0.745i$. The computed fractal dimension of the boundary of this set is 1.3934.

Here a high resolution fractal was first generated using MATLAB. For the Vicsek and Sierpinski fractals, this was 150,000,000 points over 9 fractal scales. For the Douady rabbit, a set of 1,589,222 points was computed to a depth of 300 iterations. The chosen size of fractals was memory limited during computation. A synthetic image of the fractal was then generated at a fixed resolution. Images are generated with 100 linearly spaced side lengths between 2 and 2^{14}. Each image is generated by determining the total number of fractal points contained by each pixel, then applying a universal threshold to create a binary image of fractal pixels. The fractal dimension of each image was then estimated by box counting. As is shown in Figure 3.4, the estimated fractal dimension converges closest to the true fractal dimension when the image size is a power of 2. The chosen fractals show opposing behavior. The Vicsek fractal overestimated the calculated dimension by up to 9.5% consistently before dropping to near the expected value. The Sierpinski fractal behaved inversely, approaching the calculated value from below then dropping to underestimate the dimension by 6.1%. The Douady rabbit, despite being the most non-rectangular, had the best error, with a max deviation of 5.6% from the Hausdorff dimension. This bounding behavior occurs consistently regardless of the full size of the image, and is expected with the boxcounting algorithm. This establishes the expected error for box counting algorithm on small images, which is found to be less than 10% from the expected fractal dimension and not a strong function of the image size. This indicates that the small image sizes used in here still accurately represent the fractal dimension of the fireball contours.

3.2 Consistency of fractal dimension with respect to rotation

Explosive events are frequently studied using low order models that make significant assumptions about the symmetry of the event. For example, one dimensional radial models assume spherical or cylindrical symmetry. For the application of fractal dimension to the complete fireball surface, the assumption is made that surface complexity is evenly distributed across the surface. For the perturbed sphere test series, all charges had axially symmetric geometry about the initiation point, with perturbations being made entirely in the azimuthal direction. All other charges considered were nominally radially symmetric about the long axis of the detonator. A planar slice taken from any imaging angle is assumed to have the same fractal dimension as any other slice that passes through the center point of the blast. As such, the estimated fractal dimension D_2 of a 2D slice is taken to be representative of the estimated fractal dimension D_3 of

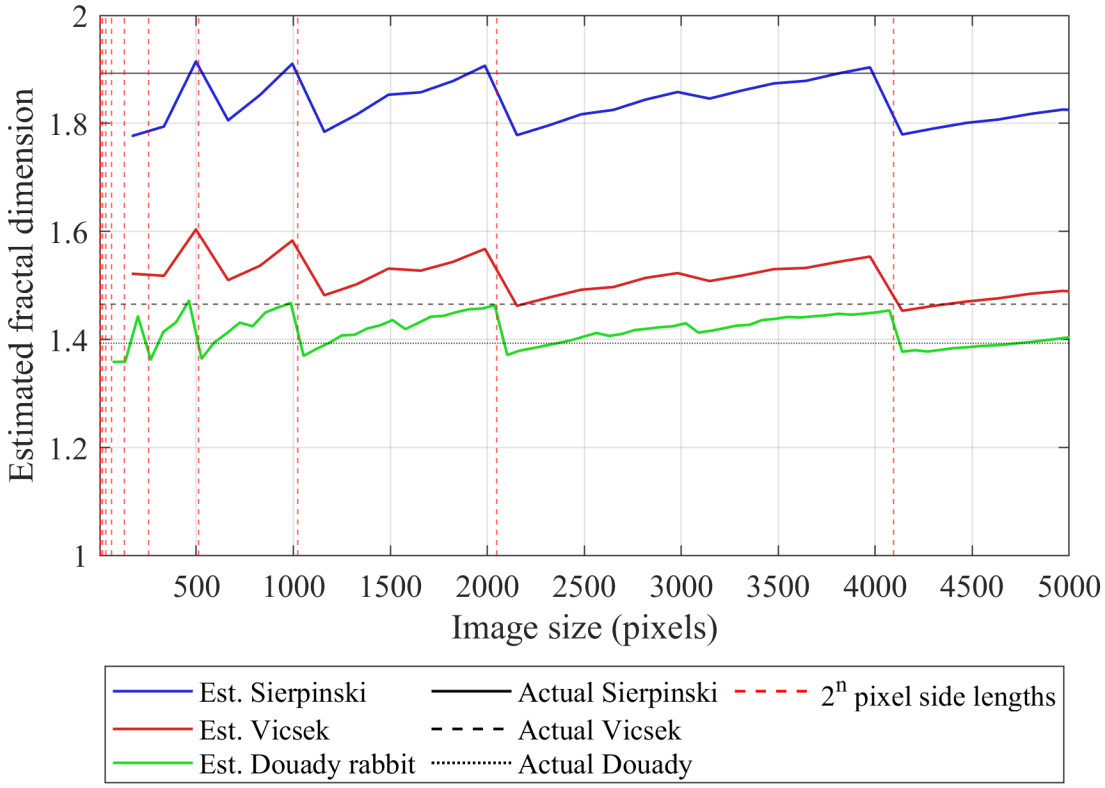

Figure 3.4: The estimated fractal dimension as a function of image size side length, with the exact fractal dimension for each fractal as a black horizontal line.

the 3D surface represented by the fireball. This is supported by the additive rule of fractals [42, 56], which states that the fractal dimension of the plane interesting the three dimensional fractal object with dimension D_3 will be related by $D_3 = D_2 + 1$. Experimental results using multiple camera angles further reinforce the validity of this assumption.

To confirm that the measured fractal dimension of a fireball is consistent regardless of fireball orientation, images of a single explosion from 5 different viewing angles were processed to extract the time resolved fractal dimension. The experiment was performed three times by detonating a 1.32 kg spherical charge with constant camera positions. The period of validity for these fireballs runs from $t = 0$ ms to $t = 2.6$ ms, or 0 to 0.236 scaled time. The behavior of the fractal dimension for all 5 cameras for all three tests is shown in Figure 3.5.

To determine variation, a mean fractal dimension was computed for every time step. Percentage difference from the mean was computed for all cameras, and is reported in Figure 3.6. For the first frames, estimated fractal dimension is highly variant. The extracted boundary contains few pixels spread over a small portion of the image, so large deviation is expected in the early time. Past 1 ms, the extracted fractal is largely consistent, with the deviation from the mean fractal falling to within 10%. In Figure 3.7, each camera shows good consistency from test to test. The 0° camera has both the most usable data points and the tightest grouping. The sudden drop in the 45° camera at approximately $t = 1.5$ ms is seen in two of the tests but not the third. This time coincides approximately with the fireball beginning to interact with the shock reflection plate, which complicated the fireball extraction, and may distort the expected fractal evolution.

In these tests, the fireball begins to exit the individual fields of view at different times, which changes the percentage of the fireball interface visible. A mathematical fractal is scale invariant, and will return the same fractal dimension regardless of the section measured [42]. The fireball exiting the field of view should therefore have minimal impact on the extract fractal dimension as long as there are sufficient boundary data points available. Once the fireball begins to exit the horizontal field of view, the number of points on the edge of the fireball drops. A similar trend occurs when the fireball is occluded, creating two separate curves divided by a non-fractal object. As a result of these behaviors, fractal data collection was stopped once the fireball was either obstructed by an object or exited the horizontal field of view.

The fractal dimension of a fireball measured by box counting is found not to vary as a function of the viewing angle. This validates the assumption of axial symmetry throughout all three-dimensional testing, and supports the conclusion that the fractal dimension is representative of the fireball as a whole.

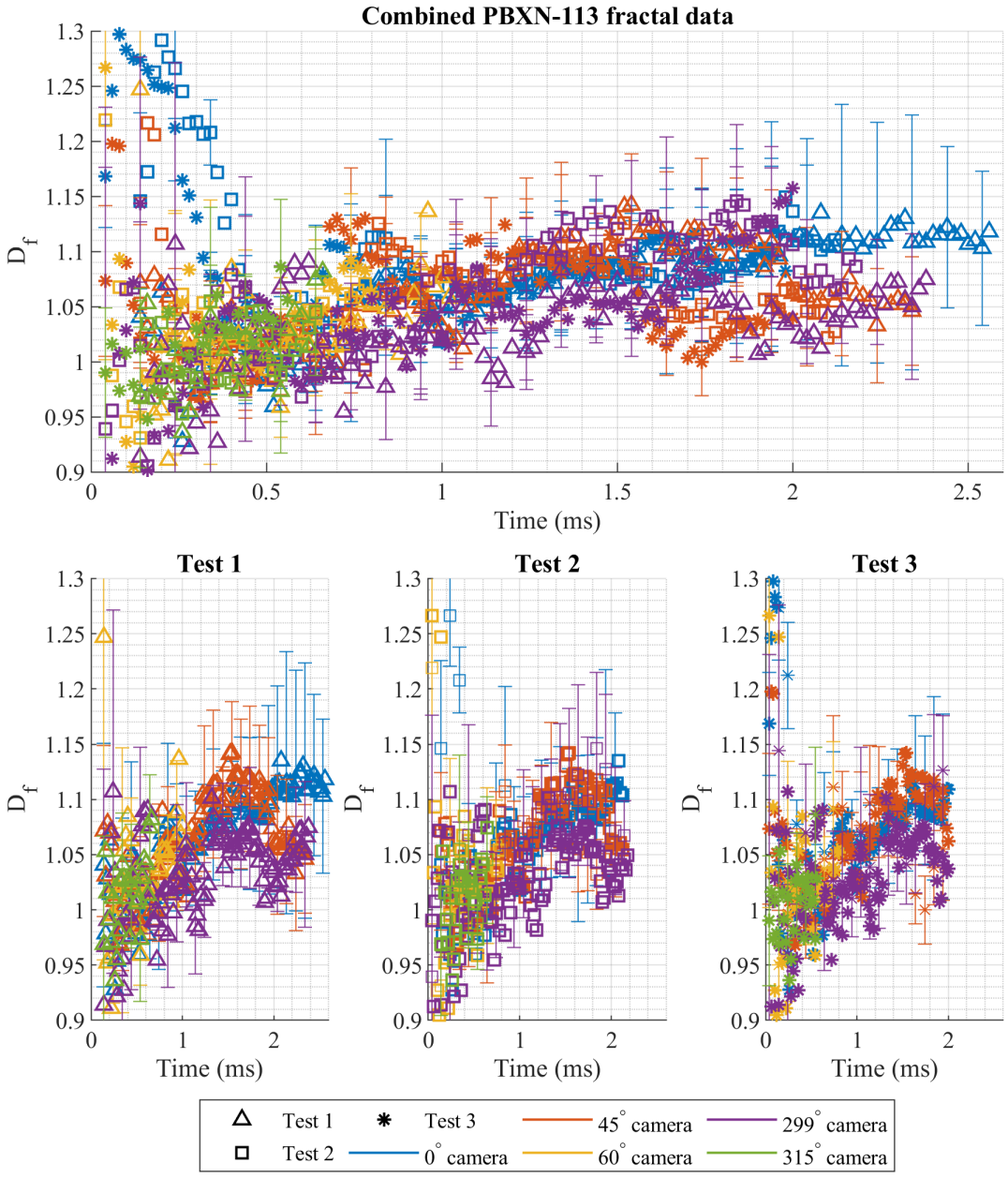

Figure 3.5: (top) Estimated fractal dimension for all 5 camera angles across all 3 tests. (bottom) Data from each individual test from all angles for the three repeats performed. There is high dispersion in the early time, but all cameras return to the same trend beyond about 1 ms.

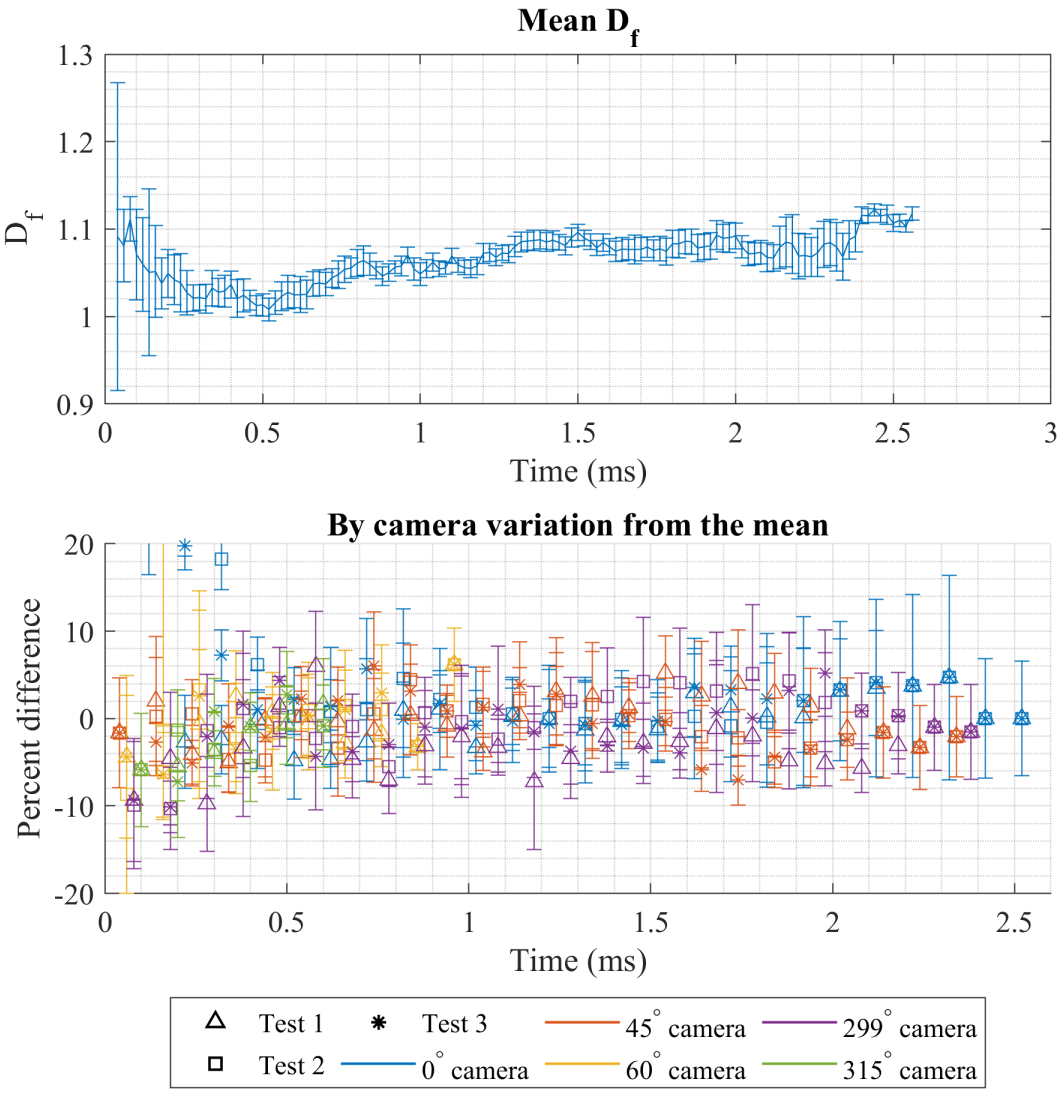

Figure 3.6: The mean fractal dimension (top) of all tests and camera angles shows a steady trend. The initial variation from that mean (bottom) is large, but falls to consistently below 10%. The measured fractal dimensions are within the uncertainty of the mean fractal dimension for all camera angles.

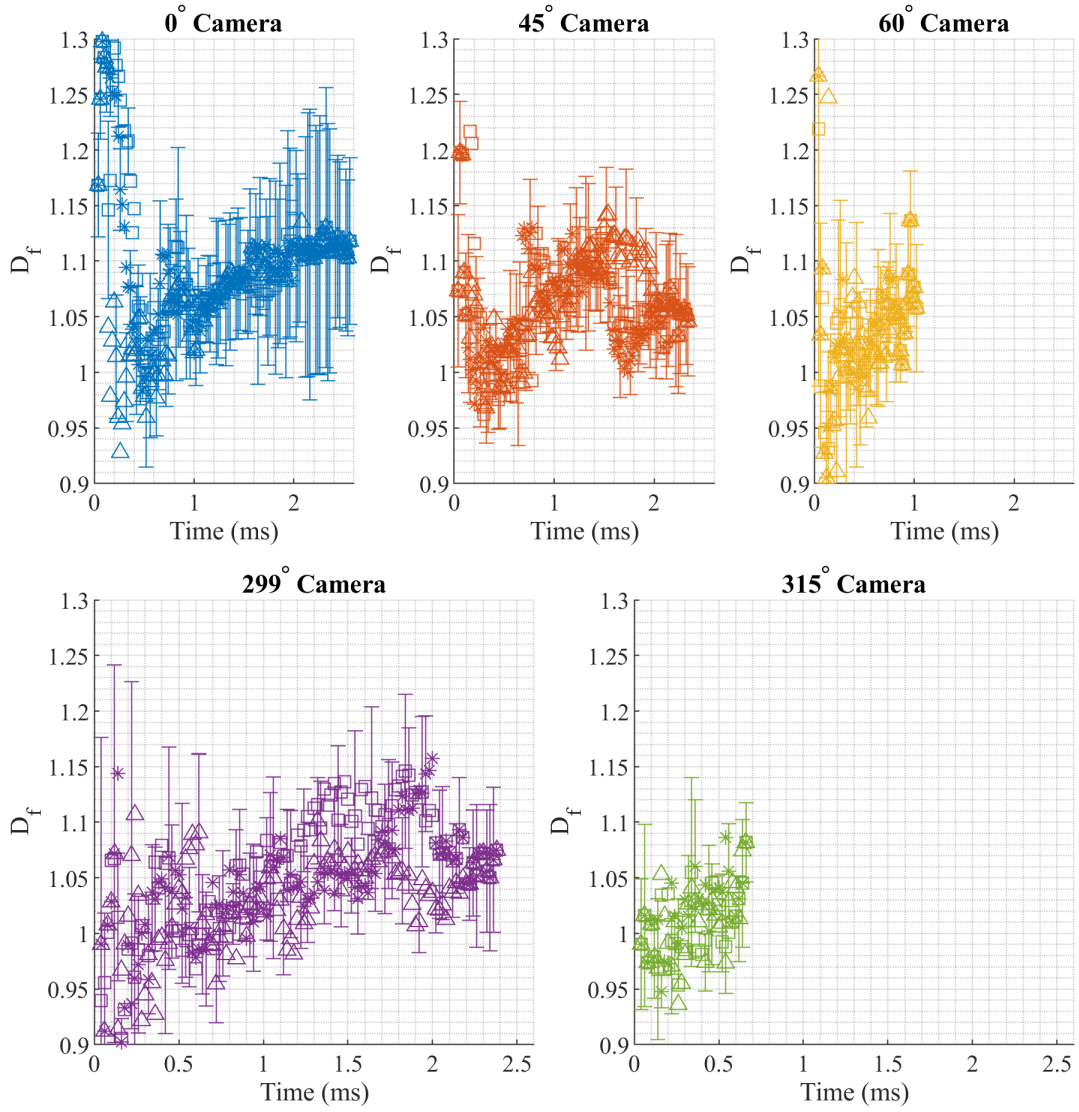

Figure 3.7: The fractal dimension of each independent camera broken down by test. The 60° and 315° camera data ends at earlier times because the fireballs either exit the field of view or become obstructed.

CHAPTER 4

FIREBALL DIMENSIONS AND CHARACTERISTIC LENGTHS

To determine the mixing region width and fractal dimension of the fireballs extracted from experiments, spatially and temporally resolved radius data was required for all tests. The discussion of results first covers baseline measurements of fireball radius and the determined characteristic lengths and times. Time resolved radius data is reported for all tests alongside discussions of any critical features of the fireball radius evolution. The data was extracted for all fireballs as a function of the explosive charge center, the angular position on the fireball, and the elapsed time post-detonation. The scaling criteria for supporting data is discussed, and scaling variable values are reported. While spatially averaged radius data is presented here as a function of only time, when determining mixing region width the spatial component of the radius data is important, and representative fireball edges will be presented here.

4.1 Fireball and gas cloud radius data

To validate the bulk behavior of the fireball, the temporally and spatially resolved radius of the fireball contours was computed for all data sets. Spatial resolved data is temporally averaged to determine a bulk fireball radius for each time step. While averaged data is presented here, including averaging over repeated tests, a full test-by-test breakdown of radius data can be found in Appendix B. For real explosive events, the contour of the fireball surface is not a smooth circle, so an average radius is used. As shown in Figure 4.6, the average radius is a good representation of the bulk behavior of the fluid.

Shotgun primer radius data is presented averaged by confinement spacing in Figure 4.1. Radius data was collected from the first detection of a gas cloud radius greater than the primer gun radius up until either reshock from outside the test section or the from the gas cloud test section. The large variance between peaks and valleys in the lower confinement cases is characteristic of the introduction of mixing along a curved front as the cloud expands towards the confining plate as described in Figure 2.3.

The radius data for all PBXN-113 tests is broken down by camera angle and test number in Figure 4.1. Radii are reported until the fireball was either obscured or exited the sides of the field of view. The camera positions to either

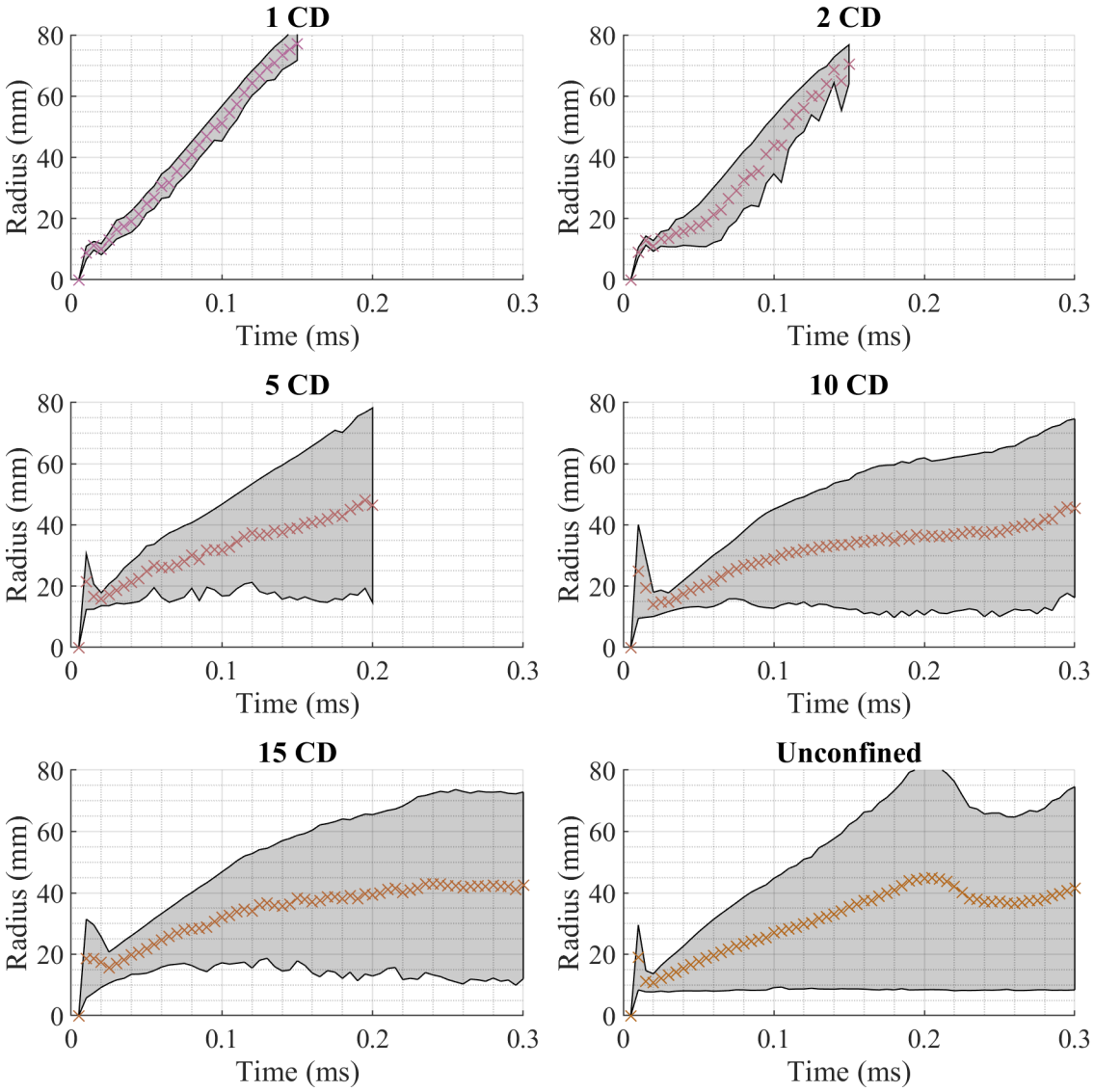

Figure 4.1: Averaged radius data for all confinement levels. One charge diameter (CD) is 2.4 mm.

side were more quickly obscured by the support frame for the charge, and have correspondingly shorter record lengths.

The radius data for both gram scale tests is shown in Figure 4.3. Radius is measured from whenever the product gas cloud is first visible to the end of recording. In the gram scale case, the bandpass filter limits the visualization of light produced within the test section. This prevents the detonation from washing out early time diagnostic information. It also prevents the use of illumination based metrics for the identification of the fireball. The optical density of the fireball remains high, however as Primasheet 2000 has a high soot production that renders the fireball largely opaque. The identification of the fireball is therefore the inverse of the direct imaging tests, and focuses on locating the edge of the optically dense region centered on the detonation event. The radius results presented here are in line with the other tests conducted. The gap in the detected radius measurements at around 0.2 ms is representative of the secondary shock detaching from the fireball and being detected instead of the fireball. Data was manually inspected to identify affected frames and they were removed. The impacted times were not the same between charges.

The radius data for the 105 g and 880 g test series are shown in Figure 4.1 and Figure 4.1 respectively, averaged by initial perturbation. Radius data is presented from the first frame a full fireball contour could be extracted, until the validity of the fireball extraction ends. The radii reported here are spatial averages representative of the bulk fluid flow, as shown in Figure 4.6.

A start of validity (SoV) and end of validity (EoV) frame is determined for each test. The exact cutoff criteria varied for each test series based on imaging requirements. Typical reasons for the identification of SoV and EoV include the fireball exiting the frame, or a change in the imaging characteristics of the fireball. As the fireball begins to exit the field of view, the number of points over which the average radius is calculated is reduced. Figure 4.7 shows the evolution of an extracted profile from fully visible to only partially visible to almost completely exiting the frame. Once enough of the fireball contour has exited the frame, there is little confidence that the small sections of fireball visible are representative of the full fireball behavior. Additionally, changes in the quality of the contour extraction as a result of changing image characteristics will also end the validity. After the EoV time the results are not reported.

Table 4.1 shows the start and end of validity for the primer driven gas expansion. Laser illuminated collimated imaging does not have issues with over exposure due to detonation, so the first frame of gas expansion was valid. The principal drivers of EoV in the primer tests were shock interactions with the gas cloud and exiting the field of view. Both were very consistent, so the start and end of validity frames were very consistent.

Table 4.2 reports the SoV and EoV frames for the tests with PBXN-113. Initial camera wash out was minimal for these tests, so the fireball exiting the field of view was the primary driver of validity ending.

The gram scale charges had to be visible around the central obstruction in

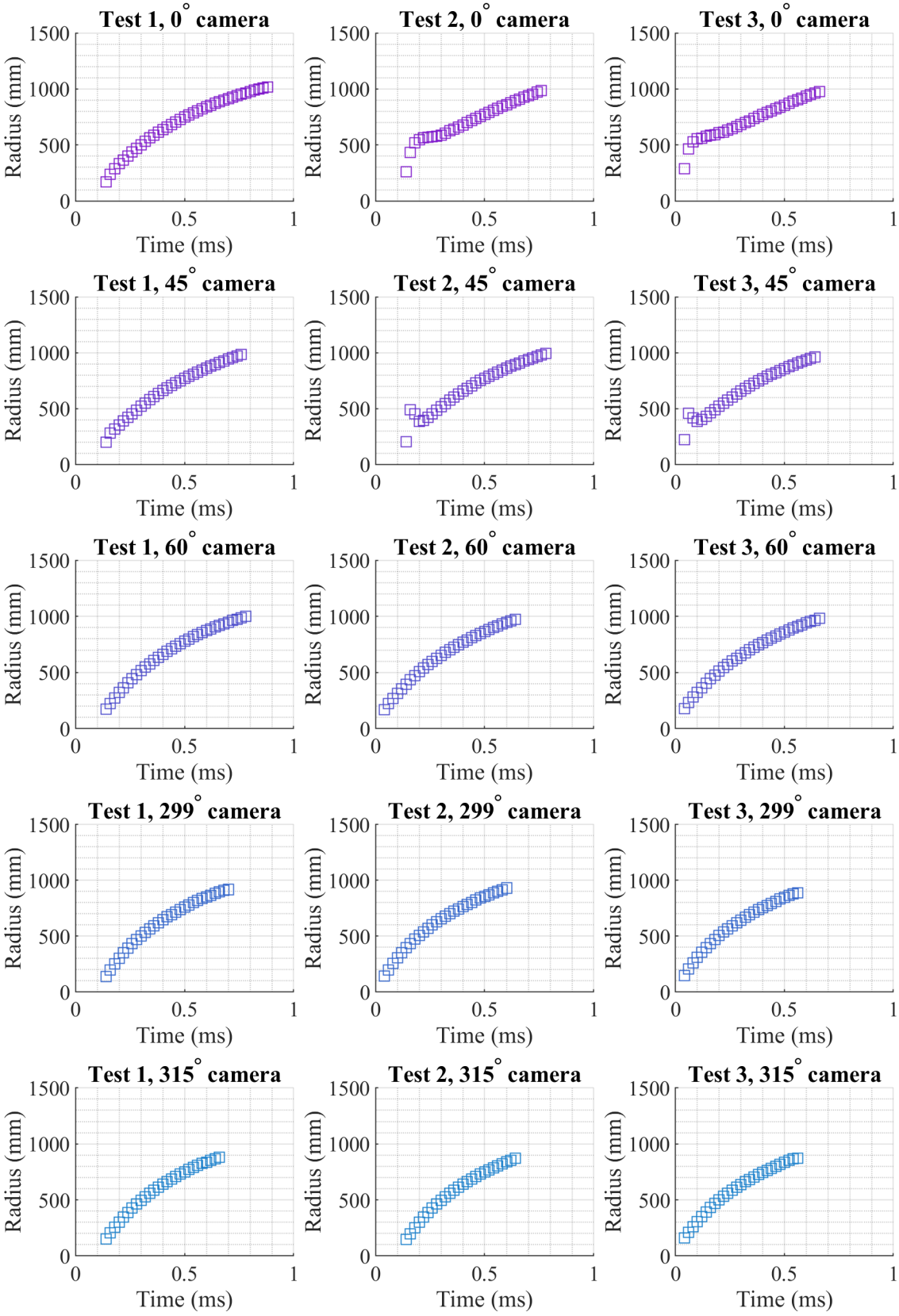

Figure 4.2: Radius data from all PBXN-113 tests organized by test number (vertical) and camera location (horizontal).

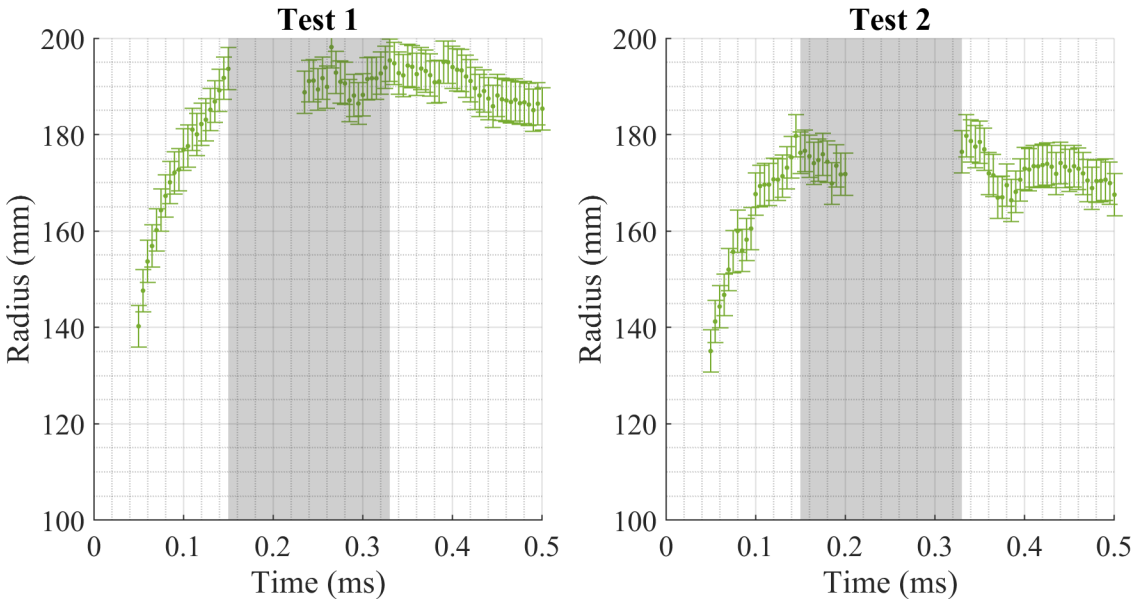

Figure 4.3: Gas cloud radii extracted from gram scale charges. The radius plateaus about halfway through the test. The shaded region indicates interaction between the gas cloud and secondary shock.

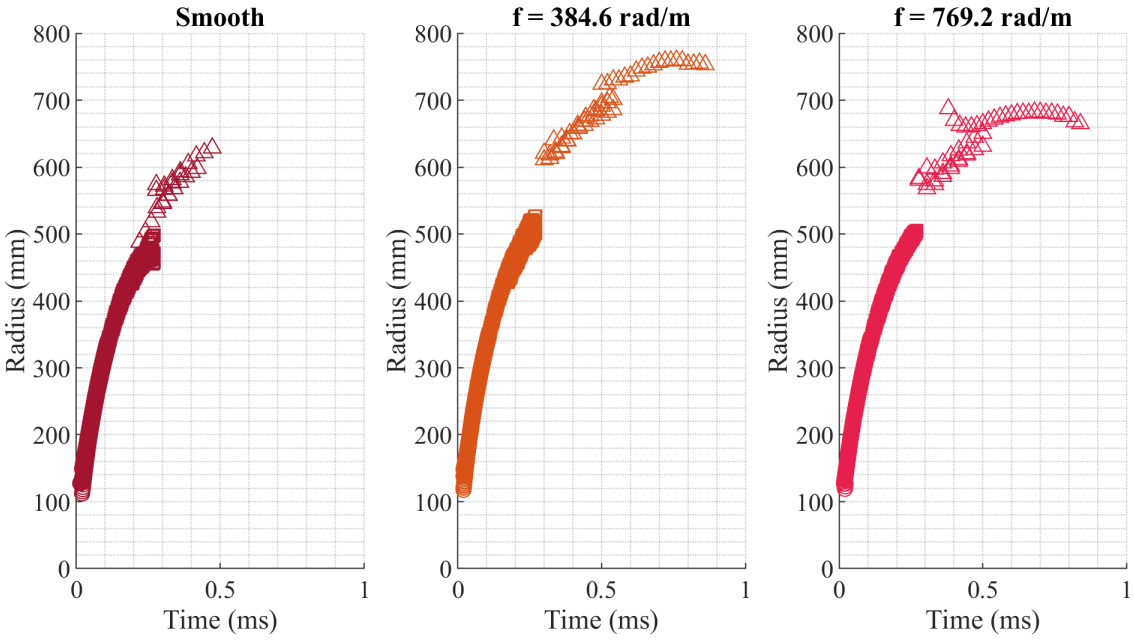

Figure 4.4: Radius data for the 105 g charges. The 3 cameras are represented by circles (○), squares (□), and triangles (△) respectively.

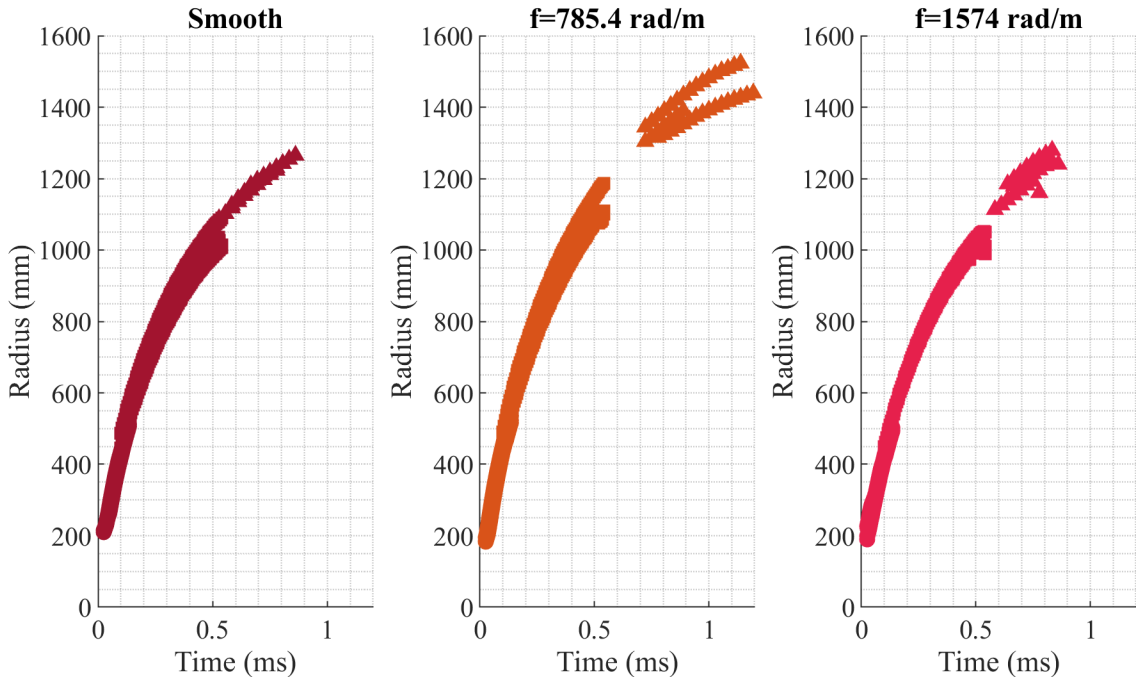

Figure 4.5: Radius data for the 105 g charges. The 3 cameras are represented by circles (○), squares (□), and triangles (△) respectively.

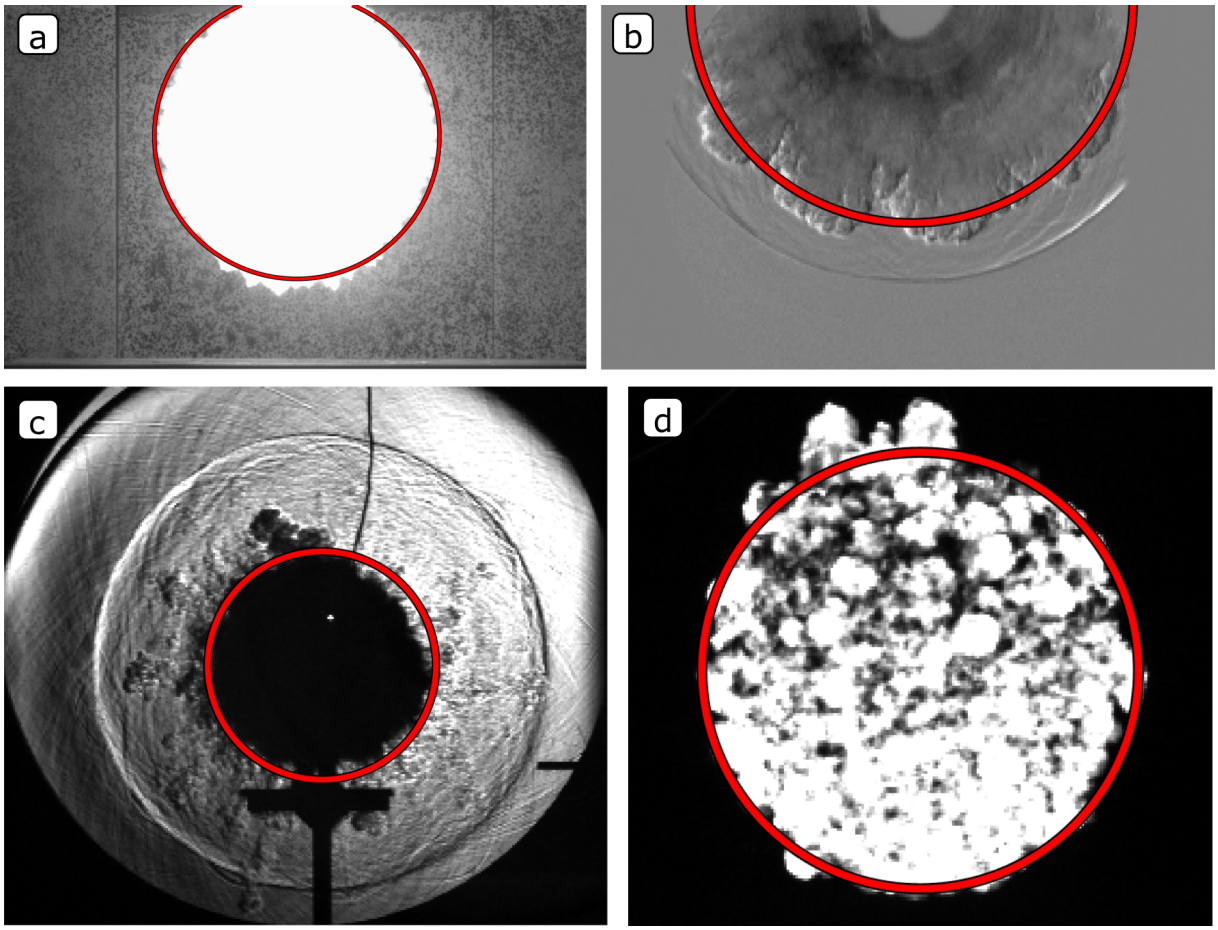

Figure 4.6: Representative overlaid extracted radii from (a) 1.32 kg PBXN-113 charges at Eglin AFB, (b) product gas cloud from a shotgun primer, (c) 1 m schlieren images of 1 gram C-4, and (d) the fireball from a 105 g C-4 charge.

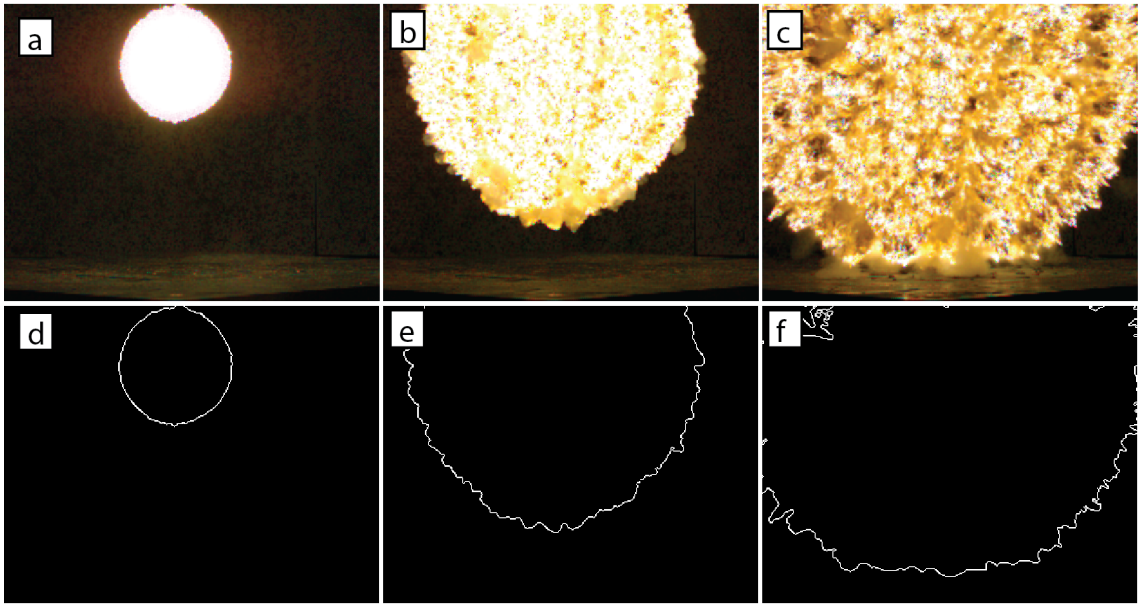

Figure 4.7: (a, b, c) Direct images and (d, e, f) extracted fireball surface contours for and expanding PBXN-113 charge. A fireball begins (a, d) fully in the field of view of the cameras, occupying a small number of pixels near the center of the image. As the fireball expands (b, e) it begins to exit the field of view, reducing the proportion of contour visible to the cameras. After some time, the fireball (c, f) nearly completely exits the field of view, and only a small fraction of the overall contour is visible.

Table 4.1: The start of validity and end of validity frame numbers for primer driven gas expansion in varying confinement. The camera frame rate was 200,000 fps.

	1 CD		2 CD		5 CD		10 CD		15 CD		Open Faced	
Test #	SoV	EoV	SoV	EoV	SoV	EoV	SoV	EoV	SoV	EoV	SoV	EoV
1	1	30	1	30	1	40	1	60	1	60	1	60
2	1	30	1	30	1	40	1	60	1	60	1	60
3	1	30	1	30	1	40	1	60	1	60	1	60
4	1	30	1	30	1	40	1	60	1	60	1	60
5	1	30	1	30	1	40	1	60	1	60	1	60
6	1	30	1	30	1	40	1	60	1	60	1	60
7	1	30	1	30	1	40	1	60	1	60	1	60
8	1	30	1	30	1	40	1	60	1	60	1	60
9	1	30	1	30	1	40	1	60	1	60	1	60
10	—	—	1	30	1	40	1	60	1	60	1	60
11	—	—	1	30	1	40	1	60	1	60	—	—
12	—	—	1	30	1	40	1	60	1	60	—	—
13	—	—	—	—	—	—	1	60	—	—	—	—
14	—	—	—	—	—	—	1	60	—	—	—	—

Table 4.2: The start of validity and end of validity frame numbers for tests with PBXN-113. The camera frame rates were 50,000 fps.

	0° Camera		45° Camera		60° Camera		299° Camera		315° Camera	
Test #	SoV	EoV	SoV	EoV	SoV	EoV	SoV	EoV	SoV	EoV
1	1	37	1	31	1	32	1	28	1	26
2	1	31	1	32	1	30	1	28	1	25
3	1	31	1	30	1	31	1	26	1	26

the imaging system, and took a consistent number of frames to reach that point. There were no reflected shocks or exits from field of view, so validity extended for the full record length, as seen in Table 4.3.

Table 4.3: The start of validity and end of validity frame numbers for gram scale tests. The camera frame rate was 100,000 fps.

	Camera 1	
Test Number	SoV	EoV
1	10	128
2	10	128

The SoV and EoV frames for the 105 g and 880 g perturbed charges are presented in Tables 4.4 and 4.5, respectively. Washout and bloom in the very early frames of camera 1 prevent reliable fireball identification until about halfway through the data, though the fireball was consistently visible out to the end of recording. Camera 2 experienced the opposite issue, where the short exposure required to capture the early evolution reduced effective contrast between the fireball and the background at later times. This was an intentional trade-off to ensure data overlap between the two primary cameras. Camera 3 was configured for late time context imaging, and had relatively few properly exposed frames of the fireball.

4.2 Characteristic lengths and times for fireball and mixing diagnostics

Characteristic values for length and time were calculated for each test series, and are presented in Table 4.6. For characteristic values impacted by atmospheric conditions, an average value is reported here. The shotgun primer flow scaling parameters are calculated and presented for completeness, but it was not expected that scaling for spherical explosions would accurately capture the dynamics of the flow in these confined tests. Instead, dynamics are normalized by the charge diameter (2.4 mm). A complete listing of all values by test can be found in Appendix B.

4.2.1 Scaling behavior

As shown in Figure 4.8, a fluid dynamic scaling scaling based on explosive energy and ambient fluid characteristics (speed of sound) is effective at reducing the radius-time plot to a single effective curve. Dispersion appears to increase as the fireball radius plateaus, but is otherwise small. For free-air blasts, Sedov and Wei-Hargather scalings report nearly identical values, so both scalings are equally effective. Figure 4.9 demonstrates the mean radius and velocity of the

Table 4.4: The start of validity and end of validity frames as determined by fireball visibility in the frame for 105 g perturbed C4 spheres. The frame rate of camera 1 was 1,000,000 fps. The frame rate of camera 2 was 400,000 fps. The frame rate of camera 3 was 50,000 fps.

	$f = 0$		$f = 785.4$		$f = 1574$	
Camera 1						
Test Number	SoV	EoV	SoV	EoV	SoV	EoV
1	40	128	40	128	60	128
2	35	128	40	128	60	128
3	30	128	22	128	60	128
4	40	128	40	128	40	128
Camera 2						
Test Number	SoV	EoV	SoV	EoV	SoV	EoV
1	10	90	10	100	10	128
2	10	100	10	82	10	95
3	10	98	10	96	10	102
4	20	90	10	95	10	103
Camera 3						
Test Number	SoV	EoV	SoV	EoV	SoV	EoV
1	12	19	14	21	12	20
2	13	23	17	29	12	18
3	15	18	17	29	13	20
4	12	15	27	45	21	44

Table 4.5: The start of validity and end of validity frames as determined by fireball visibility in the frame for 880 g perturbed C4 spheres. The frame rate of camera 1 was 800,000 fps. The frame rate of camera 2 was 200,000 fps. The frame rate of camera 3 was 50,000 fps.

	$f = 0$		$f = 384.6$		$f = 769.2$	
Camera 1						
Test Number	SoV	EoV	SoV	EoV	SoV	EoV
1	27	128	20	128	70	128
2	53	128	36	128	47	128
3	37	128	38	128	58	128
Camera 2						
Test Number	SoV	EoV	SoV	EoV	SoV	EoV
1	10	128	10	128	10	98
2	10	85	10	128	10	90
3	10	111	10	104	10	103
Camera 3						
Test Number	SoV	EoV	SoV	EoV	SoV	EoV
1	26	33	30	45	26	33
2	22	26	27	42	23	30
3	21	30	28	34	26	33

Table 4.6: Characteristic lengths and times for each test series

Characteristic	Primers	Gram	1.32 kg PBXN-113	105 g C4	880 g C4
l_c	0.097	0.379	2.91	1.75	3.5
t_c	0.00029	0.0011	0.0083	0.005	0.0101

conducted tests scaled with the Wei-Hargather scaling. The attached shockwave drops out of the strong shock regime $M > 5$ when predicted by the scaling criteria at $t^* = 0.02$, but remains supersonic ($M > 1$) throughout the remainder of the collected data. As the surface instabilities grow, mean surface radius and velocity become less useful measurements, as the spatial variation in the radius becomes larger, as indicated by the increasing standard deviation of the radius measurement. Scaled surface velocity is not presented for contours extracted from camera 3, as the data is sparse. The growth rate of the perturbations on the surface of the fireball is important for the establishment of later time mixing.

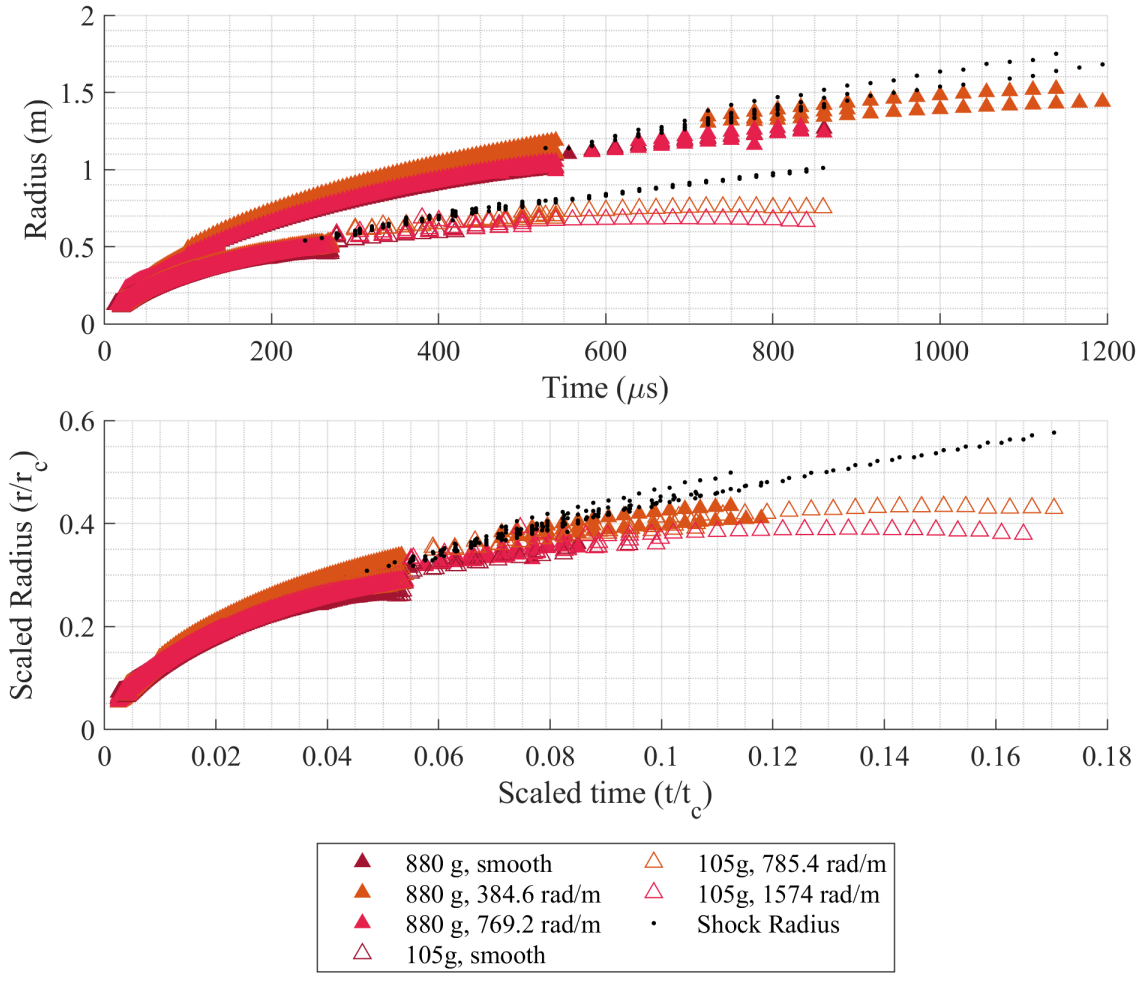

Figure 4.8: (top) The unscaled fireball radii collapse to a single curve when (bottom) scaled with Wei-Hargather scaling for 105 g and 880 g charges. The shock radius is included to highlight the separation between the primary shock and the fireball.

Having established scaling within a single test series, Figure 4.10 shows the

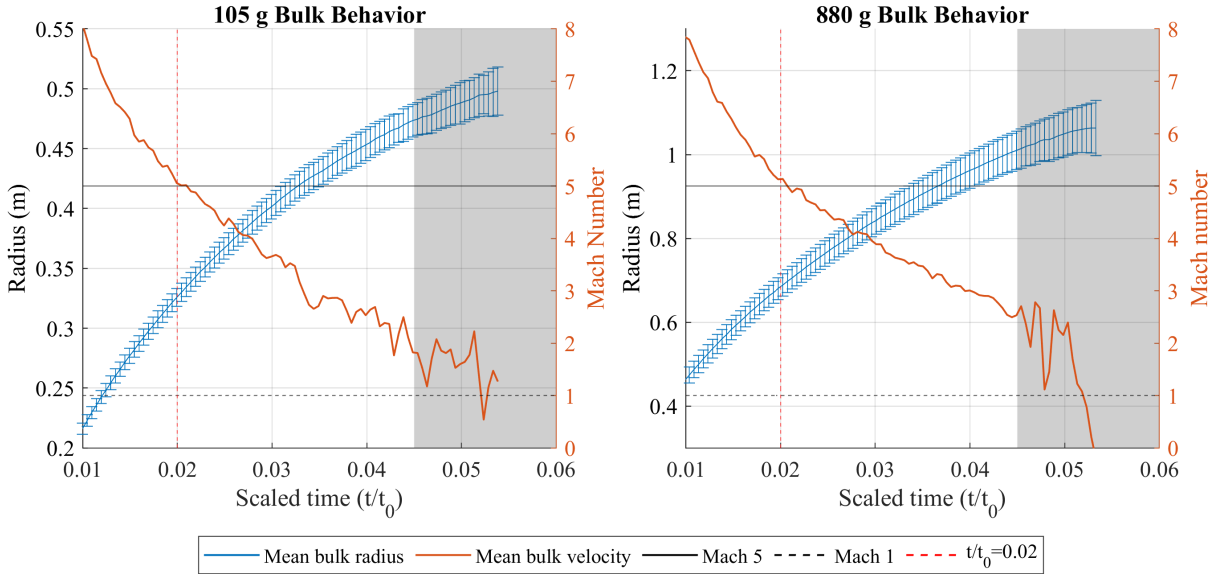

Figure 4.9: For both perturbed explosive charge masses tested, the shock wave separates from the gas cloud well after dropping below the strong shock threshold of $M > 5$, shown with the top horizontal black line. The separation time is shown with the gray shaded section. The error bars on the radius measurement represent a single standard deviation, highlighting the size of the instability driven perturbations on the surface of the gas cloud.

effective scaling of the the other high explosives fireballs. All tests trend towards a plateau in scaled radius after 0.15 scaled time.

The strong shock regime of the blast passes while the shock wave is still attached to the fireball. The change in fluid behavior with the transition out of the strong shock regime makes intuitive sense, as expansion rate slows to nearing the ambient speed of sound and expansion is no longer entirely in the inviscid regime. Shock wave separation began occurring at time scale of approximately 0.04 scaled time in the Wei-Hargather scaling, as determined by the context camera. Due to the texture of the fireball, shock separation does not occur at a single time, but rather over a span of times as the shock clears the peaks and valleys of the fireball. The shock separation was discussed in Section 2.4.4 and Figure 2.18. Shock separation is complete at 0.065 scaled time, at which point the shock wave is no longer directly interacting with the fireball. Separation is complete outside the data collection window for the primary diagnostic cameras, so only it's very early impact on the fractal dimension can be accessed.

4.3 Uncertainty considerations

There are two primary sources of uncertainty when working with digital high speed images, the precise spatial location of an object in frame, and the exact time each frame captured. For camera sensors with low sensor resolution, the spatial uncertainty is dominant over the temporal uncertainty. A digital image has a smallest measurement increment of one pixel. The uncertainty σ in where exactly an object is within a pixel is ± 0.5 pixels in all directions, meaning $\sigma_x = \sigma_y = \sigma_{px} = 0.5$. When measuring a radius there are three principal sources of uncertainty: the uncertainty in the contour location, the uncertainty in the charge center location, and the uncertainty in the calibration between real world units and pixels, which is again a function of pixel location uncertainty. The distance d between two points (x_1, y_1) and (x_2, y_2) on an image is

$$d = \sqrt{(x_1 - x_2)^2 + (y_1 - y_2)^2} \tag{4.1}$$

The uncertainty σ_f of a function $f(x_1, x_2, \cdots, x_n)$ with uncorrelated uncertainties $\sigma_1, \sigma_2, \cdots, \sigma_n$ is [113]

$$\sigma_f^2 = \sigma_1^2 \left(\frac{\partial f}{\partial x_1}\right)^2 + \sigma_2^2 \left(\frac{\partial f}{\partial x_2}\right)^2 + \cdots + \sigma_n^2 \left(\frac{\partial f}{\partial x_n}\right)^2 \tag{4.2}$$

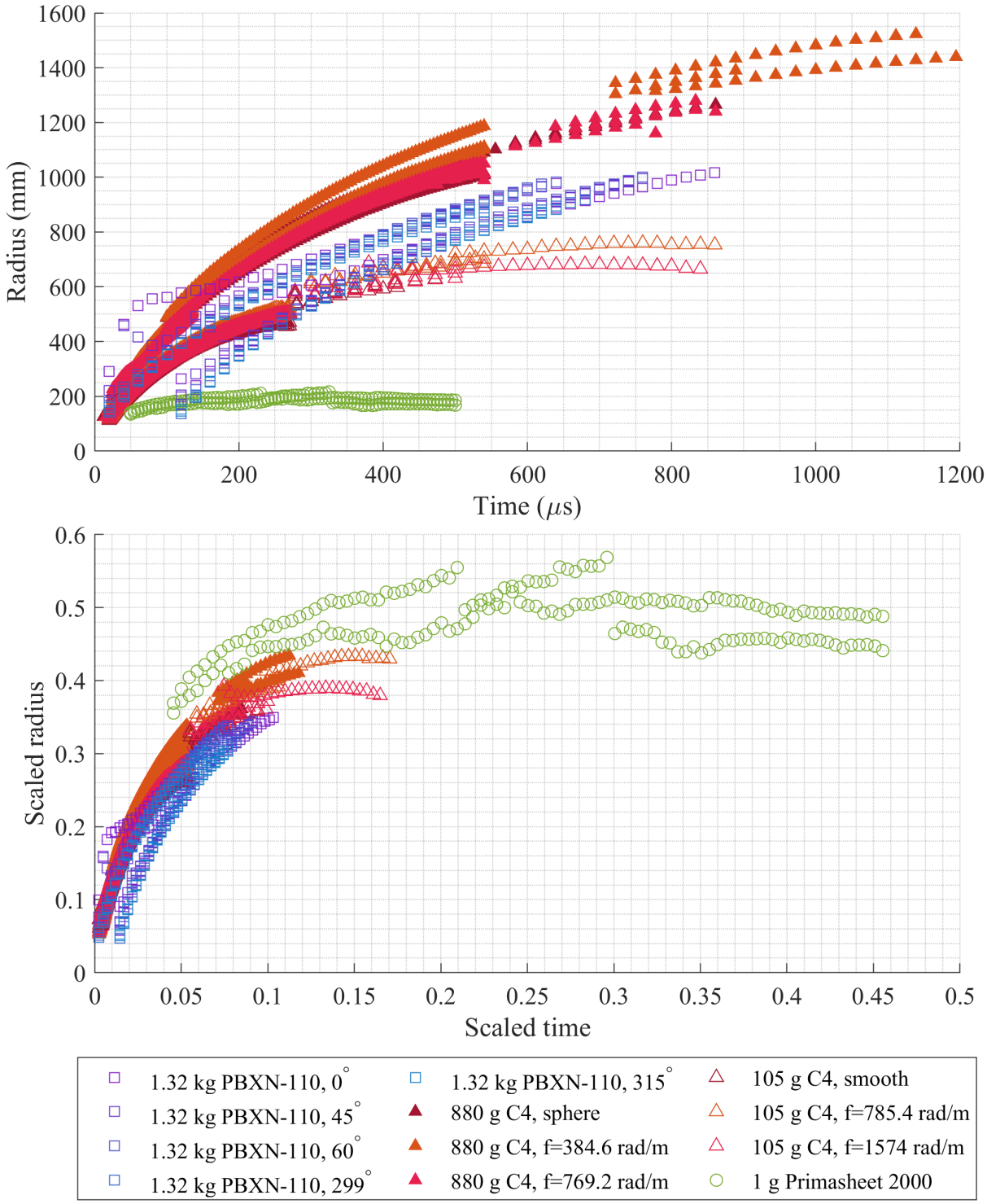

Figure 4.10: The (top) unscaled fireball radii of all tests (bottom) collapse to a single curve when scaled with Wei-Hargather scaling.

Assuming uncorrelated errors between x and y, the uncertainty of a distance between two points in pixels is then

$$\sigma_d = \sqrt{\sigma_{x_1}^2 \left(\frac{\partial d}{\partial x_1}\right)^2 + \sigma_{x_2}^2 \left(\frac{\partial d}{\partial x_2}\right)^2 + \sigma_{y_1}^2 \left(\frac{\partial d}{\partial y_1}\right)^2 + \sigma_{y_2}^2 \left(\frac{\partial d}{\partial y_2}\right)^2} \tag{4.3}$$

$$= \sqrt{2\sigma_x^2 \left(\frac{\partial d}{\partial x}\right)^2 + 2\sigma_y^2 \left(\frac{\partial d}{\partial y}\right)^2} \tag{4.4}$$

$$= \sqrt{\frac{2\sigma_x^2 (x_1 - x_2)^2}{(x_1 - x_2)^2 + (y_1 - y_2)^2} + \frac{2\sigma_y^2 (y_1 - y_2)^2}{(x_1 - x_2)^2 + (y_1 - y_2)^2}} \tag{4.5}$$

$$= \sqrt{2\sigma_{px}^2} \tag{4.6}$$

$$= \sqrt{2}\sigma_{px} \tag{4.7}$$

The uncertainty of the calibration value β is a function of the true size of the calibration object l and the size of that object in the image d.

$$\beta = \frac{l}{d} \tag{4.8}$$

For low resolution images such as from high speed cameras, the uncertainty in the true size of the calibration object is assumed to be significantly smaller than the uncertainty in the pixel distance ($\sigma_l \ll \sigma_d$). Therefore, the uncertainty in β is

$$\sigma_\beta = \sqrt{\sigma_d^2 \left(-\frac{l}{d^2}\right)^2} \tag{4.9}$$

$$= \frac{\sigma_d l}{d^2} \tag{4.10}$$

$$= \frac{\sqrt{2}\sigma_{px} l}{d^2} \tag{4.11}$$

The radius in real units is calculated by

$$r = \beta d \tag{4.12}$$

Again assuming uncorrelated errors between σ_d and σ_β, the uncertainty in any given radius measurement is

$$\sigma_r = = \sqrt{\sigma_\beta^2 \left(\frac{\partial r}{\partial \beta}\right)^2 + \sigma_d^2 \left(\frac{\partial r}{\partial d}\right)^2} \tag{4.13}$$

$$= \sqrt{\sigma_\beta^2 d^2 + \sigma_d^2 \beta^2} \tag{4.14}$$

$$= \sqrt{\sigma_\beta^2 d^2 + 2\sigma_{px}^2 \beta^2} \tag{4.15}$$

The calibration parameter β and its uncertainty σ_β are constant, but the fireball radius in pixels d varies. Therefore uncertainty is maximized where the fireball radius is largest when measured in pixels. The uncertainty in the calibration constant β is very small, so the value of β dominates Equation 4.15. The lower bound for the uncertainty of a radius measurement is for $d = 0$, where

$$\sigma_r|_{d=0} = \sqrt{2}\sigma_{px}\beta = 0.707\beta \tag{4.16}$$

The mean radius $\bar{r}$ is computed by

$$\bar{r} = \frac{\sum_{i=1}^{i} r_i}{n} \tag{4.17}$$

The base uncertainty for the mean radius is therefore;

$$\sigma_{\bar{r}} = \sqrt{\sum_{i=1}^{n} \sigma_{r_i}^2 \left(\frac{\partial \bar{r}}{\partial r_i}\right)^2} \tag{4.18}$$

$$= \sqrt{\sigma_{r_1}^2 \left(\frac{\partial \bar{r}}{\partial r_1}\right)^2 + \sigma_{r_2}^2 \left(\frac{\partial \bar{r}}{\partial r_2}\right)^2 + \cdots + \sigma_{r_n}^2 \left(\frac{\partial \bar{r}}{\partial r_n}\right)^2} \tag{4.19}$$

$$= \sqrt{\frac{\sigma_{r_1}^2}{n^2} + \frac{\sigma_{r_2}^2}{n^2} + \cdots + \frac{\sigma_{r_n}^2}{n^2}} \tag{4.20}$$

$$= \sqrt{\frac{\sum_{i=1}^{n} \sigma_{r_i}^2}{n^2}} \tag{4.21}$$

The number of points square term drives the measurement uncertainty in the average radius down. A given radius measurement may have an uncertainty on the order of 6.4 mm over 1230 mm, but the uncertainty of the mean radius is on the order of 0.1 mm over the same distance.

Another consideration for uncertainty is the exposure or shutter time of the camera. For a camera exposure of t_{sh}, an object traveling at a velocity v will cover a number of maximum number of pixels Δx that is a function of the calibration value β.

$$\Delta x = \frac{v t_{sh}}{\beta} \tag{4.22}$$

To introduce a more significant uncertainty than the dominant pixel uncertainty, an object would have to be moving faster than

$$v = \frac{\sigma_{px}\beta}{t_{sh}} \tag{4.23}$$

Similarly, jitter in the exposure start time is extremely small for all cameras, and is neglected in all velocity calculations. Measurement uncertainty values for all test series are summarized in Table 4.7, along with the cut-off velocity for camera exposure based location uncertainty to be a factor. The cut-off velocity is large relative to the velocity of the fireball surface for all tests, and is neglected.

Table 4.7: Systematic uncertainties associated with measuring distance on digital images for all test series. Values are representative values for series with multiple tests. The maximum individual radius uncertainty is presented to provided an upper bound.

	Primer	**Gram**	**Perturbed C4 (105 g)**		
			Cam 1	**Cam 2**	**Cam 3**
t_{sh} (ns)	10	10	200	200	1100
β (mm/px)	0.623 ± 0.02	3.5 ± 0.06	4.01 ± 0.01	5.95 ± 0.02	4.02 ± 0.01
σ_{px} (px)	0.5	0.5	0.5	0.5	0.5
Max σ_r (mm)	129 ± 1.64	195 ± 3.7	362 ± 2.8	530 ± 4.5	628 ± 3.2
v (km/s)	31.2	175	10.1	14.8	1.9

Perturbed C4 (880 g)			
	Cam 1	**Cam 2**	**Cam 3**
t_{sh} (ns)	200	200	1100
β (mm/px)	3.8 ± 0.01	11.9 ± 0.1	8.3 ± 0.05
σ_{px} (px)	0.5	0.5	0.5
Max σ_r (mm)	515 ± 3.0	1370 ± 14.7	1490 ± 10.7
v (km/s)	9.5	29.75	3.8

PBXN-113					
	0°	45°	60°	299°	315°
t_{sh} (ns)	437	437	1000	294	294
β (mm/px)	5.51 ± 0.02	5.99 ± 0.03	7.76 ± 0.04	7.42 ± 0.04	5.16 ± 0.02
σ_{px} (px)	0.5	0.5	0.5	0.5	0.5
Max σ_r (mm)	1230 ± 6.4	1285 ± 7.3	1001 ± 8.2	930 ± 7.2	882 ± 5.0
v (km/s)	6.31	6.85	3.88	12.6	8.78

CHAPTER 5

EVALUATION OF THE MIXING REGION GROWTH FOR EXPLOSIVE EVENTS USING ANALYTICAL MODELS

The mixing region results from primer driven confined gas expansion and perturbed C4 spheres are reported. Mixing widths are compared to results from analytical equations. Fitting parameters are compared to literature values.

5.1 Mixing region width from varied explosives

The mixing region was determined for two principal test series, the confined explosively driven gas clouds of the shotgun primers and direct detonation fireballs of the smooth and perturbed C4 spheres. It is reported as a function of time and scaled time.

5.1.1 Mixing region growth for variably confined gas clouds[1]

Manual extraction was performed on the confined explosively driven gas clouds generated by shotgun primers to validate the mixing region width extracted by the automated extraction algorithms. Figure 5.1 shows the extracted mixing region width as a function of time for all primer tests. The mixing region as extracted by morphological processing was compared to the manually extracted mixing region. Figure 5.2 shows a representative example of manual and morphological results for both radius and mixing region width. The two methods show good agreement, and only the morphological method was used in further analysis.

[1] A large portion of this section is reprinted from Christian Peterson, Veronica Espinoza, and Michael Hargather. Experimental evolution of explosively driven gas clouds in varying confinment, Experiments in Fluids, 63(12):1-11, 2022, Reproduced with permission from Springer Nature.

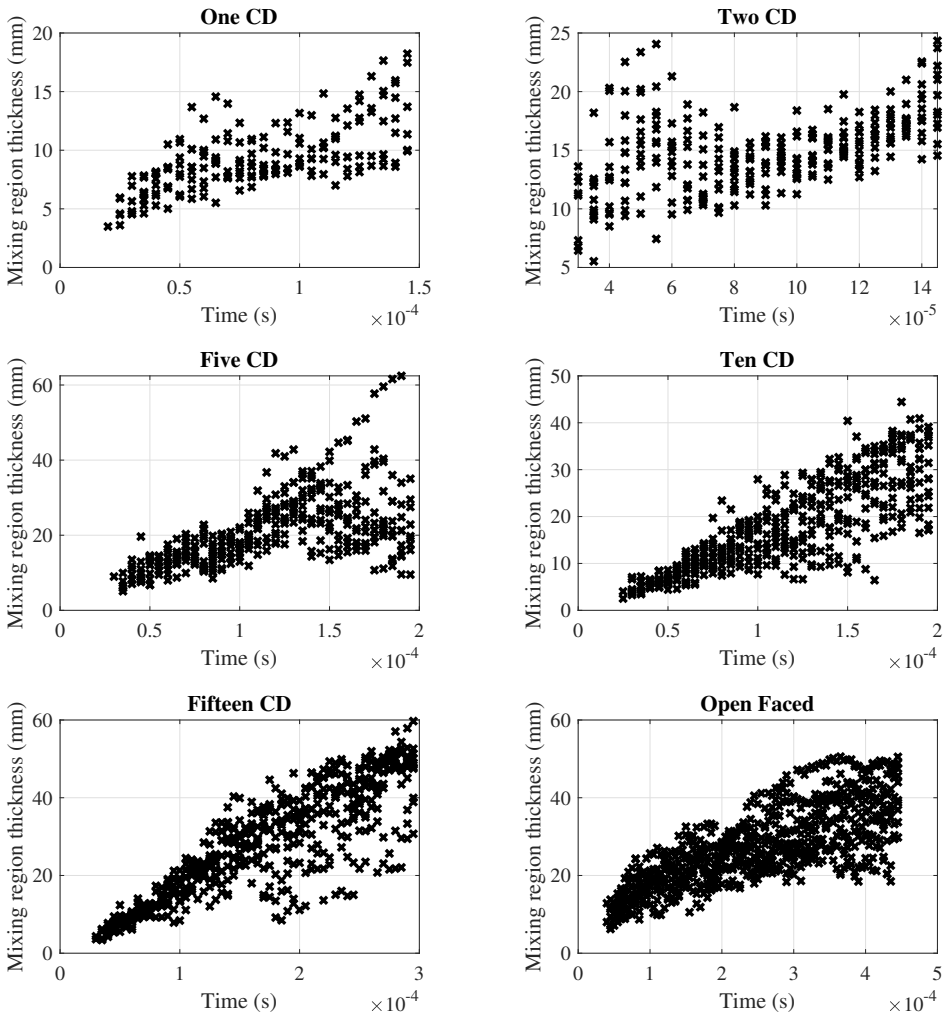

Figure 5.1: The raw mixing region width data as extracted from the shotgun primer image sets. The data are shown for 10 tests under each confinement condition from 1 CD to the open faced geometry.

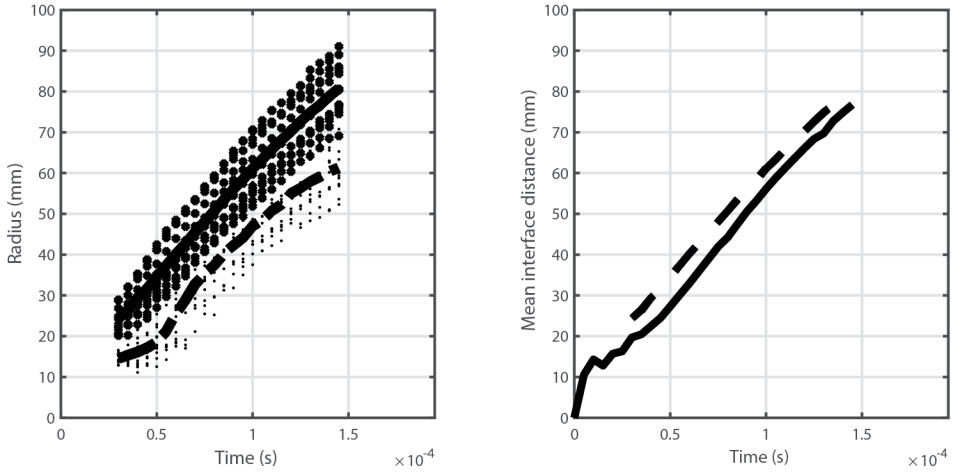

Figure 5.2: (Left) Multiple tests at each spacing are reduced to a single mean value for both the leading and trailing edge of the gas cloud mixing region. The crosses and solid line are the peak leading edge data points, and the dots (·) and dashed line are the "valley" trailing edge points. The data here is the two charge diameter (2CD) separation case. (right) Comparison of manual tracking (dashed line) to the automated morphological tracking (solid line) method.

Primer specific uncertainty considerations The uncertainty of the determined radius for the manual tracking methods is variant across the image space. The uncertainty is 1.2 mm over a 122 mm radius, or just under 1% uncertainty. The temporal accuracy is set by the pulsed laser illumination. The 10 ns laser pulse is driven by a a camera output with 10 ns of jitter, or 0.2% of the nominal interframe time. The systematic uncertainty of the measurement remains under 1 pixel deviation at the furthest corners of the measurement domain. There are variations in the pneumatic initiation of the primer, which causes uncertainty in the exact time of initiation. By using the high speed images, the uncertainty was determined to be a single frame of jitter added to the interframe time, or 5.7 μs

5.1.2 Mixing width of perturbed spheres

The mixing region width was determined using the methodology from Section 2.4.4 for all C4 perturbed sphere tests, and is reported as an average by perturbation and charge mass. Figure 5.3 shows the mixing region widths and uncertainties for cameras 2 and 3 for the 105 g charges sorted by perturbation. Figure 5.4 shows the mixing region widths and uncertainties for cameras 2 and 3 for the 880 g charges sorted by perturbation. For clarity, the uncertainty bars will be omitted unless relevant to the discussion.

The baseline case for fireball surface evolution is the detonation of a smooth sphere. Figure 5.5 specifically highlights the behavior of the mean of the 105 g smooth charges. The largest difference in measured mixing width was approximately 15 mm near the end of the measurement. While this difference was larger than the measurement uncertainty, the mean behavior well represents the behavior of the mixing width for the 105 g smooth charges. The trend of the mean was consistent with the raw data.

The smooth 105 g mean mixing width was used as a baseline measurement for comparing the relative evolution of the perturbed 105 g charges. The evolution of the perturbed 105 g mixing widths were compared to the evolution of the smooth 105 g charge mixing width by subtracting the mixing width of the perturbed cases from the mean mixing width of the smooth cases, resulting in a difference in mixing region growth from the smooth baseline. Figure 5.6 shows the mixing width of the perturbed tests minus the mixing width of the mean smooth test. The $f = 785.4$ rad/m tests remained within the measurement uncertainty of the smooth mean. Tests 3 and 4 trend upward enough to be outside the uncertainty, but the bulk trend of the data does not vary significantly from the baseline. The $f = 1574$ rad/m mixing width growth trends slightly lower than the baseline. This trend is within the uncertainty until 0.183 ms, where 3 of the 4 tests begin trending downward toward a maximum of 13 mm below the baseline, where the local uncertainty is 5.1 mm. Overall, there is limited impact on the mixing region width for the perturbed cases relative to the smooth case.

The evolution of the smooth 880 g charges was analyzed for consistency as a baseline. Figure 5.7 shows the three 880 g smooth tests and their deviation from the mean. While test 3 had a consistently lower mixing width, it was within the uncertainty of the other two tests, and followed the same growth trend. The mean mixing width of the 880 g smooth tests was used as a baseline to assess the mixing region growth trends for the perturbed 880 g charges.

The evolution of the perturbed 880 g charges mixing widths were compared to the baseline case. Figure 5.8 shows the evolution of each perturbed test minus the baseline mean smooth test. Both perturbations exhibited measurably lower mixing widths than the smooth case. Test 1 of the $f = 384.6$ rad/m case in particular was lower than the baseline, though not outside of uncertainty from the other 2 tests at that perturbation. Tests 1 and 3 had similar mixing region growth rates to the baseline, demonstrated by maintaining a consistent offset from the mean. Test 2 differs in growth rate, growing slower than the baseline measurement. The $f = 769.2$ rad/m case was more tightly grouped at around a 20 mm smaller mixing region than the baseline.

Figure 5.9 reports the mixing region width h and the normalized mixing region width h/l_c for all cameras and charge masses. The difference in mixing width between the 880 g charges is within the uncertainty of the measurement. The behavior of the mixing region width shows a divergence larger than uncertainty in behavior between the mixing region growth of the 105 g $f = 785.4$ rad/m charge and remaining charges when normalized against the characteristic length and time, as is highlighted in Figure 5.9. The 880 g charges all show a

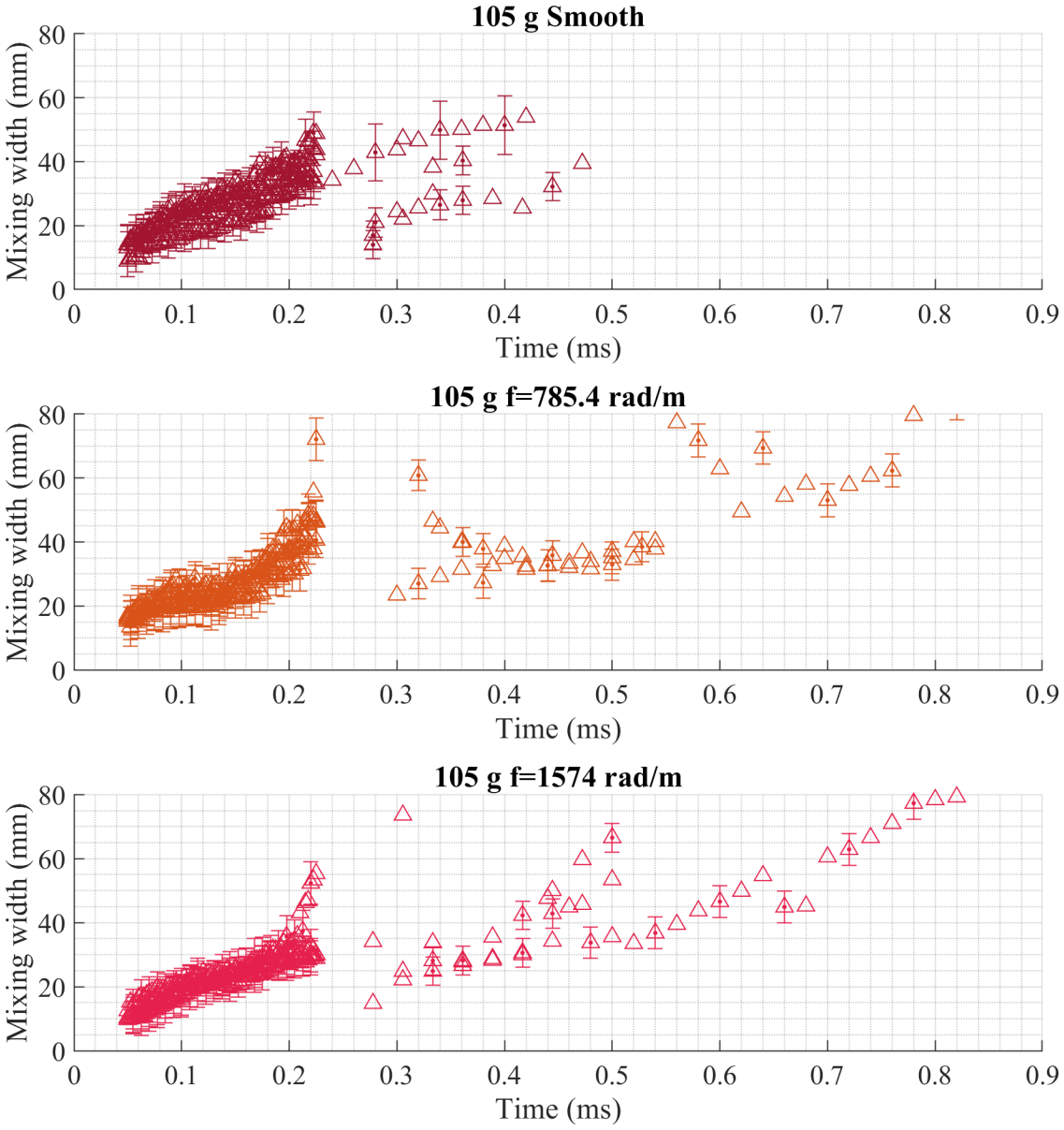

Figure 5.3: The mixing width by perturbation for 105 g spherical C4 charges from cameras 2 and 3. The measurement consistency drops significantly when moving to camera 3.

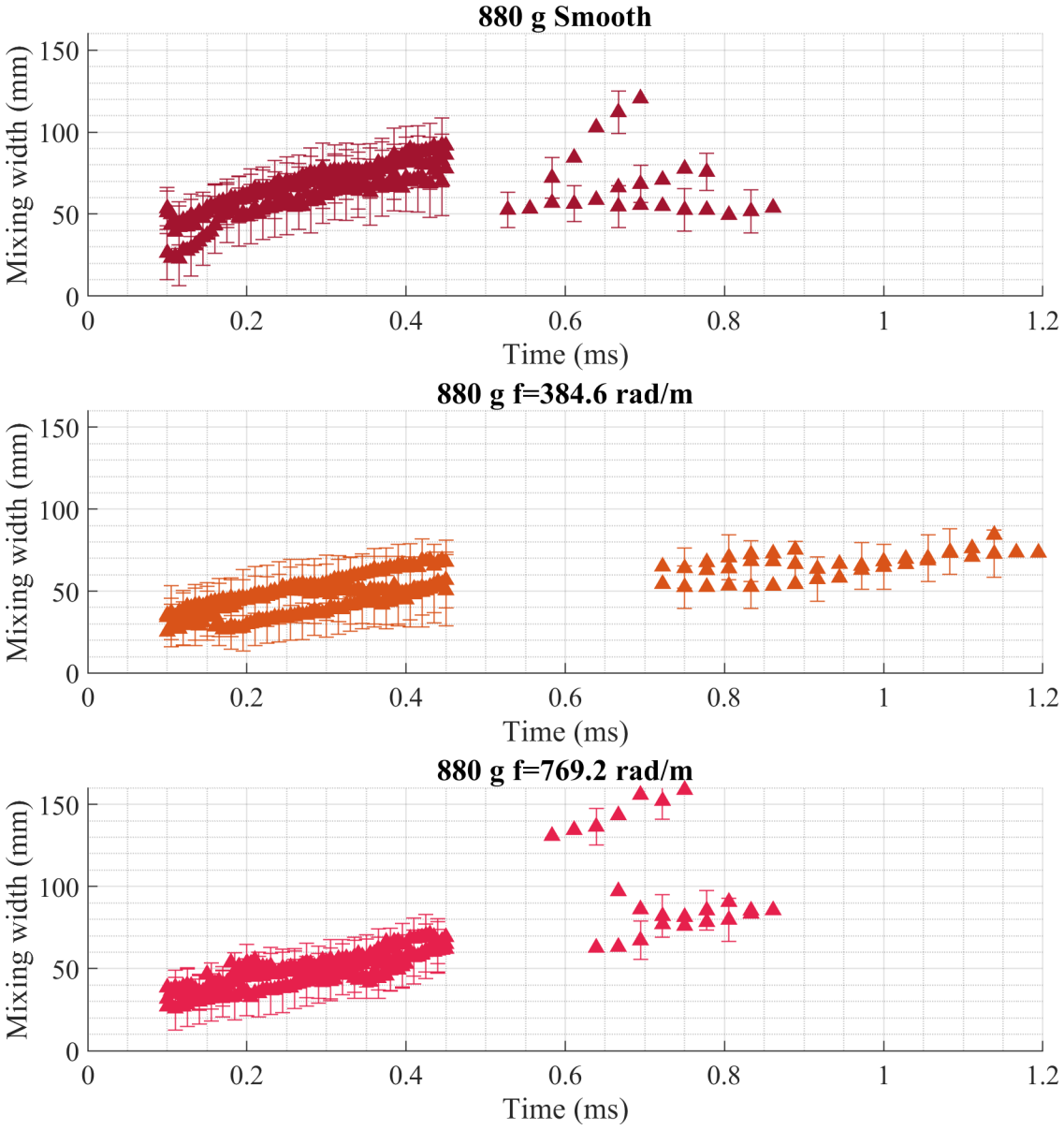

Figure 5.4: The mixing width by perturbation for 880 g spherical C4 charges from cameras 2 and 3. The measurement consistency drops significantly when moving to camera 3.

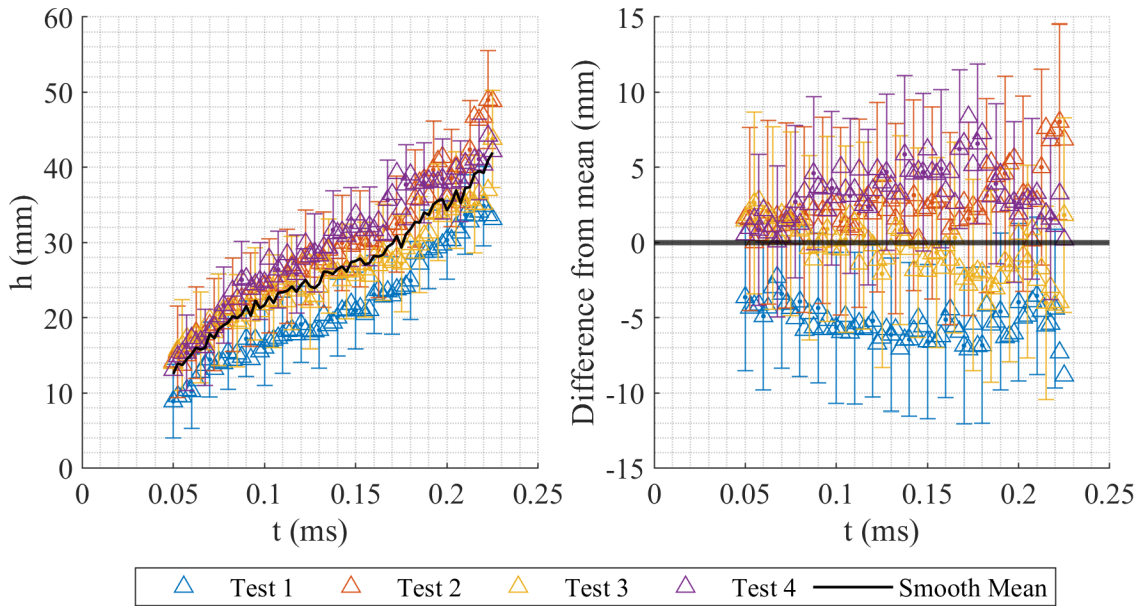

Figure 5.5: The (left) mixing width for individual tests of 105 g smooth charges, with the mean value plotted in black. The (right) difference of each test from the mean shows dispersion is slightly higher than the uncertainty of the measurement.

fairly linear growth rate throughout the diagnostic window. The initial growth rate of the 880 g charges mixing region was slightly lower (85%) than the initial growth rate of the smaller 105 g charges mixing region.

The perturbed 105 g charges initially follow the same approximately linear behavior as the 880 g configurations, but diverges in behavior at approximately 0.033 scaled time, remaining within the linear growth regime while increasing the approximate growth rate by a further factor of approximately 2. The change in growth rate only appears in the the $f = 785.4$ rad/m 105 g perturbed sphere case, and the smooth and the $f = 1574$ rad/m 105 g tests continues on a linear growth trend. As described in Table 4.4, the last data points are nearing the EoV for camera 2. The contextual data from camera 3 at a later time suggests that the apparent spike in seen in camera 2 does not translate to increased mixing region width at later times. In fact, the camera 3 data, though much more dispersed, suggests that the growth of the mixing region briefly plateaus as the initial shock separates from the fireball, before continuing a near linear increase.

The mixing region growth rate with respect to time $\frac{\mathrm{d}h}{\mathrm{d}t}$ was estimated for the camera 2 data. To estimate the growth rate, the following fourth order centered difference scheme was used,

$$\frac{\mathrm{d}h_i}{\mathrm{d}t} = \frac{h_{i-2} - 8h_{i-1} + 8h_{i+1} - h_{i+2}}{12\Delta t} \tag{5.1}$$

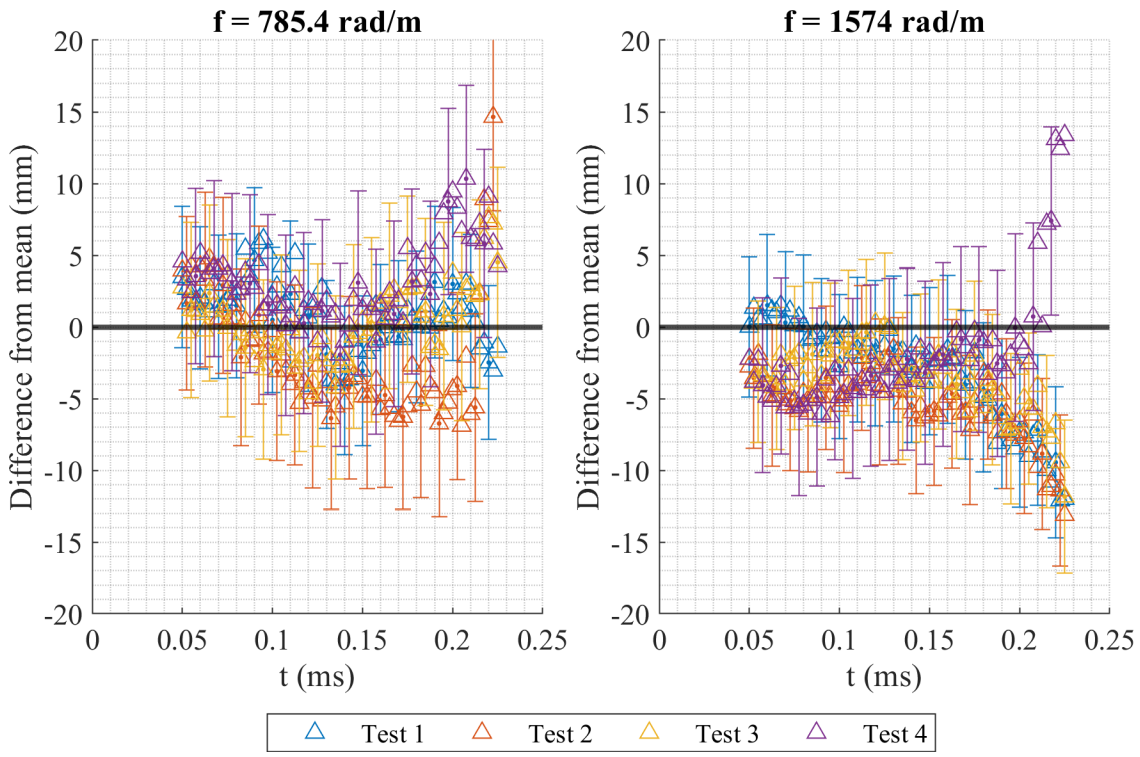

Figure 5.6: The (left) 105 g $f = 785.4$ rad/m and (right) 105 g $f = 1574$ rad/m mixing width for individual tests minus the mean mixing width of the smooth charges.

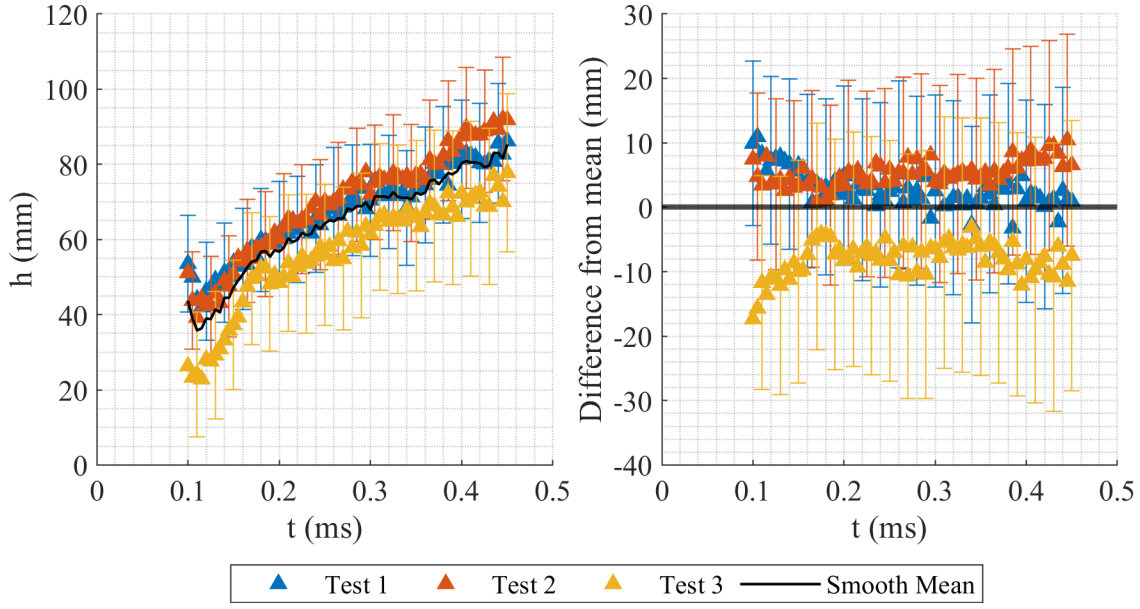

Figure 5.7: The (left) mixing width for individual tests of 880 g smooth charges, with the mean value plotted in black.

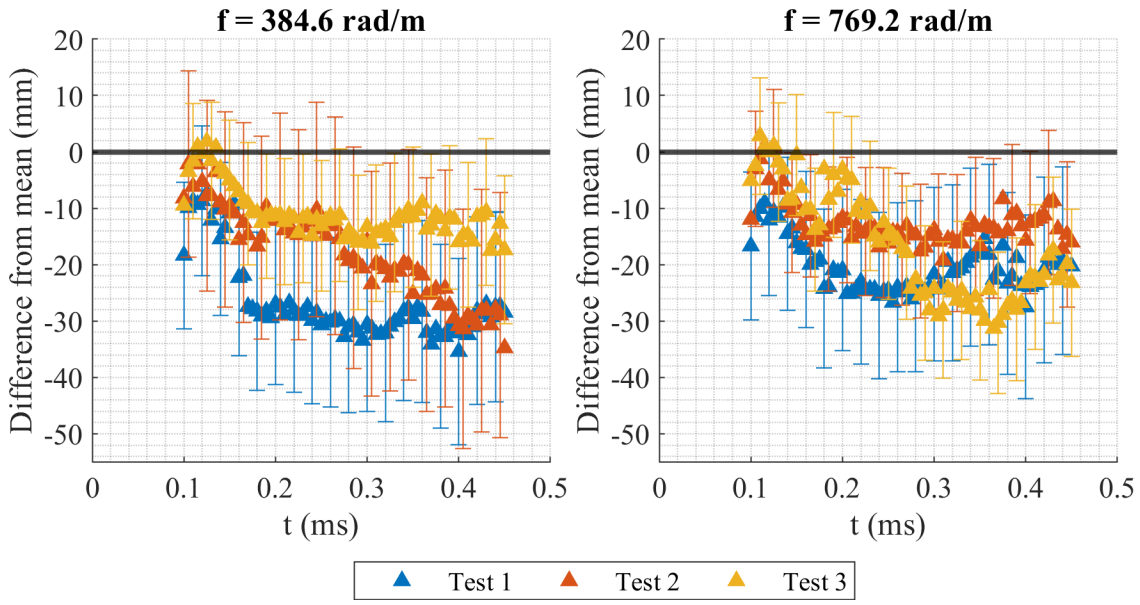

Figure 5.8: The (left) 880 g $f = 384.6$ rad/m and (right) 880 g $f = 769.2$ rad/m mixing width for individual tests minus the mean mixing width of the smooth charges.

where h_i is the mixing width at the ith time step, and Δt is the time between steps. Direct numerical differentiation of the data was very sensitive to small variations in the mixing region width, resulting in anomalous results. To better characterize the general growth velocity trends at the expense of precision, a moving mean over 10 time points was calculated for the growth rate. Figures 5.10 and 5.11 shows the impact of the moving mean on the 105 g and 880 g smooth charges. The moving mean produced a growth rate that was in line with the bulk trends seen in the width data. The smooth charge configurations for both masses were used as baseline growth rates.

Figure 5.12 shows the baseline growth rate as a function of time. Both 105 g and 880 g charges show stable, nearly linear, growth rates over this time period. The slopes, reported in Table 5.1, are minimal indicating that the growth of these perturbations is well within a linear regime of growth. There is not any apparent separation in growth rate between the various charges with different initial perturbations. Even with the moving mean the uncertainty in the velocity measurement is double the value of the measurement. The uncertainty presented is very conservative, and the primary value of the growth rate calculation is the establishment of overall trends in the mixing width. The growth rate of the 105 g charges was influenced by the change in linear behavior highlighted in Figure 5.9, and has a small but consistent upward slope. These growth rates are slow relative to the velocity of the expanding fireball. In the context of bulk cloud velocity, the mixing region growth rates are very similar between charge masses. The similarity is evident in Figure 5.12, where scaling the growth rate by the characteristic

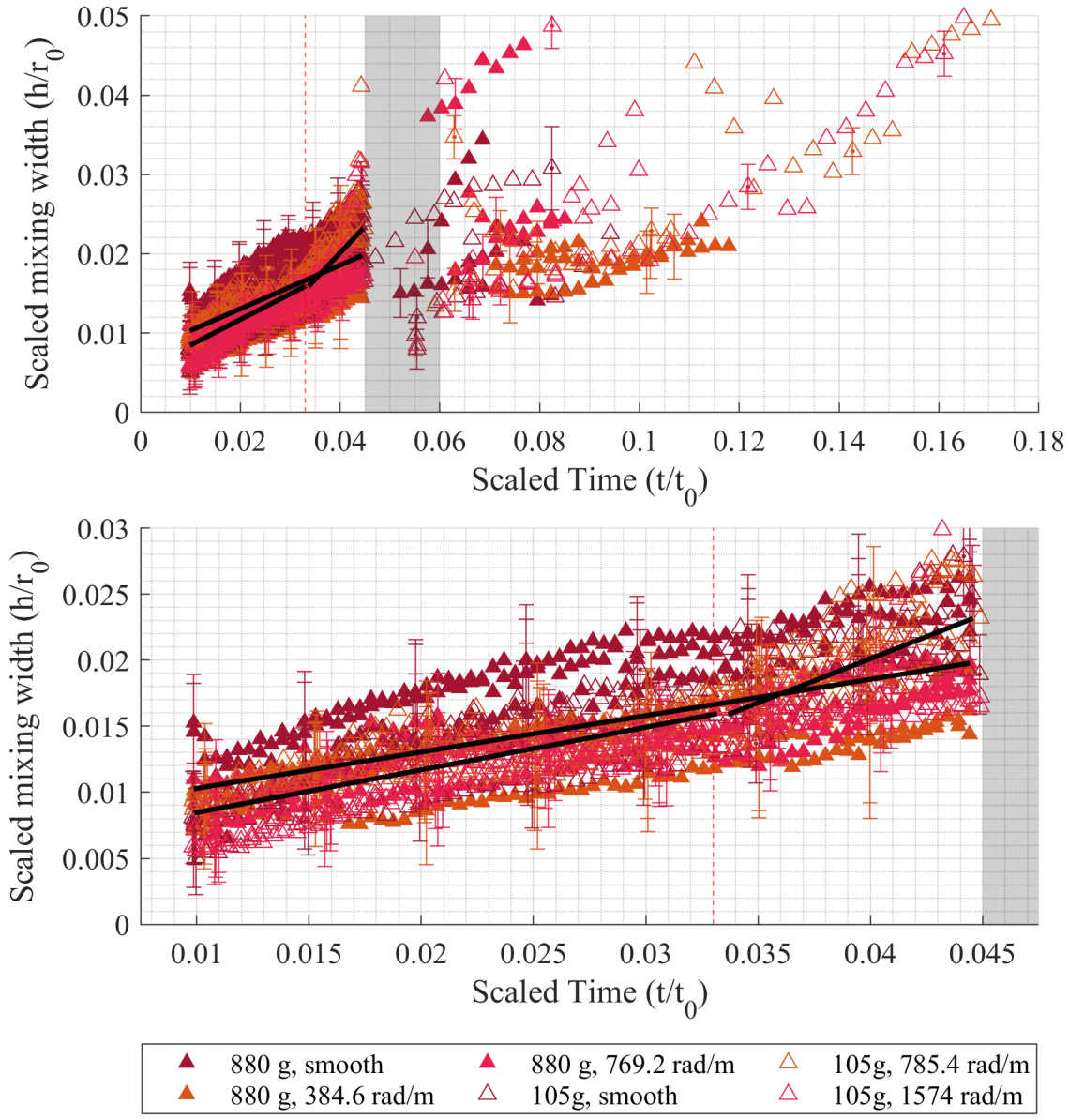

Figure 5.9: (top) The mean mixing region width averaged across charge configuration. The vertical dashed red line demarcates the approximate separation point between the behavior of the 105 g $f = 384.6$ rad/m charge and remaining charges, and the gray shaded region represents the onset of shock separation. (bottom) Plotting only the data from camera 2 highlights the that while the change in mixing region growth rate is large, it is only marginally outside the uncertainty of the measurement.

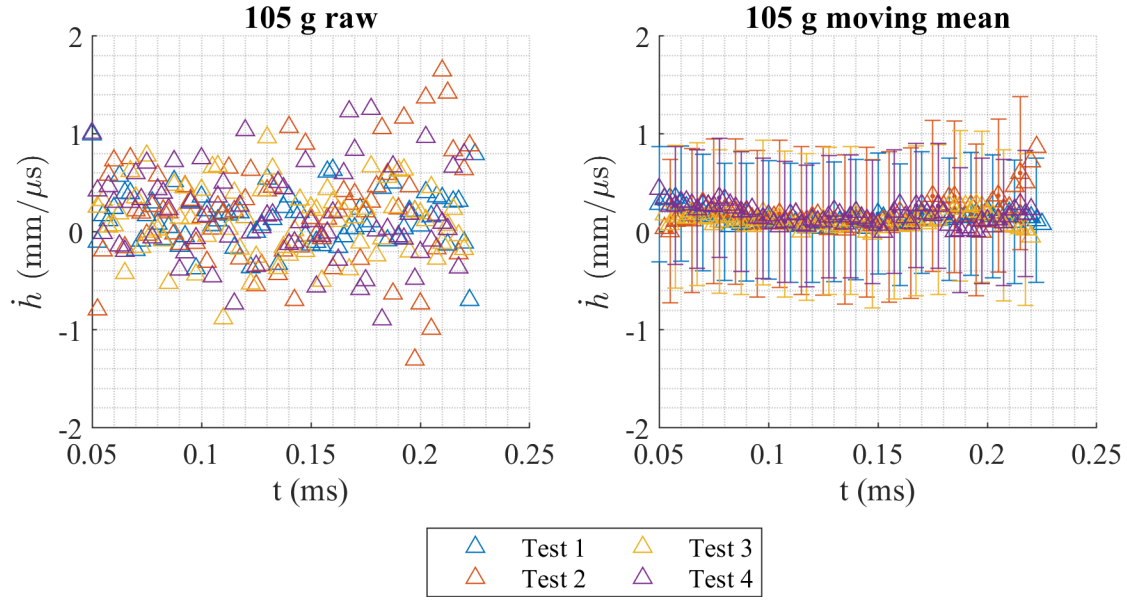

Figure 5.10: The (left) raw mixing growth rate data had large dispersion. When (right) smoothed by a moving mean the growth rates followed the expected trends from inspection of the mixing width data.

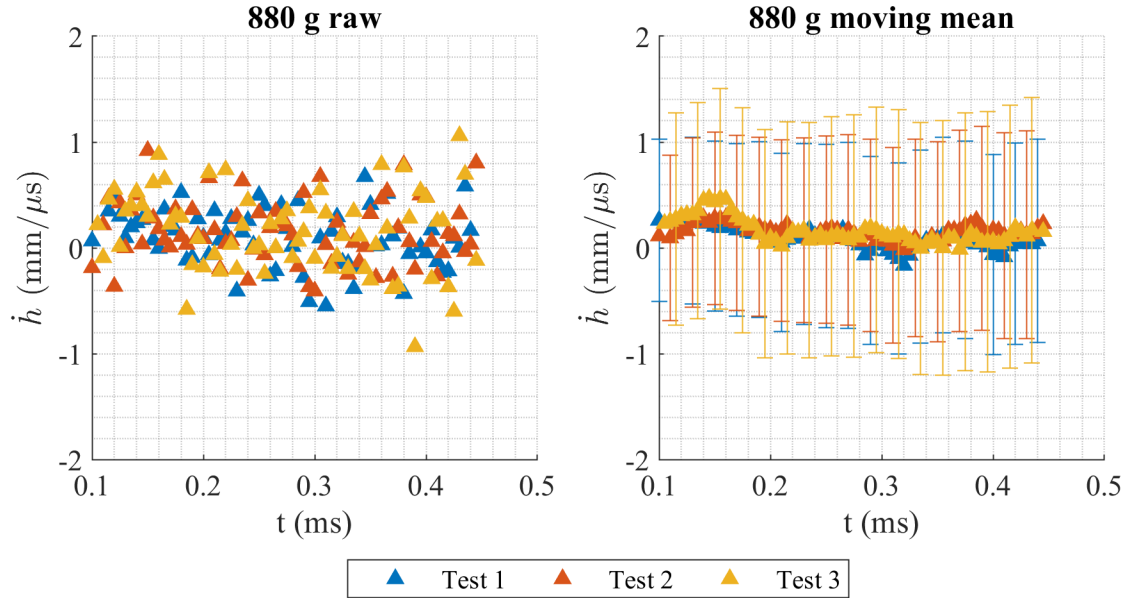

Figure 5.11: The (left) raw mixing growth rate data had large dispersion. When (right) smoothed by a moving mean the growth rates followed the expected trends from inspection of the mixing width data.

velocity C_0 and characteristic time t_0 collapse the data.

Table 5.1: The slope of a linear fit to the mixing region growth rate, or the linearized acceleration of the mixing region width.

	Growth rate acceleration (m^2/s^2)		
	Smooth	$f = 785.4$ $f = 384.6$	$f = 1574$ $f = 769.2$
105 g	0.09	0.50	-0.74
880 g	-0.51	-0.05	-0.30

The initial perturbations were of magnitude 1 mm, which when compared to the initial radius of the spheres is small. The 105 g charges had an initial perturbation to radius ratio of $h_0/R_0 = 0.039$. The 880 g charges had an initial perturbation to radius ratio of $h_0/R_0 = 0.020$. These ratios were considered sufficient to satisfy the $h \ll R_0$ assumption that is a requirement from the Plesset equations [8, 10]. Figure 5.13 shows the evolution of the ratio between the mixing width and fireball radius. As the fireball expanded, the ratio increased slightly, but stabilized at $h(t)/R(t) = 0.065$ for the 105 g charges and $h(t)/R(t) = 0.07$ for the 880 g charges, though the 105 g charges grew to over 0.1 for the smooth and low frequency tests. The ratio between h and R was very stable for the 880 g test, with minimal change after 0.02 scaled time. The 105 g charges were similarly stable until 0.033 scaled time, when the mixing region begins to spike in several tests. The increase in 105 g charge mixing width seen in camera 2 near the end of its validity also increases the ratio to around 0.05. Overall, the consistency of the ratio between the mixing region width and the fireball radius indicates that a scaling effective for the radius of the fireball would also be effective for the mixing region width on the surface of that fireball. The effectiveness of this scaling is supported by Figure 5.9, where the characteristic length and time from Wei-Hargather shock scaling collapse the width of the mixing region to a single trend.

The impact of large sinusoidal perturbations on the evolution of the mixing region in bare C4 charges appears to be minimal. The estimated mixing width was within uncertainty of the baseline for 105 g and 880 g charges. The growth rates of the perturbed and unperturbed charges were consistent, and appear to be largely constant with time. The ratio between fireball radius and mixing region width increases from the initial perturbations, but remained stable for the 880 g charges. The mixing measurements all take place before the secondary shock interacts with the surface, and therefore the primary driver of instability on the surface will be the acceleration of the fireball contact surface with respect to the ambient air.

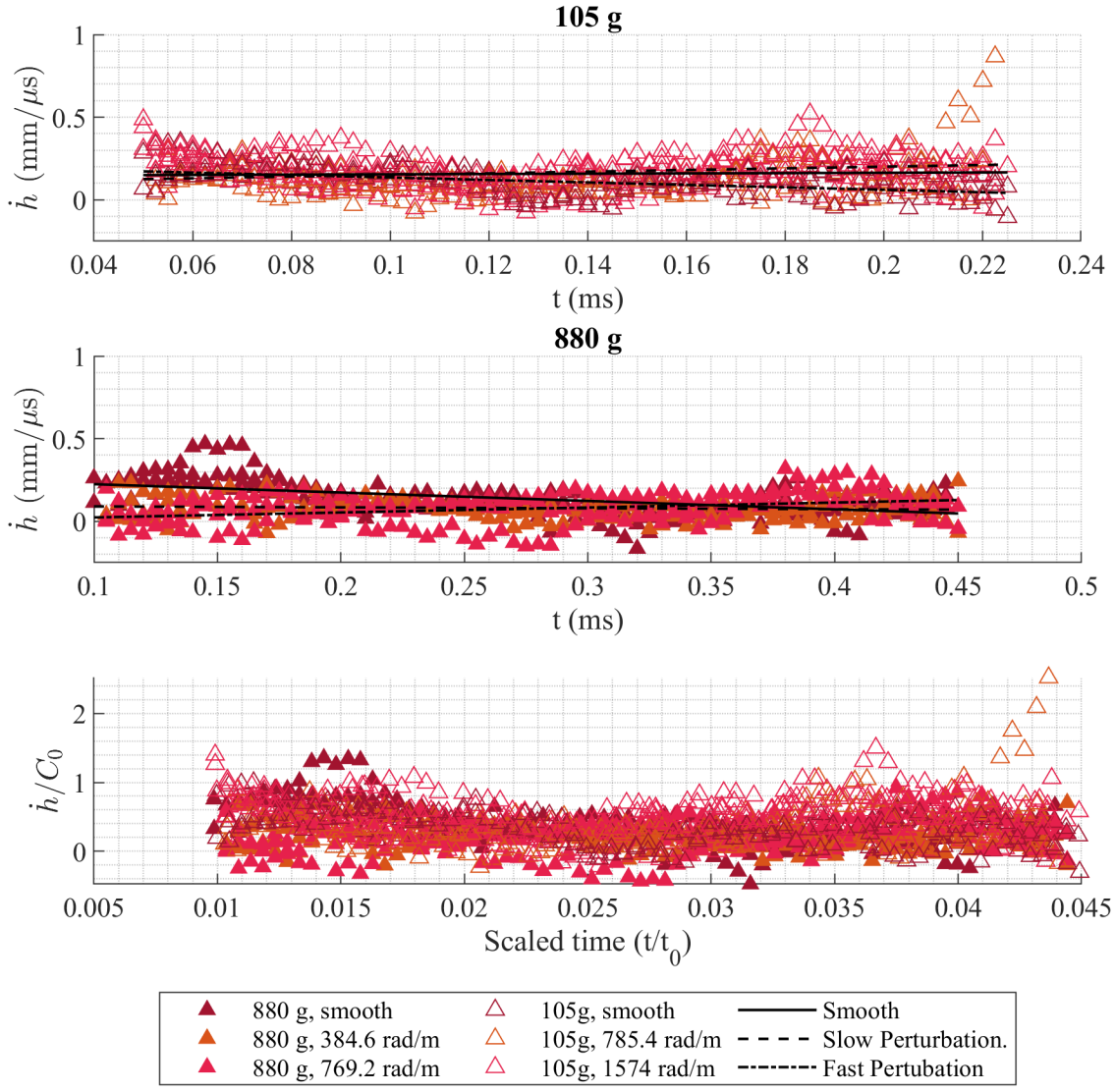

Figure 5.12: The mixing region growth rate for (top) 105 g and (middle) 880 g charges. The slow perturbation refers to the $f = 785.4$ rad/m and $f = 384.6$ rad/m cases for 105 g and 880 g charges respectively. The fast perturbation refers to the $f = 1574$ rad/m and $f = 769.2$ rad/m cases for 105 g and 880 g charges respectively. The scaled growth rate versus scaled time (bottom) confirms that the growth rates are very similar for both masses.

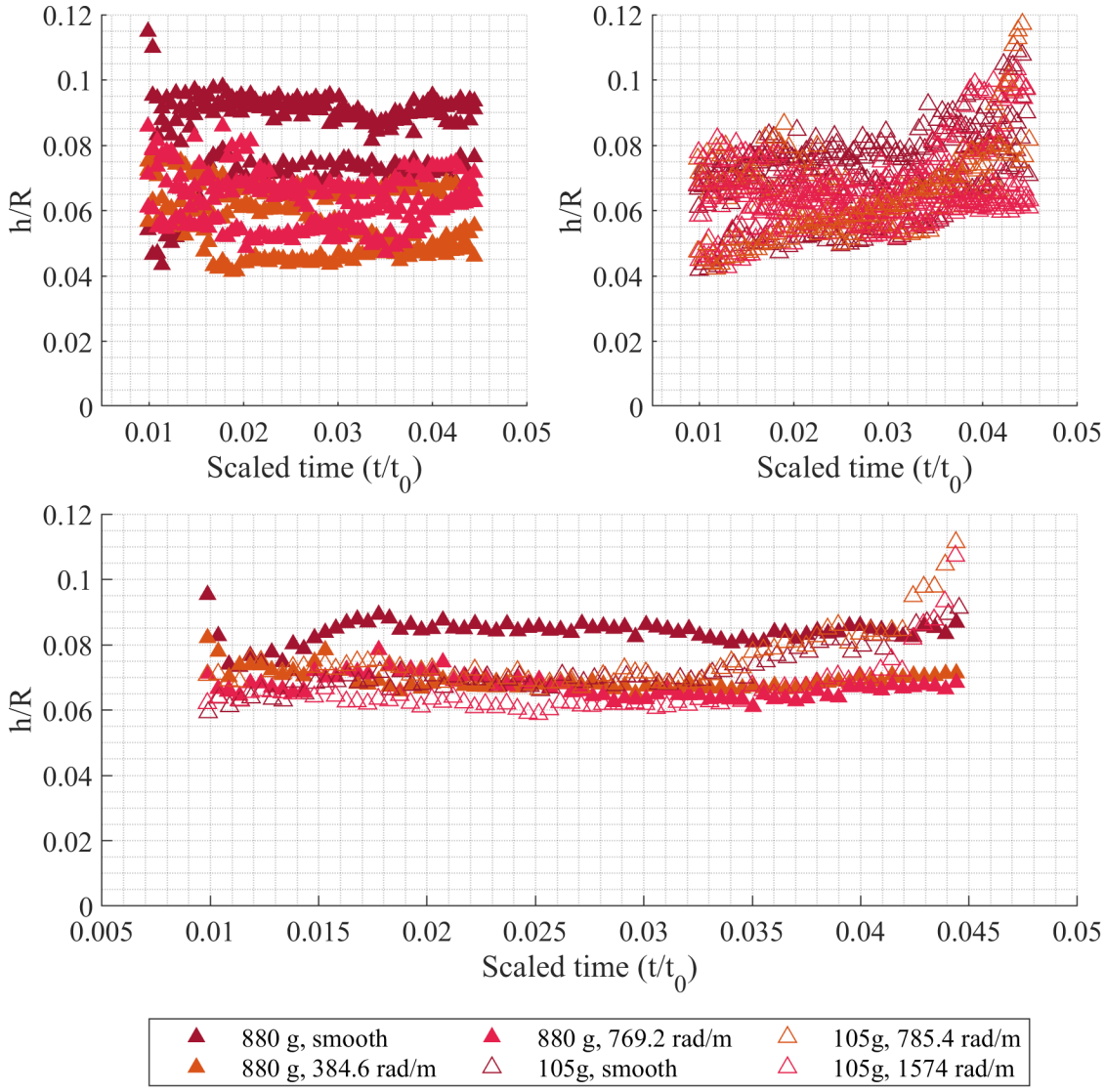

Figure 5.13: The ratio between the mixing region width h and the mean fireball radius R for (top left) the 880 g charges, (top right) the 105 g charges, and (bottom) the mean mixing width of each charge configuration as recorded by camera 2.

5.1.3 Uncertainty in mixing width measurements for perturbed spheres

The uncertainty in the mixing layer thickness is a function of the relative radius difference between the minimum radii in the valley r_{val} and the maximum radii in the peaks r_{peak}. The identification of all mixing regions widths was done when the radii are already converted to physical units. The uncertainty in a given mixing region width measurement in mm is found in Equation 5.2, where $\sigma_{r_{peak}}$ and $\sigma_{r_{val}}$ are calculated using Equation 4.15.

$$\sigma_h = \sqrt{\sigma_{r_{peak}}^2 + \sigma_{r_{val}}^2} \tag{5.2}$$

The relative uncertainty in the mixing region measurement is large compared to the uncertainty in the averaged radius data. As discussed in the baseline radius uncertainty, the calibration constant dominates the values for $\sigma_{r_{peak}}$ and $\sigma_{r_{val}}$. The lower bound for the uncertainty in the estimated mixing region width is β.

The uncertainty of the growth rate measurement is obtained by plugging Equation 5.1 into Equation 4.2. The assumption is made that the uncertainties in the mixing width do not vary significantly between time steps as the dominant component β does not change, so $\sigma_{h_{i-2}} \approx \sigma_{h_{i-1}} \approx \sigma_{h_{i+1}} \approx \sigma_{h_{i+2}} \approx \sigma_h$.

$$\sigma_{\dot{h}} = \frac{\sigma_h}{6\Delta t}\sqrt{\frac{65}{2}} \tag{5.3}$$

As Δt is very small, the uncertainty of the velocity measurement is very large. The moving mean calculation, following Equation 4.18, reduces the magnitude of the uncertainty, but it is still significant compared to the measured values.

5.2 Analysis of analytical models for mixing width

The Mikaelian model for mixing region growth in spherical geometry was compared to the mixing width data from the two experimental setups. The mixing width in variably confined gases was compared to the model to develop the underlying technique. Tests of explosive spheres with known initial perturbations were then compared to a modified and unmodified Mikaelian equation and the results were assessed.

5.2.1 Application of analytical models to mixing in variable confinement[2]

The Mikaelian model, restated in Equation 5.4, requires the use of a tuning parameter c to adjust the fit of the model to growth for varying geometries of

[2]A large portion of this section is reprinted from Christian Peterson, Veronica Espinoza, and Michael Hargather. Experimental evolution of explosively driven gas clouds in varying confinment, Experiments in Fluids, 63(12):1-11, 2022, Reproduced with permission from Springer Nature.

explosive expansion.

$$h(t) = h(0) + R_0^2 \frac{\mathrm{d}h_0}{\mathrm{d}t} \int_0^t \frac{dt}{R^2} + c\mathcal{A} \int_0^t \left(\frac{1}{R^2} \int_0^t R^2 \ddot{R} dt' \right) dt \tag{5.4}$$

This parameter is necessary to achieve good agreement. In [9] it is found that a c value of 0.1 was appropriate for a cylindrical geometry. For the two dimensional approximation 1 CD case, which matches most closely with the cylindrical geometry described commonly in literature, good agreement with the experimental data is found with $c = 0.3$. In the 2 CD case, more deviation can be seen in Figure 5.14, especially in the early time. This is largely attributed to the early time noise in both peak and valley measurements, as the early time numerical derivatives fluctuate. As the experimental conditions varied from the baseline case, the value for best fit of the parameter c increases towards unity. This is surprising, as the variation in confinement increases the geometry moves further from the ideal case described in literature.

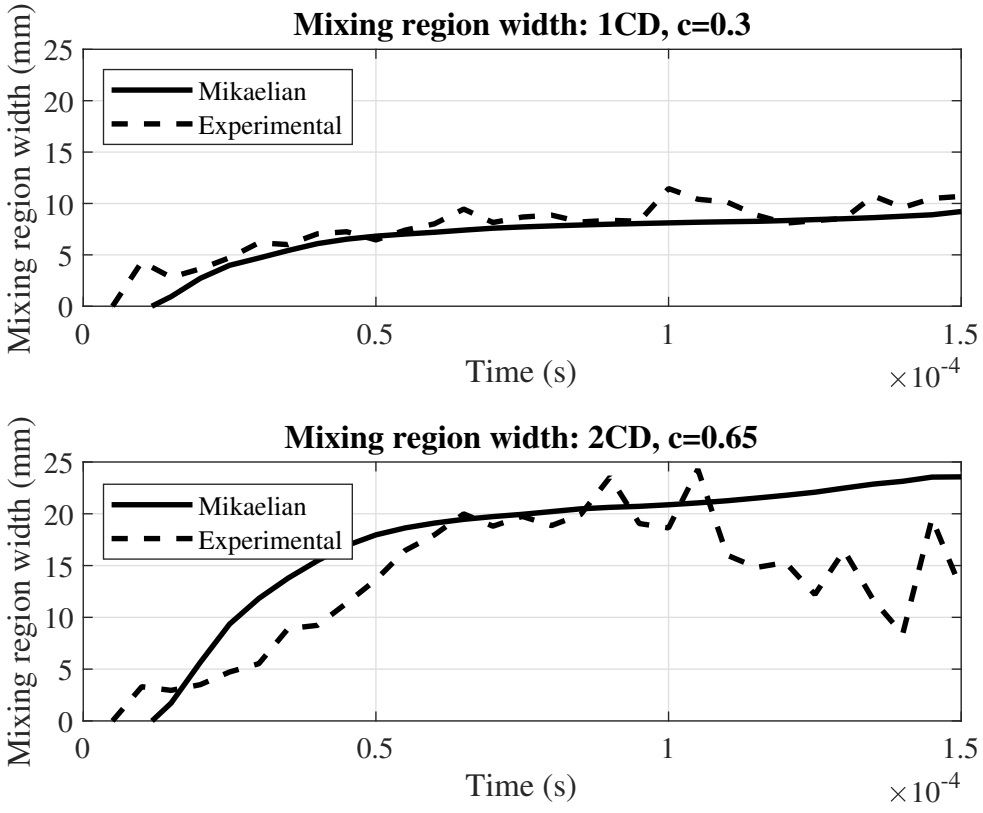

Figure 5.14: The mixing region width as a function of time is presented for the experimental data and the Makaelian prediction for the (a) 1CD and (b) 2 CD cases. The parameter c is found to vary with the geometry of the experiment.

However, the presence of only the c parameter is predicated on neglecting the impact of the initial growth rate. Data from very early time explosively driven mixing is frequently noisy, and it is advantageous to be able to predict mixing region growth based on incomplete time information. If the initial time t_a is taken as non-zero, the integral equations are broadened to no longer be able to neglect the initial growth rate term. That initial growth rate term is tuned using the parameter k, the evolution of which has not been previously discussed in literature. The parameters were fit to the mixing region data of each confinement. The fit was done using a least-squares regression. The evolution of the parameter k is shown in Table 5.2.

The parameter k is a necessary tuning parameter that is dependent on both external geometry and selected initial seed time t_a.

Table 5.2: Variation of k and c parameters with spacing and initial time. The later seeding time $t_a = 0.000055$ s shows a reduced sensitivity for the parameter c.

	$t_a = 0.00003$ s		$t_a = 0.000055$ s	
Spacing	k	c	k	c
1 CD	0.09	0.125	0.025	0.3
2 CD	0.25	0.2	0.75	0.1
5 CD	0.2	0.05	0.05	0.1
10 CD	0.45	2.0	0.15	0.3
15 CD	0.1	1.0	0.125	0.1
Open Faced	0.2	4.0	0.3	0.1

Due to the difficulty in estimating initial parameters for the gas perturbation, the experimental results were fed to the analytical methods with non-zero initial times. The definite integrals found in Mikaelian support an arbitrary time interval t_0 to t as long as a time radius history, mixing region height h_a, and initial growth rate $\frac{\partial h_a}{\partial t}$ are known. The behavior of the analytical solution is highly sensitive to the value for $\frac{\mathrm{d}h_a}{\mathrm{d}t}$, which for shotgun primer expansion is on the order of $8 \cdot 10^5$ m/s^2. The noise in raw radius measurements is sufficient to introduce significant variation in the derived velocity and acceleration estimates. This is seen as a high deviation between the model and experimental results after $t_a = 0.0001$ s. Seeding the model at a later time t_a causes a reduction in the value of c required to achieve reasonable agreement. However, with the high noise inherent in numerical derivatives, the variation in calculated initial velocity drives the value of the fitting parameter k away from agreement with c. Without the corrective factor k, the analytical models begin to under-predict the mixing region width based on experimental radius data.

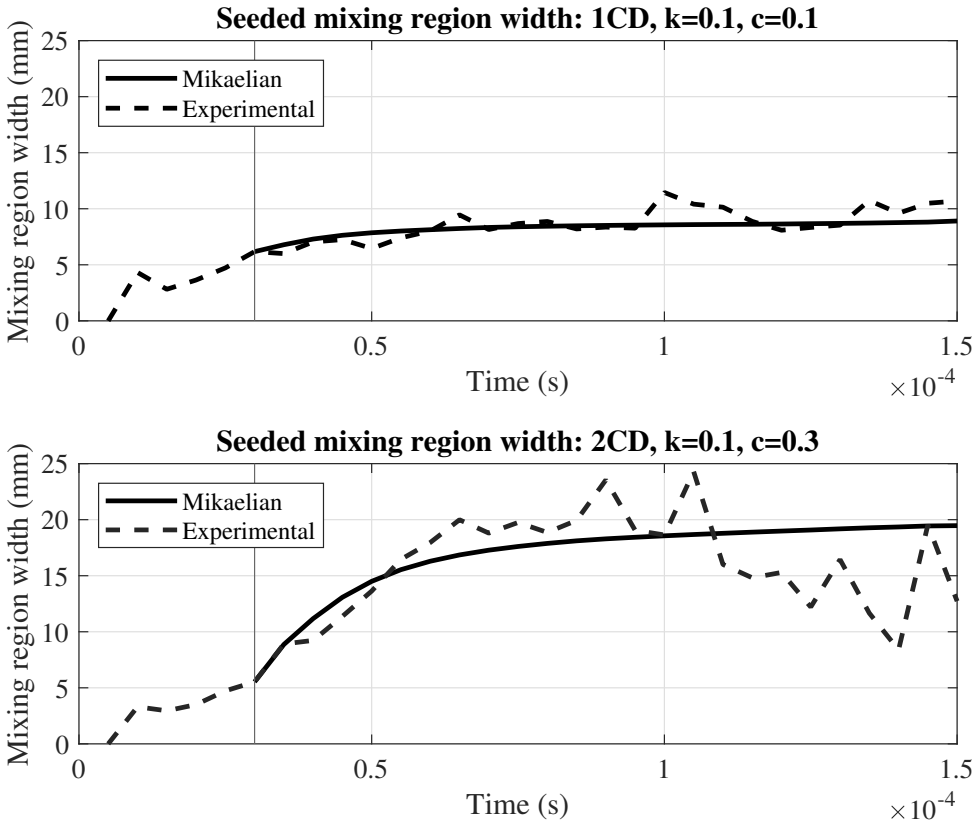

Figure 5.15: At 1 CD, seeding the Mikaelian model with data from $t_a = 0.00003$ s, using constants of $c = k = 0.1$, good agreement is achieved between the predictive model and the experimental data. For the 2 CD data, using constants of $c = 0.3$ and $k = 0.1$, good agreement is seen in the early and mid-time, but as the gas cloud exits the field of view the automatic extraction produces an artificially small mixing region, which diverges from the model.

5.2.2 Analytical models for the growth of mixing in the perturbed high explosive spheres

The same modified Mikaelian fit developed from work with shotgun primer driven gas clouds [101] was applied to the perturbed sphere data. Equation 5.5 is a restatement of evolution of a perturbation in a spherical expanding shell.

$$h(t) = h(0) + R_0^3 \frac{\mathrm{d}h_0}{\mathrm{d}t} \int_0^t \frac{dt}{R^3} + c\mathcal{A} \int_0^t \left(\frac{1}{R^3} \int_0^t R^3 \ddot{R} dt' \right) dt \tag{5.5}$$

There is an implied assumption in Equation 5.5 of the Atwood number $\mathcal{A}$ remaining constant with time, allowing it to be pulled out of the integrals. In the context of an explosion, the density ratio between the product gases and the air does not remain constant. When treating the Atwood number as a function of time, it remains within the double integral in the third term. The second term is assumed to be zero due to there being no initial perturbation growth rate ($\frac{\mathrm{d}h_0}{\mathrm{d}t} = 0$), which yields:

$$h(t) = h(0) + c \int_0^t \left(\frac{1}{R^3} \int_0^t \mathcal{A} R^3 \ddot{R} dt' \right) dt \tag{5.6}$$

However, for an explosive experiment it is advantageous to retain the second term, and reform the integral as between an initial known mixing state at t_a and the end time t:

$$h(t) = h(t_a) + R_0^3 k \frac{\mathrm{d}h_a}{\mathrm{d}t} \int_{t_a}^t \frac{dt}{R^3} + c \int_{t_a}^t \left(\frac{1}{R^3} \int_{t_a}^t \mathcal{A} R^3 \ddot{R} dt' \right) dt \tag{5.7}$$

Equation 5.7 includes the same fitting parameter k described in the shotgun primer work. The parameter k is an indicator of the scalar offset between the experimental data and the output of the analytical model. A k of 1 indicates good agreement, $k > 1$ indicates under prediction by the model, and $k < 1$ indicates over prediction by the model.

The perturbed spheres had known initial perturbation amplitudes ($h_a = 1$ mm) and wavenumbers (f), in addition to well characterized mixing width evolution. Fits were done for both modified and unmodified Mikaelian equations. The equations were fit for each perturbation.

To assess the impact of the variable Atwood number on the efficacy of the model, the parameter c was determined for three variations of Equation 5.6. As a baseline, a constant Atwood number based on the initial, condensed phase density ratio was calculated by

$$\mathcal{A} = \frac{\rho_{C4} - \rho_{air}}{\rho_{C4} + \rho_{air}} \tag{5.8}$$

where $\rho_{C4} = 1500\,\mathrm{kg/m^3}$ and $\rho_{air} \approx 0.95\,\mathrm{kg/m^3}$. In this case, the specific Atwood number is not crucial to the effectiveness of the fit, as it is a constant modifier to the parameter c. Figure 5.16 shows the resulting fits for all perturbations and

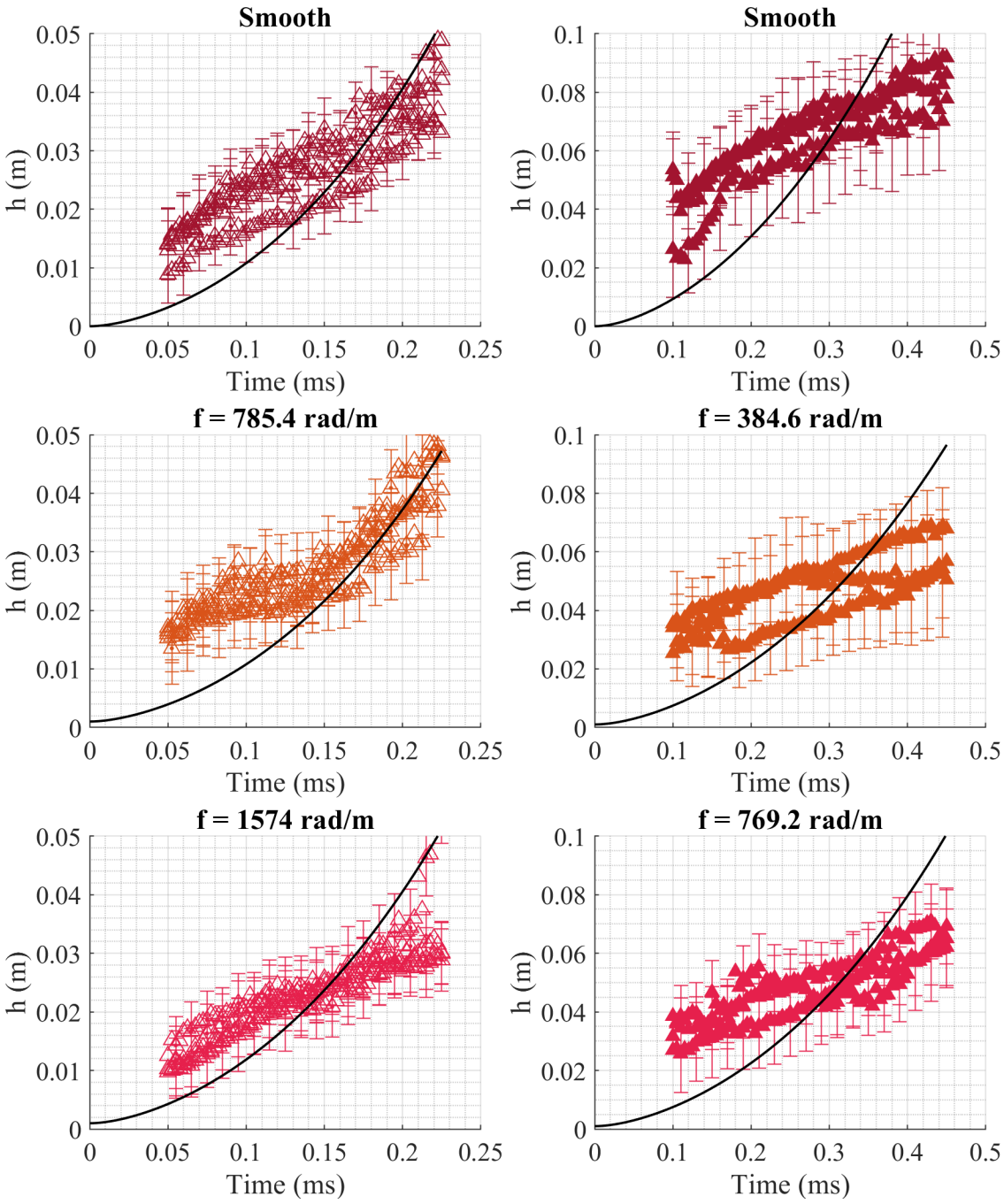

Figure 5.16: The results of fitting Equation 5.5 with a constant Atwood number to experimental mixing region results for (left column) 105 g charges and (right column) 880 g charges.

masses. The exponential growth predicted by models of the linearized regime results in under-prediction initial, then over-prediction at the tail of the data.

By allowing the Atwood number to vary with time, the model can be reactive to the significant temporal variation in relative densities found at the contact surface. The Atwood number was calculated with respect to time by

$$\mathcal{A}(t) = \frac{\frac{m_{c4}}{4/3\pi R(t)^3} - \rho_{air}}{\frac{m_{c4}}{4/3\pi R(t)^3} + \rho_{air}} \tag{5.9}$$

where the density of the explosive product gas was estimated by evenly distributing the charge mass over the volume of the fireball. The intention was to capture the changing dynamics of the fireball as it over-expands, switching sign of the density ratio. Figure 5.17 shows the variation of the Atwood number as a function of time based on Equation 5.9. Figure 5.18 shows the resulting fits for all perturbations and masses. The variation of the Atwood number improves the agreement with the early experimental data, but the change of sign in the Atwood number as the ambient air becomes denser than the expanding product gases results in the predicted mixing width becoming negative.

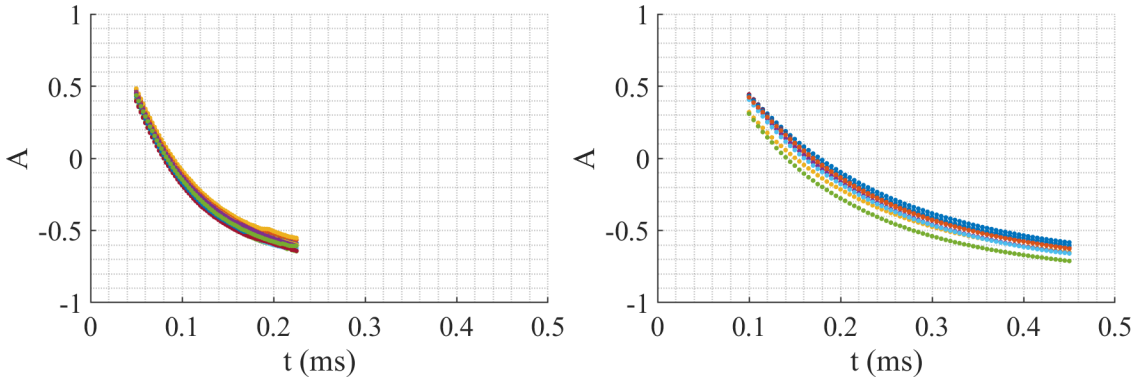

Figure 5.17: The evolution of the Atwood number for (left) the 105 g charges and the (right) 880g charges.

To account for the change in sign, the absolute value of the variable Atwood number was computed. Figure 5.19 shows the resulting fits for all perturbations and masses. The identified value for the fitting parameter c is reported for all treatments of the Atwood number in Table 5.3 and Table 5.4 for 105 g and 880 g charges, respectively.

The modified Mikaelian model coefficients c and k presented in Equation 5.7 were computed using the absolute value of the variable Atwood number. Figure 5.20 shows the fits for $t_a = 0.05$ ms and $t_a = 0.1$ ms from the 105 g and 880 g charges, respectively. Table 5.5 and Table 5.6 reports the values fit values of c and k. The addition of k shifts the fit towards the center of the data by disconnecting it from the initial surface perturbation. However, the modified model does

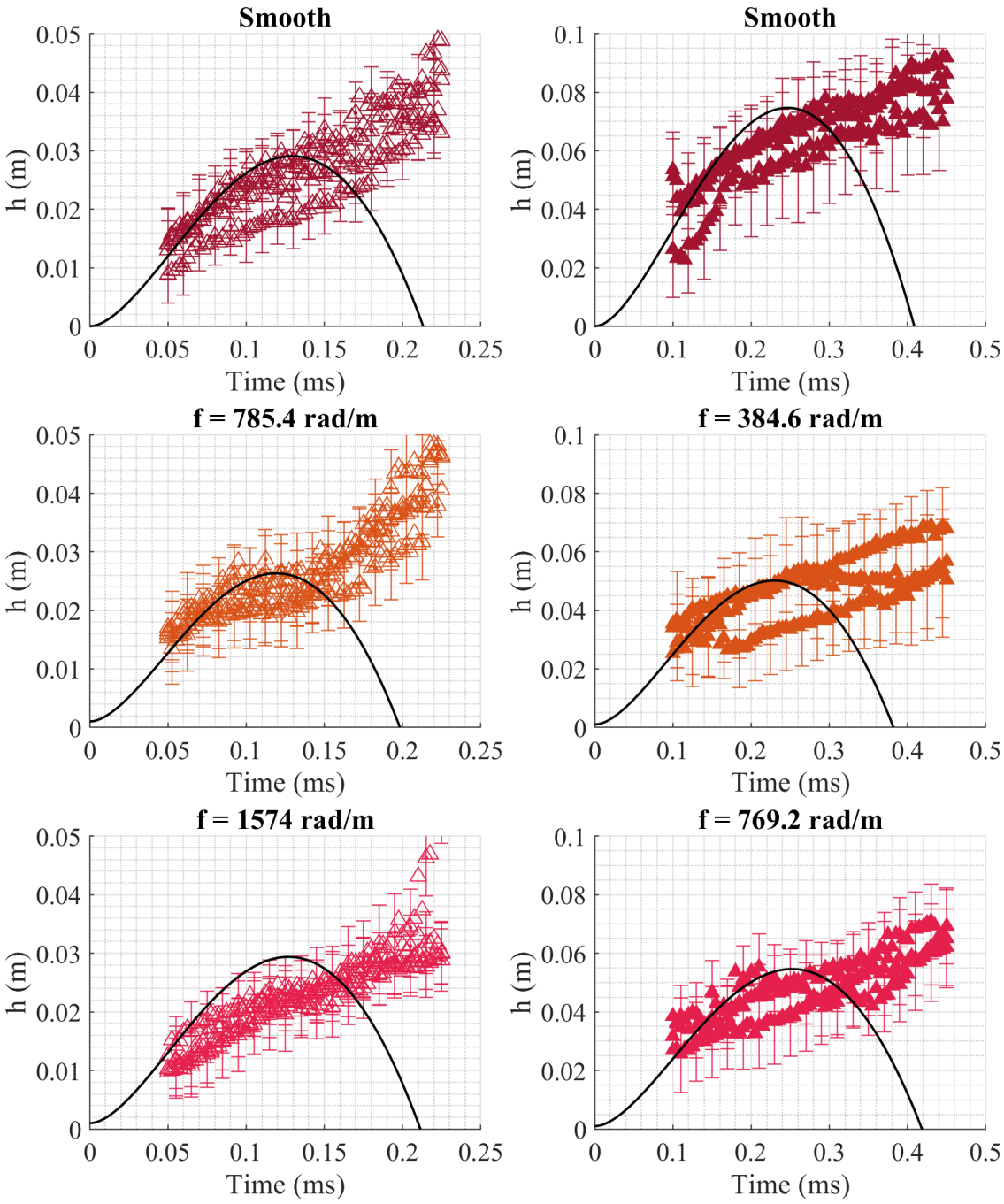

Figure 5.18: The results of fitting Equation 5.6 with an estimated variable Atwood number to experimental mixing region results for (left column) 105 g charges and (right column) 880 g charges.

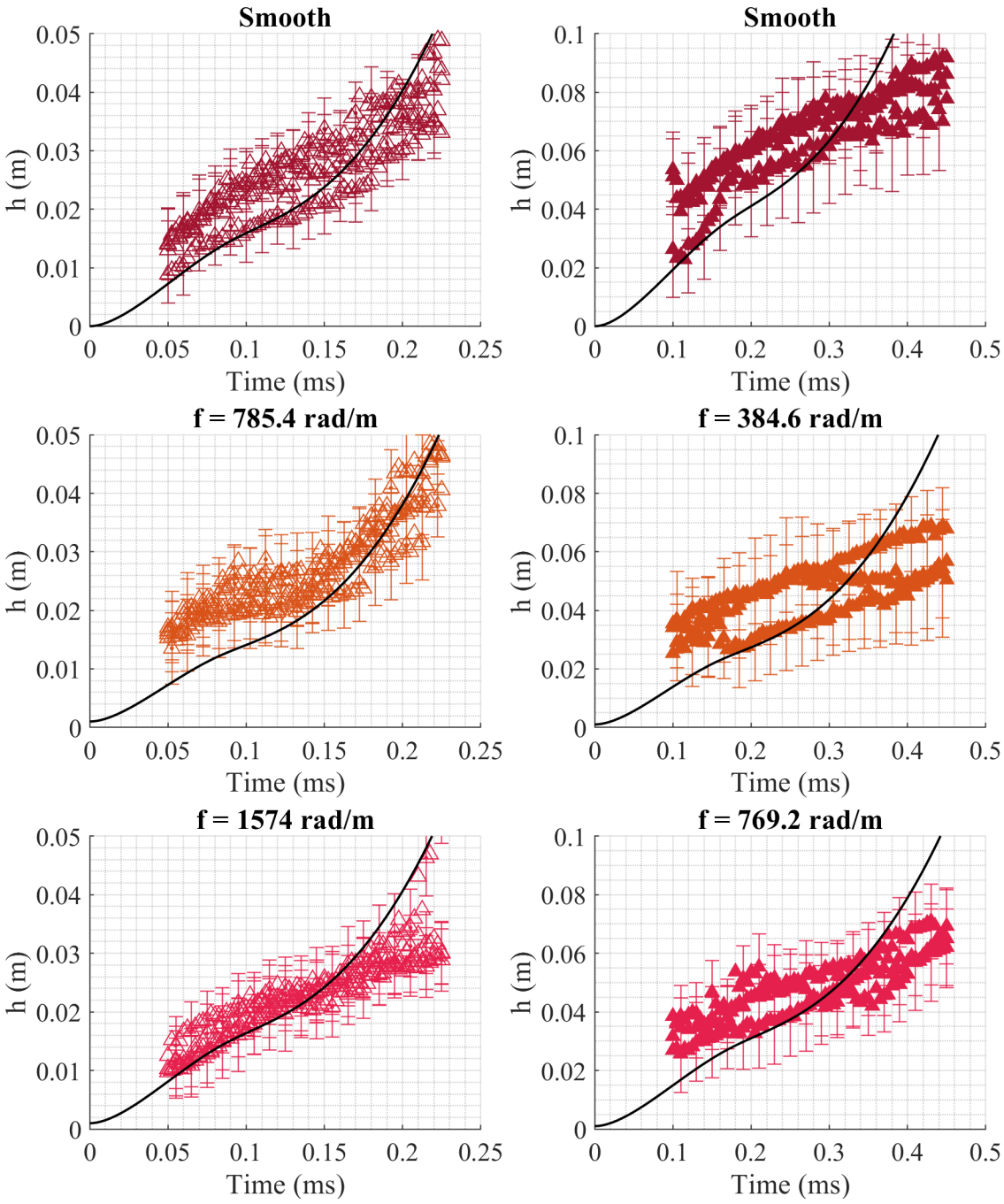

Figure 5.19: The results of fitting Equation 5.6 with the absolute value of an estimated variable Atwood number to experimental mixing region results for (left column) 105 g charges and (right column) 880 g charges.

Table 5.3: Variation of fitting parameter c for Equation 5.6 by perturbation for the 105 g charges. Three different methods of computing Atwood number are reported: constant Atwood number computed for the pre-detonation condensed phase, variable Atwood number that is allowed to go negative, and the absolute value of the variable Atwood number. The numbers in brackets are the 95% confidence intervals.

	Constant	Variable	Absolute Value
Smooth	-0.51 [-0.55, -0.47]	-2.5 [-2.6, -2.3]	-1.5 [-1.6, -1.4]
f = 785.4 rad/m	-0.47 [-0.51, -0.44]	-2.6 [-2.7, -2.4]	-1.4 [-1.5, -1.3]
f = 1574 rad/m	-0.59 [-0.63, -0.54]	-2.9 [-3, -2.8]	-1.7 [-1.8, -1.6]

Table 5.4: Variation of fitting parameter c for Equation 5.6 by perturbation for the 880 g charges. Three different methods of computing Atwood number are reported: constant Atwood number computed for the pre-detonation condensed phase, variable Atwood number that is allowed to go negative, and the absolute value of the variable Atwood number. The numbers in brackets are the 95% confidence intervals.

	Constant	Variable	Absolute Value
Smooth	-0.83 [-0.88, -0.78]	-4.2 [-4.4, -3.9]	-2.4 [-2.5, -2.3]
f = 384.6 rad/m	-0.6 [-0.64, -0.57]	-3.2 [-3.5, -2.9]	-1.7 [-1.8, -1.6]
f = 769.2 rad/m	-0.57 [-0.61, -0.54]	-2.7 [-2.9, -2.6]	-1.6 [-1.7, -1.6]

not exhibit the same characteristic upwards deviation of the unmodified model (Equation 5.6).

The behavior of the k parameter is surprising for two reasons. The methods used to estimate the perturbation width from the experimental data were designed to produce a conservative value. As the fireball surface complexity increases, the likelihood of the extracted fireball contour being influenced by 3D mixing effects and returning a lower value for the mixing region also increases. In the context of the transition out of a linear mixing regime, the value of k is amplifying the impact of positive radius integral and initial growth velocity term, which is counter-acting the sign change in the Atwood number.

Table 5.5: The fitting parameters c and k from Equation 5.7 for 105 g charges using the absolute value of the variable Atwood number. The numbers in brackets are the 95% confidence intervals.

	c	k
Smooth	-0.26 [-0.36, -0.16]	2.3 [2.1, 2.6]
f = 785.4 rad/m	-0.83 [-1, -0.61]	0.98 [0.84, 1.1]
f = 1574 rad/m	-0.31 [-0.38, -0.24]	1.7 [1.6, 1.8]

Table 5.6: The fitting parameters c and k from Equation 5.7 for 880 g charges using the absolute value of the variable Atwood number. The numbers in brackets are the 95% confidence intervals.

	c	k
Smooth	-0.19 [-0.31, -0.066]	2 [1.7, 2.2]
f = 384.6 rad/m	-0.13 [-0.27, 0.0065]	1.6 [1.3, 1.9]
f = 769.2 rad/m	-0.21 [-0.34, -0.078]	1.6 [1.3, 1.8]

All perturbations show a upward trend in the late time. Figure 5.21 shows the fit curves for each perturbation from the unmodified Mikaelian model with the absolute value treatment of the Atwood number (Figure 5.19) on the same axes. When scaled, the fits collapse well to a single curve. The shift in behavior initially described with Figure 5.9 at 0.033 scaled time. The growth of the model values away from the experimental values after this point indicates a shift in mixing behavior. The scaled mixing region width at this point is $h^* = 0.016$. The identified values of c vary between -1.4 and -2.5. Removing the 880 g smooth case, the variation reduces to between -1.4 and -1.7, with an average value of -1.58, and appears to be indicative of the behavior of this charge geometry. Figure 5.22 shows the Mikaelian fit for the average c value in scaled units. The value of the mixing width is under-predicted for most of the data, but the slope of the early time data agrees with the model. After a scaled time of $t^* = 0.03$, the slope of the fit diverges from the slope of the data. The averaged value for c appears to be representative of the mixing evolution for this charge configuration prior to

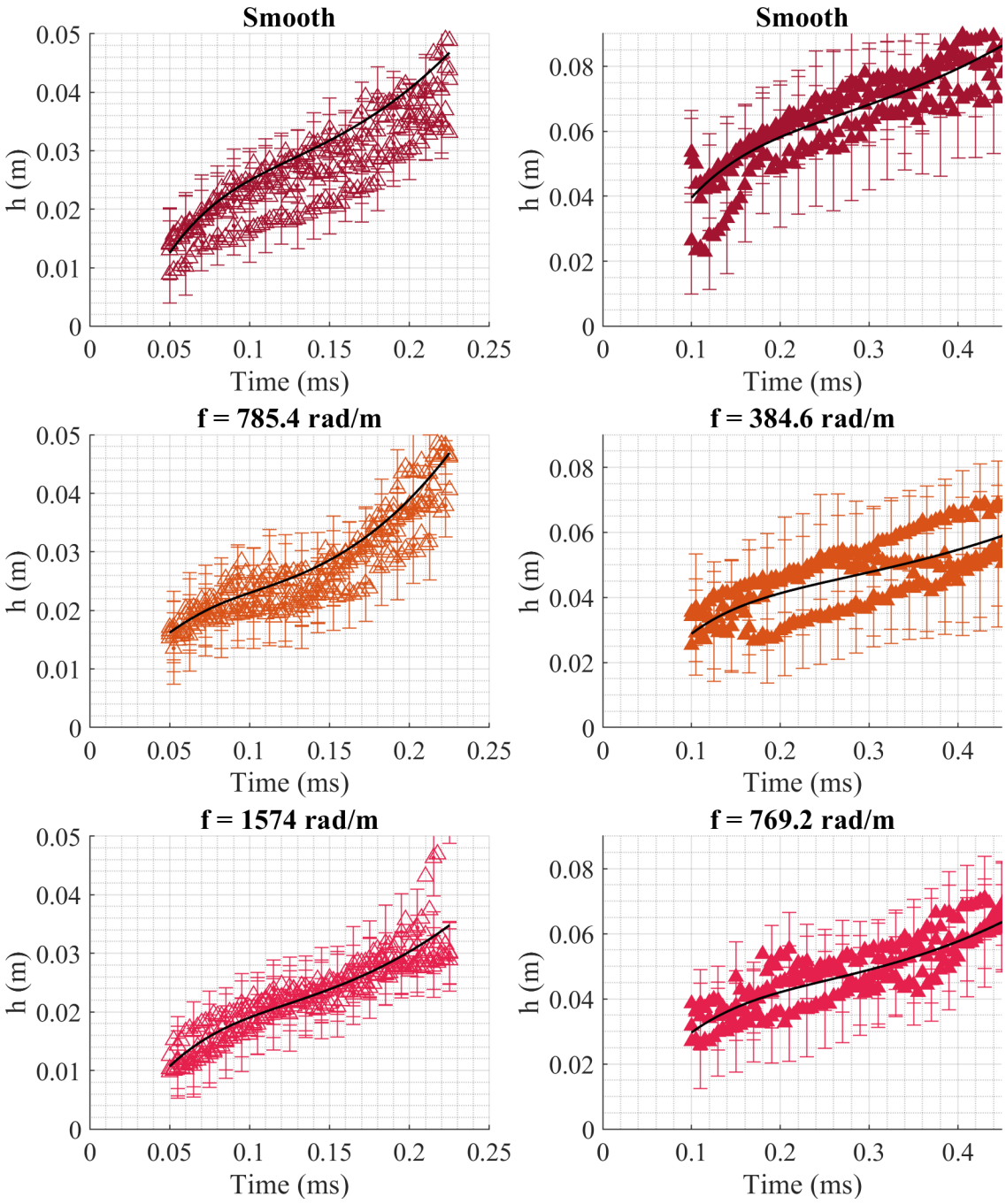

Figure 5.20: The results of fitting the modified Mikaelian equations to the experimental mixing region results for (left column) 105 g charges and (right column) 880 g charges.

$t* = 0.03$. The 880 g smooth test cases had a higher mixing region width to radius ratio than the other test cases, as seen in Figure 5.13. The ratio is important, as it relates the mixing width to the principal driving component of the model, the fireball radius, and through the radius, the estimated Atwood number.

The inclusion of the ambient density in the calculation of the Atwood number neglects the presence of the shock compression of the air immediately in front of the advancing fireball. In the time period studied, the shock is being directly driven by the gas cloud expansion, and has not sufficiently separated from the fireball for there to be attenuation of the shocked air density. To account for the change in air density, the Mach number of the shock wave M_s is determined from extracted shock velocity and the local speed of sound. The shock velocity U is determined by using a centered difference method on the extracted fireball radius R. The Mach number is then calculated by

$$M_s(t) = \frac{U(t)}{C_0} \tag{5.10}$$

The density jump across a normal shock wave is determined by a relationship between Mach number M_s and the shocked medium ratio of specific heats γ [114].

$$\frac{\rho_2}{\rho_1} = \frac{\frac{m_{c4}}{4/3\pi R(t)^3} - \rho_s}{\frac{m_{c4}}{4/3\pi R(t)^3} + \rho_s} \tag{5.11}$$

The air density behind the shock wave ρ_s and directly behind the shock wave is a function of time calculated by

$$\rho_s(t) = \rho_a \frac{(\gamma+1)M_s(t)^2}{(\gamma-1)M_s(t)^2 + 2} \tag{5.12}$$

The Mach number of the shock wave is high, decreasing from 8 towards 2 over the course of the fireball expansion. The density ratio varies from 5.56 to 2.66. The time variant value for the Atwood number using the shocked air as the second medium is

$$\mathcal{A} = \frac{\rho_{C4} - \rho_s}{\rho_{C4} + \rho_s} \tag{5.13}$$

The increase in density shifts the inflection point of the Atwood number earlier in the evolution of the fireball. The impact of the earlier inflection point is seen in Figure 5.23. The earlier sign change causes significant underestimation of the mixing width.

Applying the estimated shocked Atwood number to the complete Mikaelian model with initial growth rate term in Equation 5.7 improves the agreement of the model with the data. The parameter k was fixed at 1, and only the value for c was fit. Tables 5.7 and 5.8 report the value for c by perturbation for 105 g and 880 g charges, respectively. The average c value for the 105 g charges is -0.36, -0.26 for 880 g charges, and -0.31 across all masses and perturbations. The higher

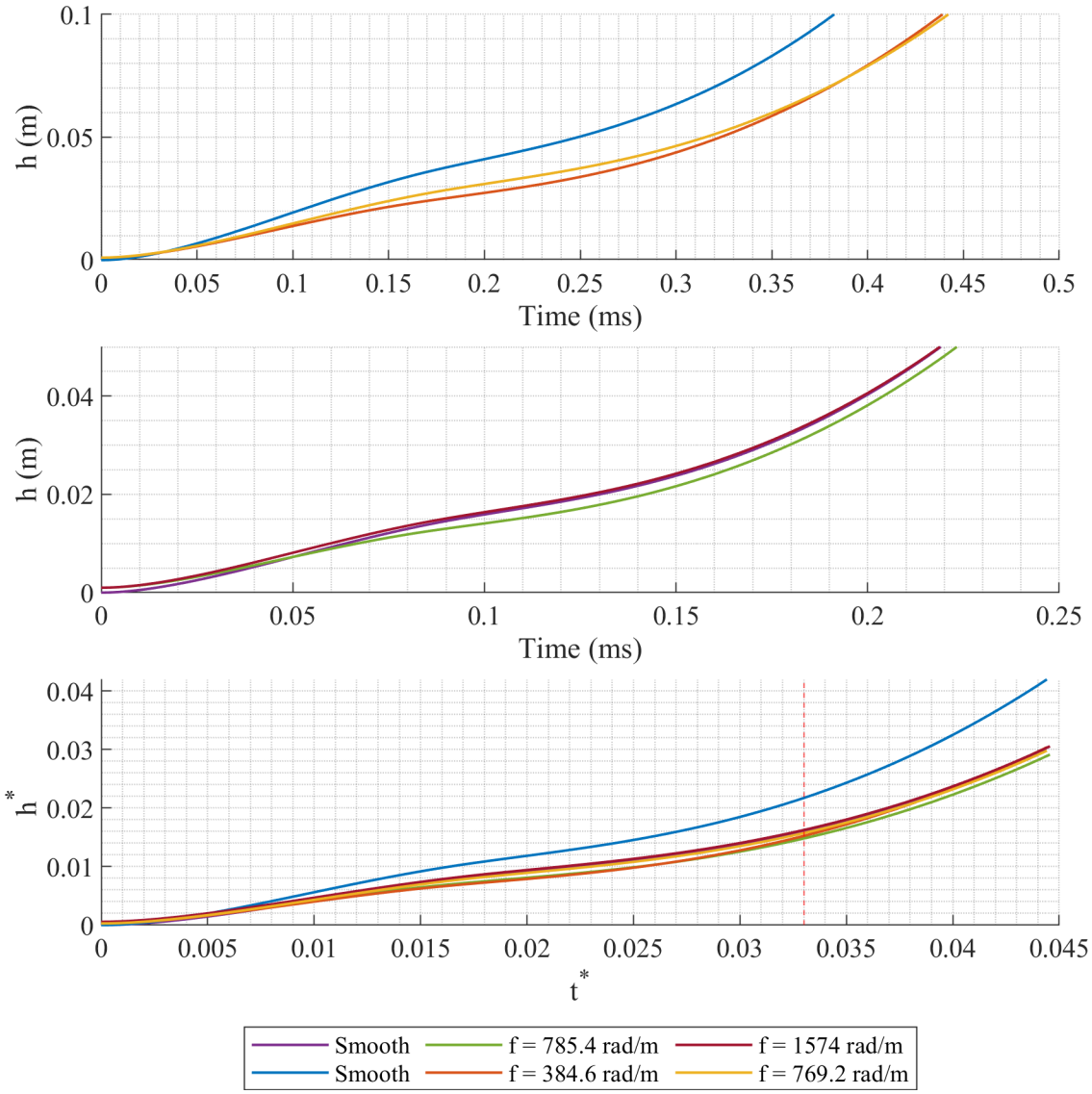

Figure 5.21: Fit line for all perturbations from (top) 105 g and (middle) 880 g charges. (bottom) Scaling the mixing width and time by the characteristic values shows a collapse to a single representative fit. The red dashed vertical line represents the shift of behavior first described in Figure 5.9. The 880 g smooth charges have $c = -2.5$, while the other perturbations have $-1.7 < c < -1.4$.

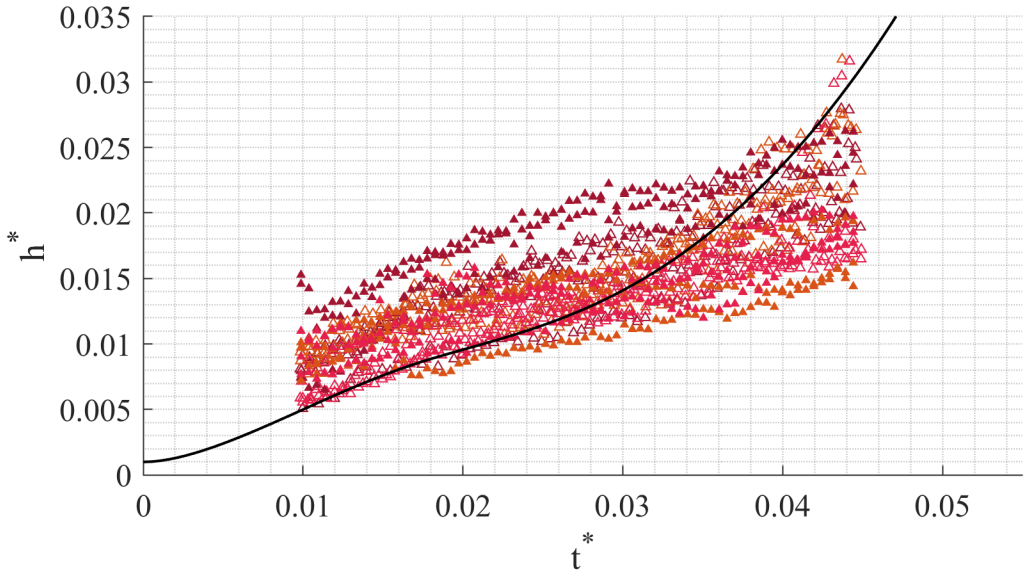

Figure 5.22: Fit line for the average fit value of $c = 1.58$ for Equation 5.6.

c value corresponds to a increase in curvature towards to the end of the data, as exemplified in the difference between the 105 g smooth and 105 g f = 785.4 rad/m cases. The third term of Equation 5.7 is dominant in the late time due to the R^3 term, so varying c has greater impacts as time increases.

Table 5.7: The fitting parameter c from Equation 5.7 for 105 g charges using the absolute value of the variable shocked Atwood number. The numbers in brackets are the 95% confidence intervals.

	c
Smooth	-0.45 [-0.48, -0.42]
f = 785.4 rad/m	-0.26 [-0.28, -0.24]
f = 1574 rad/m	-0.37 [-0.39, -0.35]

Using the average fit value for c, a scaled Mikaelian fit was computed. Figure 5.25 shows the averaged fit over all 105 g and 880 g data. The averaged fit is representative of the slope in h^* before $t^* = 0.03$, but trends upwards away from the bulk data trend in the later time. The divergence in slope is less severe than seen in Figure 5.22, indicating that the transition to a more physically representative Atwood number may extend the time range under which this model is accurate. The upwards trend is principally influenced by the smooth charge cases, which have consistently higher c values than the perturbed cases.

Comparing the universal value of c found for the shocked air treatment of the Atwood number to the values found for the open faced shotgun primers in

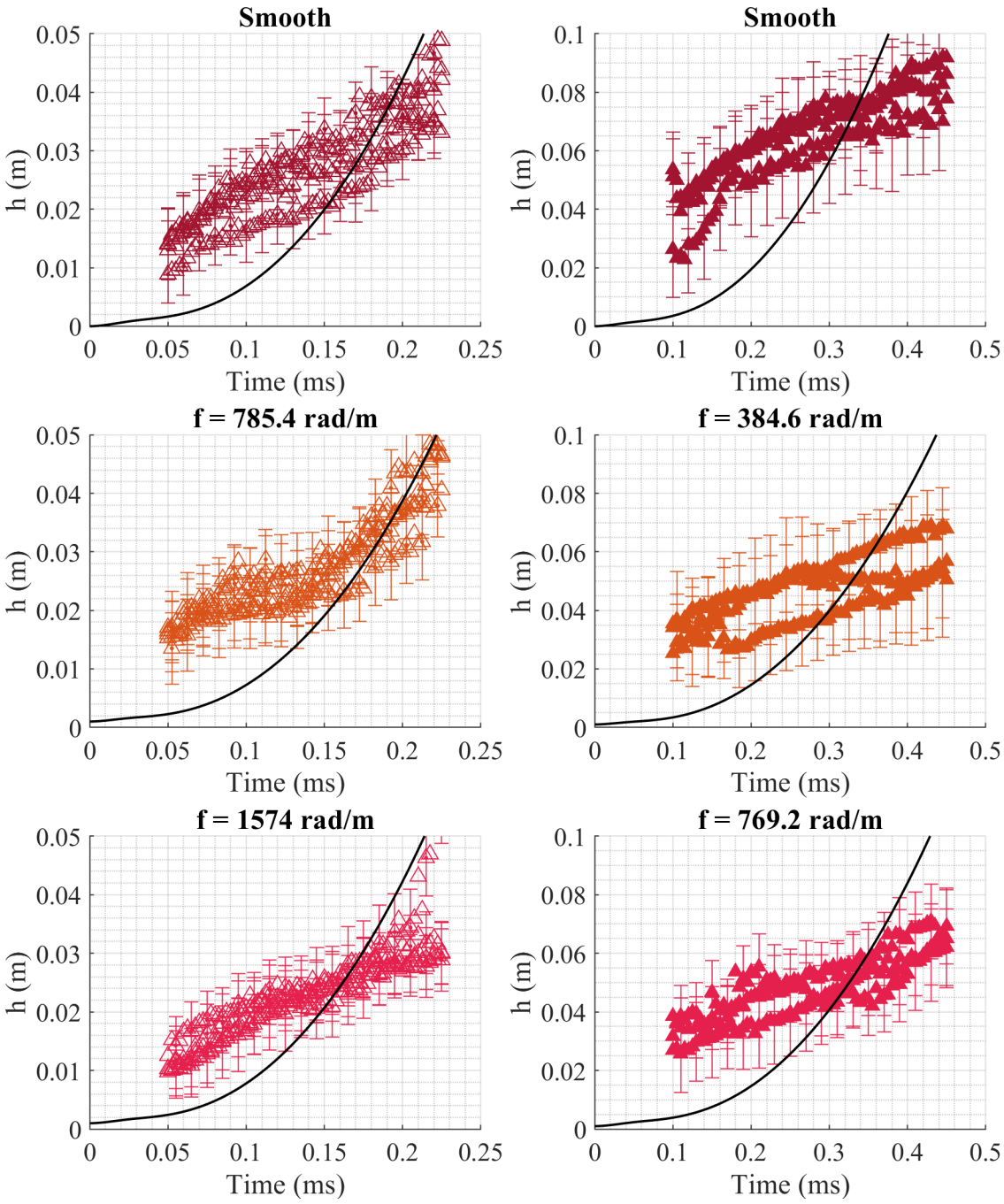

Figure 5.23: The results of fitting Mikealian equations with the ambient density replaced by the estimated shocked air density to the experimental mixing region results for (left column) 105 g charges and (right column) 880 g charges.

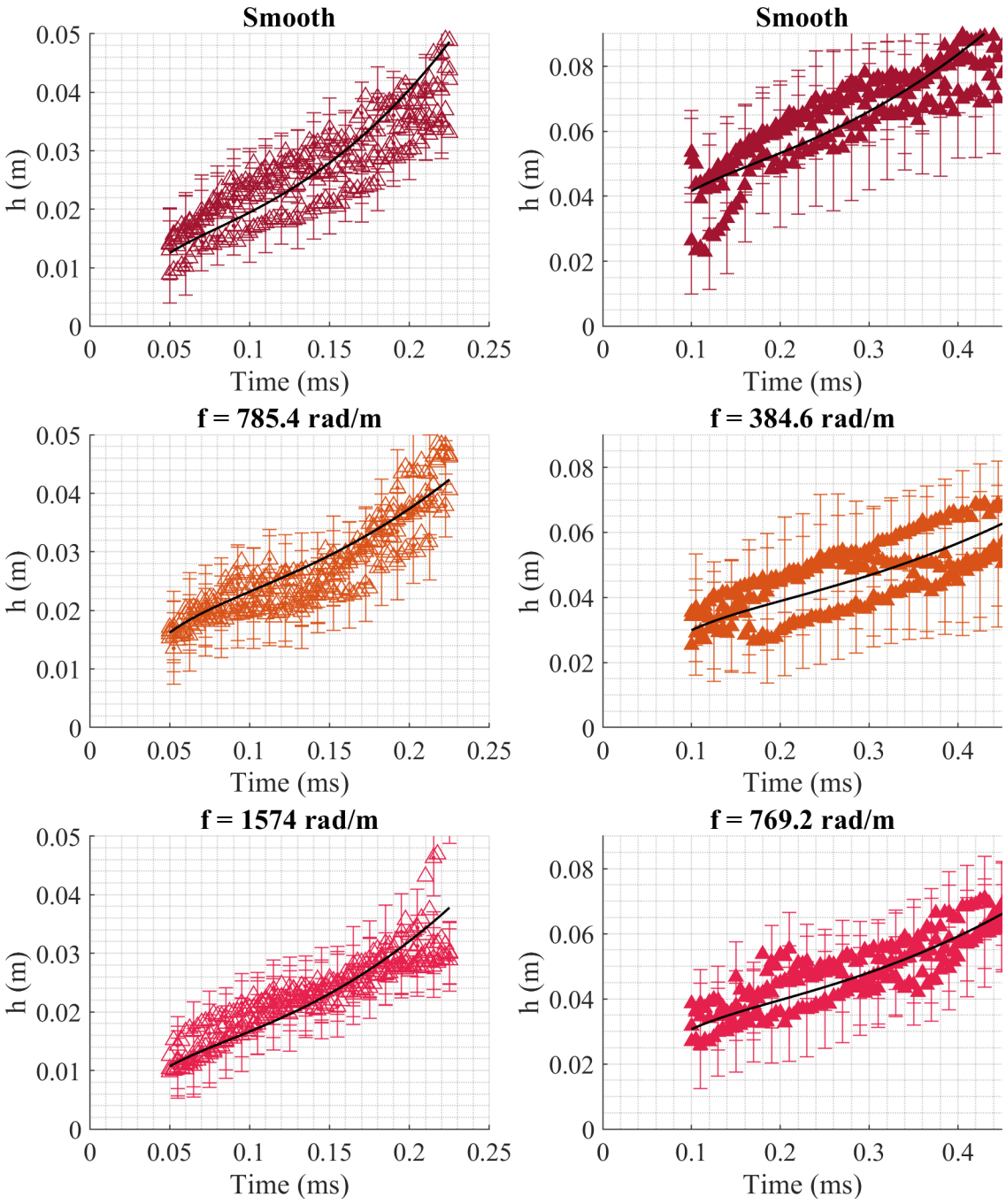

Figure 5.24: The results of fitting the Equation 5.7 with the ambient density replaced by the estimated shocked air density to the experimental mixing region results for (left column) 105 g charges and (right column) 880 g charges.

Table 5.8: The fitting parameter c from Equation 5.7 for 880 g charges using the absolute value of the variable shocked Atwood number. The numbers in brackets are the 95% confidence intervals.

	c
Smooth	-0.37 [-0.4, -0.33]
f = 384.6 rad/m	-0.2 [-0.23, -0.17]
f = 769.2 rad/m	-0.22 [-0.24, -0.19]

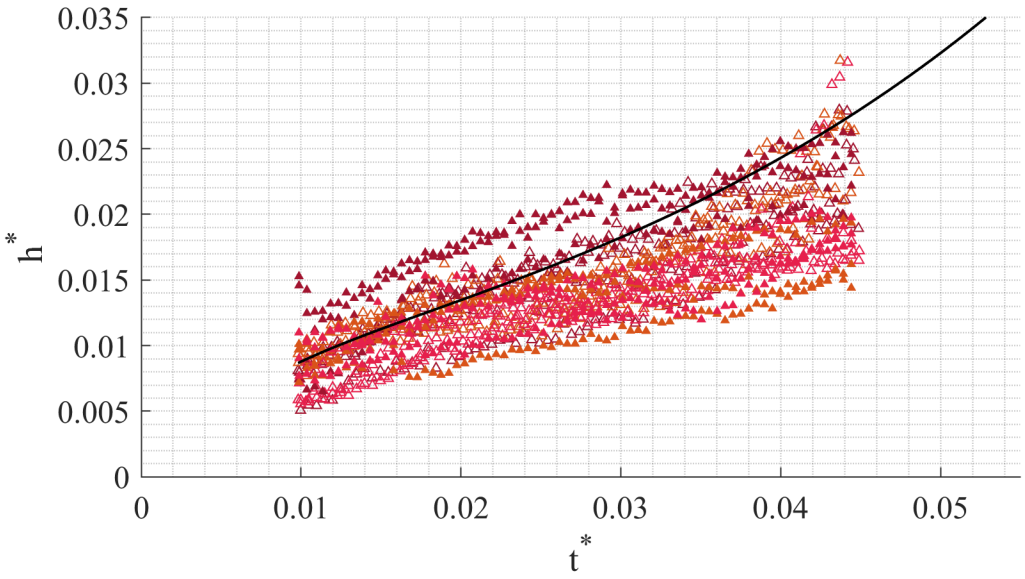

Figure 5.25: A fit to Equation 5.7 with an average c value of -0.31, and a fixed k value of 1, scaled using the Wei-Hargather characteristic lengths and times.

Table 5.2, the influence of the gas cloud geometry is apparent. In an open faced configuration, the primer driven gas cloud was more similar to a jet than an expanding cylinder or sphere of gas. The c parameters are therefore quite different. The high confinement cases, however, were more representative of the ideal expanding cylinder geometry represented by the model, and show a similar value for c to the results for the spherical expansion case.

The reasons for poor fit when working from t_0 can potentially be explained by considering the assumptions on the initial growth of the system. As was described, the radius of the initial perturbation in the charge geometry is 25 times and 50 times smaller than the charge radius for the 105 g and 880 g charges, respectively, but grows to around 10 times smaller, as seen in Figure 5.13. In the early time, before an effective mixing width can be estimated, the width ratio increases at a rate much higher than recorded after 0.01 scaled time. This is an indicator that the flow has already transitioned out of the early linearized regime that is the primary focus of the Mikaelian analytical models. The angular wavelength of these perturbations straddled the boundary between what is typically considered as part of the linear regime [13, 115]. Furthermore, the adoption of the variable Atwood number changes the underlying exponential behavior of the model. The shift in relative density towards the air as the fireball over-expands occurs at approximately 11.5 charge radii, and the impact is apparent in the inflection of the fit. This is supported by the significant improvement in fit achieved by limiting the scope to data prior to the slight observed change in mixing growth behavior. The behavior of the model with respect to the early time data indicates a potential crossover point where the transition from the linear regime is complete. While the 105 g mixing widths appear to continue to increase, the 880 g width has a trend that levels off which is supported by the camera 3 data.

The mixing region width was extracted from direct imaging of the fireball. The explosives were configured to have known dominant perturbations. The presence of initial perturbations had minimal impact on the evolution of the mixing rate as a function of normalized time. This conclusion is supported by the consistent fitting parameters calculated for the Mikaelian analytical mixing model.

CHAPTER 6

THE FRACTAL BEHAVIOR OF FIREBALL CONTOURS

The goal of this research was to characterize the relationship between the development of mixing on the surface of a fireball and the fractal dimension of that surface. Methodologies developed on gas cloud produced by shotgun primers were applied to extract the mixing region from explosive tests, and compare the growth of the mixing region to the change in the computed fractal dimension of the fireball contact surface. Based on the research conducted, the fractal dimension is a function of the mixing width and offers increased insight into the transition from the linear mixing regime to turbulence.

6.1 Fractal evolution of smooth spheres

The fractal dimension was estimated for the five camera angles for the three repetitions of the PBXN-113 tests. Figures 6.1 and 6.2 (reproduced Figures 3.5 and 3.7 for clarity) show the fractal evolution of each test. The fractal dimension was close to unity for much of the early evolution of these tests, but grew towards a non-unity value as the early smooth fireball expanded and became textured. The extracted fireball contours from the 0° camera returned the most consistent estimated fractal dimension, as is shown in Figure 6.2. The fractal dimension from the other cameras had more dispersion, but the underlying trends in the evolution of the fireball followed those of the center camera.

The smooth tests conducted with C4 are representative of the earlier time evolution of the fireball without the reflected shock wave interaction.

The evolution of the fractal dimension with respect to the fireball has three stages, shown in Figure 6.3. In the first stage of evolution, the fireball remains largely smooth, and returns a small fractal dimension near unity. As the fireball grows, distinct variations in radius become apparent as mixing begins to occur. The variations are non-uniform, but likely represent small surface imperfections in the original smooth sphere. Comparison to the the perturbed case in Figure 6.4 shows that there is minimal difference in the level of surface roughness between a smooth and perturbed sphere. The initial perturbations impact the structure and regularity of the fireball contour, but not in a way that changes the relative roughness of the interface.

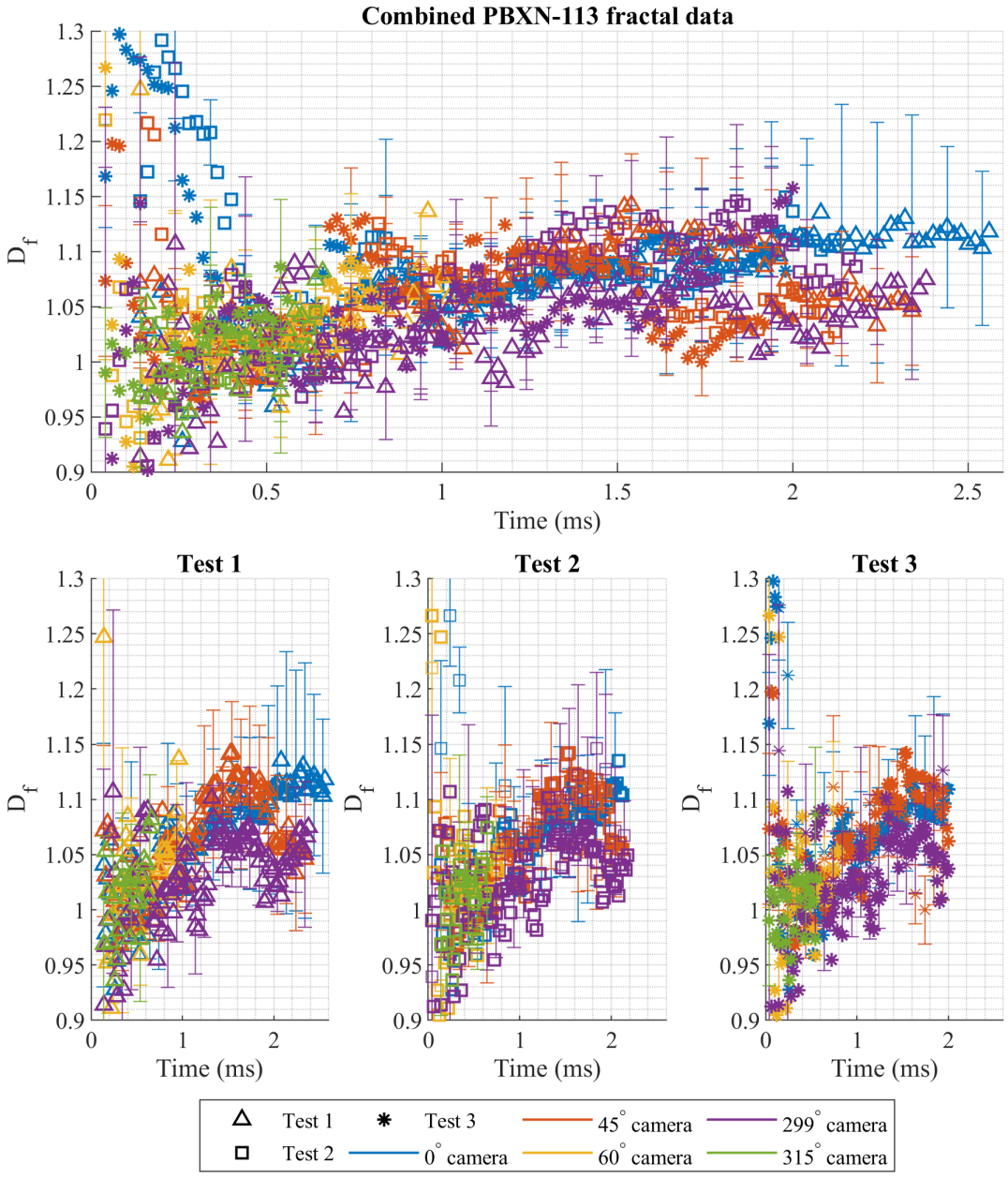

Figure 6.1: All estimated fractal dimensions (top) for 5 camera angles across 3 tests. When (bottom) broken down by test, there is good test to test agreement. There is high dispersion in the early time, but all cameras return to the same trend beyond 1 ms.

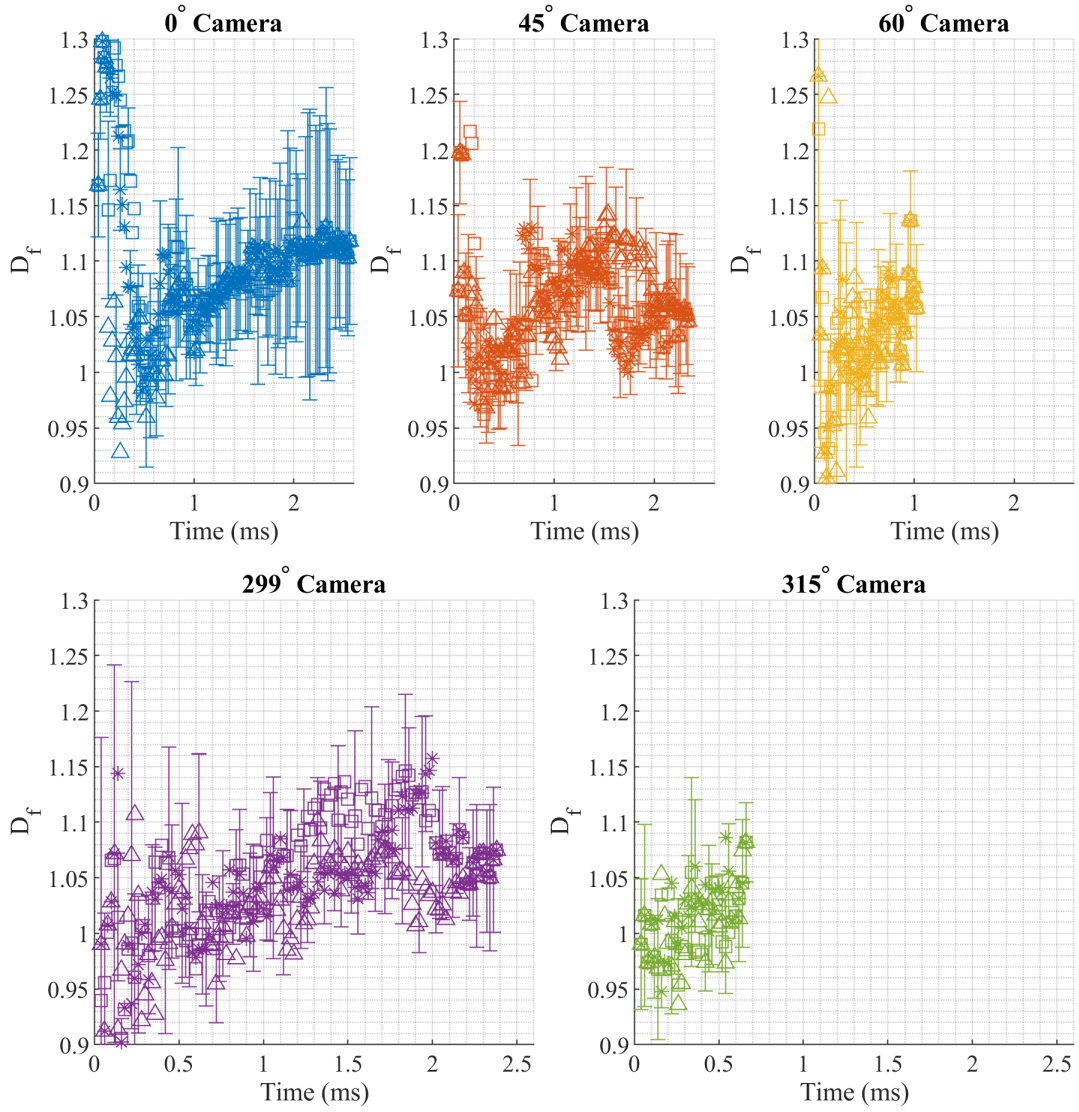

Figure 6.2: The fractal dimension of each independent camera broken down by tests. The 60° and 315° cameras either exit the field of view or become obstructed, and are cut short here.

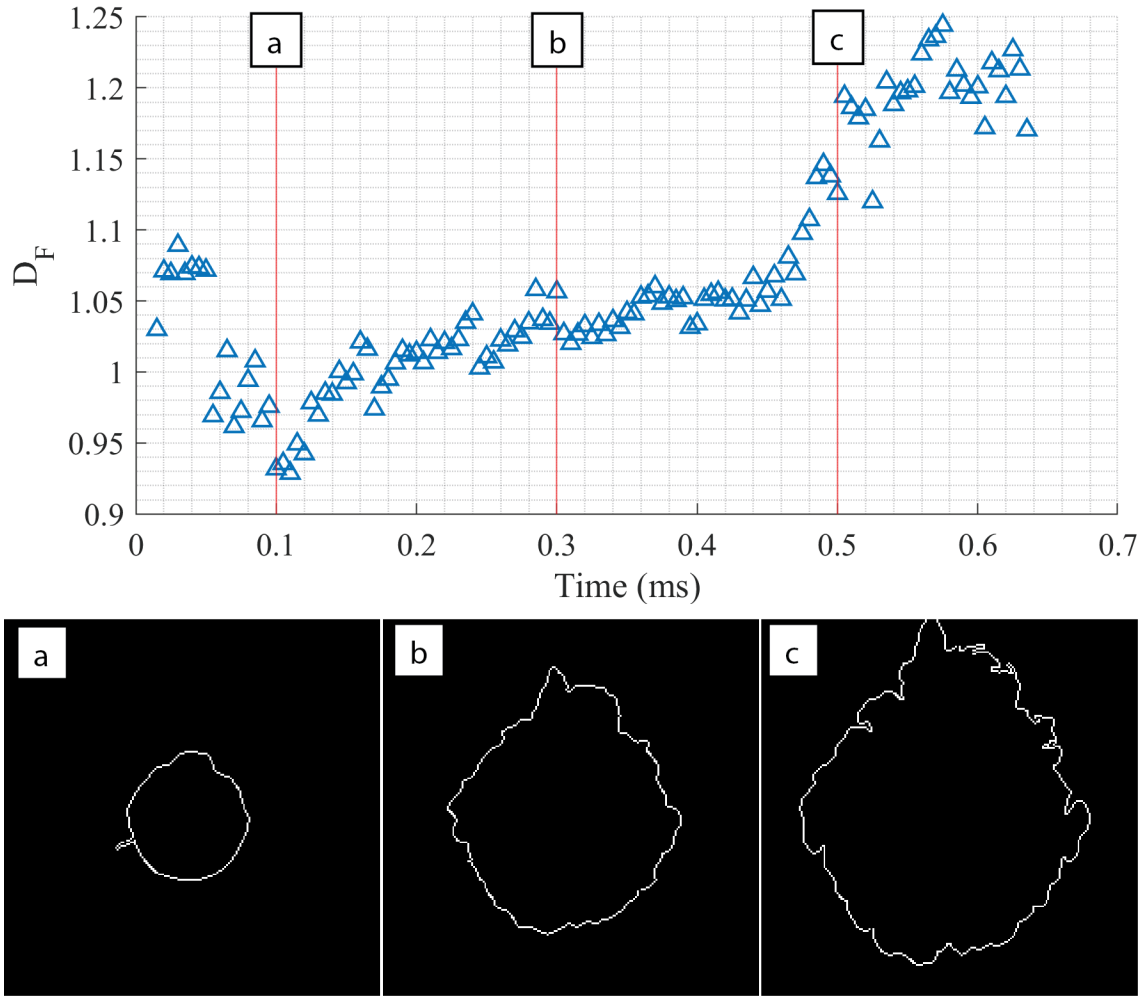

Figure 6.3: (top) The fractal dimension evolution has three regimes, exemplified here by the three frames (a, b, c). (a) Initially the fireball is smooth with limited fractal properties. (b) At the mid-time, the fireball contour has begun to develop a thickness, but is still a largely smooth curve. (c) As the fractal dimension increases, the mixing width increase is matched by an increase in the complexity of the contour. Images from the second smooth 880 g test.

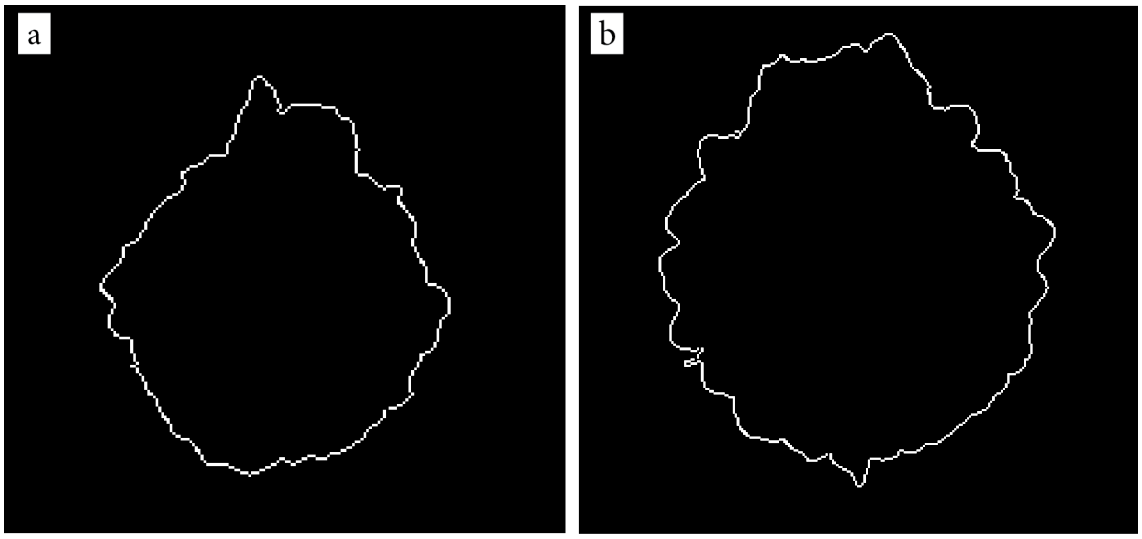

Figure 6.4: (a) The fireball contour of a smooth 880 g charge at $t = 0.3$ ms is not significantly different from (b) the fireball contour from a perturbed ($f = 384.6$ rad/m) 880 g charge at the same time.

6.2 Fractal evolution of perturbed spheres

The fractal dimension of the fireball from the perturbed spheres was computed from the data taken by camera 2. Figure 6.6 shows the evolution of the fractal dimension broken down by perturbation for the 105 g charges. At very early times, the fractal dimension is near unity as the expanding gas cloud is still largely spherical, and has not yet been significantly perturbed by mixing instabilities on the surface. The evolution of the 880 g charges, shown in Figure 6.7, is less evident than with the 105 g charges. The smooth and $f = 384.6$ rad/m tests do not significantly deviate from unity until the end of the test. The $f = 769.2$ rad/m tests show a gradual increase similar to that seen in the 105 g tests, but the growth rate is lower than all but the $f = 1574$ rad/m tests. Initial charge geometry and enforced perturbation appears to have limited impact on the initial fractal dimension, as all perturbed cases followed approximately similar trends.

As discussed with the smooth sphere charges, there is no discernible difference between the perturbations in terms of fractal evolution. The intermediate perturbation tests ($f = 384.6$ rad/m and $f = 785.4$ rad/m) retain more structure from the initial perturbation frequency than the high frequency perturbations as seen in Figure 6.5, but that structure is not accompanied by an increase or decrease in the formation of small turbulent structures within the context of the mixing region. This is supported by the similar fractal behavior seen between perturbations.

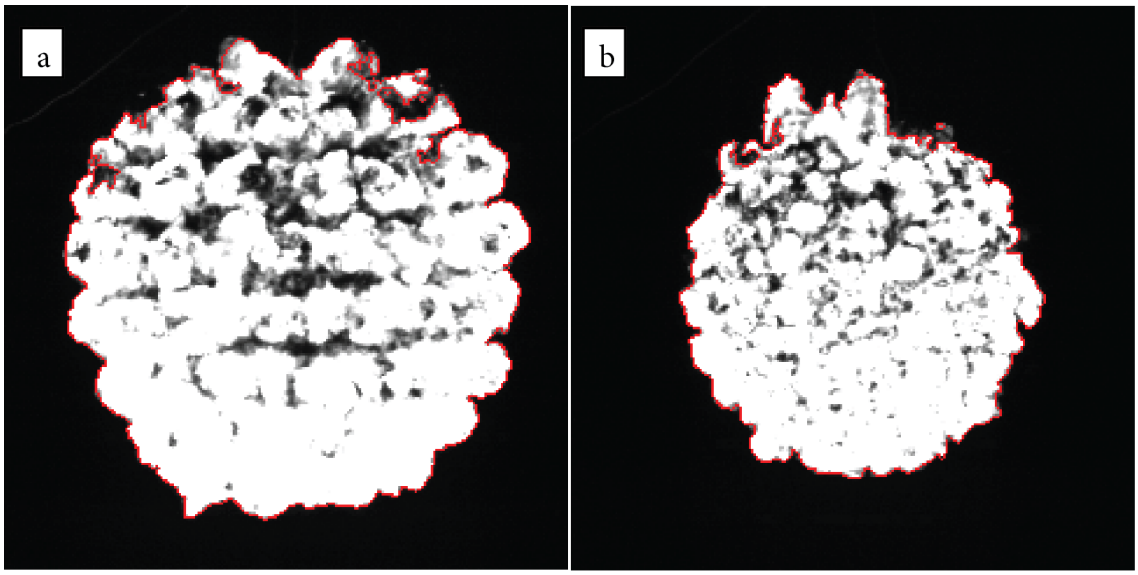

Figure 6.5: (a) The intermediate frequency initial perturbations are still strongly visible as the fireball expands, where (b) the high frequency initial perturbations have become more multi-modal. Images shown are from 105 g tests 10 and 6, respectively, taken 0.2 ms after detonation.

6.3 Scaling behavior of fractal evolution

6.3.1 Scaling of the fractal behavior of perturbed spheres

As seen in Figure 6.8, at later scaled times, the fractal dimension begins rapidly increasing as the surface begins mixing under strong Rayleigh-Taylor surface instabilities, causing the multiple length scales of turbulence to begin to form. There is no change to the estimated fractal dimension of the fireball as the expansion rate changes regimes in the the Wei-Hargather scaling. The fractal measurement is an indicator of transition of non-linear turbulence in the mixing regime. The point of transition can be identified from Figure 6.8 by locating the point of divergence in the scaled fractal measurement. The transition point is not consistent in scaled time, with the fractal dimension of the 880 g spheres not changing at the same point as the 105 g spheres. The 105 g spheres begin to increase in fractal dimension between 0.03 and 0.035 scaled time. The high frequency 880 g charges begin to increase in fractal dimension at 0.035 scaled time, as do some, but not all, of the smooth and medium frequency perturbations. The 880 g tests where the fractal dimension did increase align broadly with the behavior exhibited by the 105 g charges.

The incomplete scaling seen in Figure 6.8 indicates that the mass scaling exponent of 1/3 may not be the proper exponent to collapse this scaling. A simplified investigation in the scaling exponent relating total explosive energy E_{HE} to

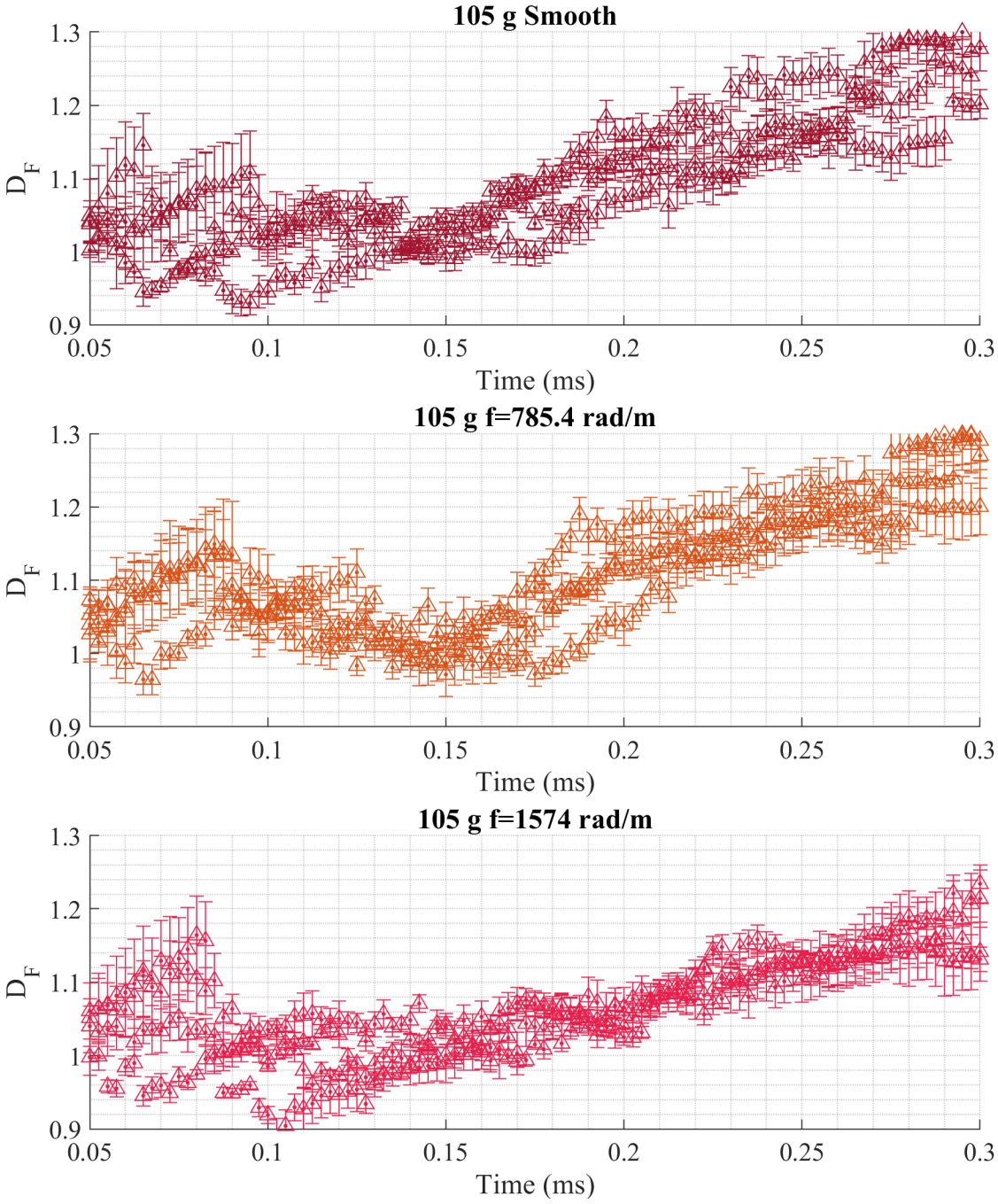

Figure 6.6: The fractal dimension of reported tests broken down by mass and perturbation for the perturbed 105 g C4 spheres.

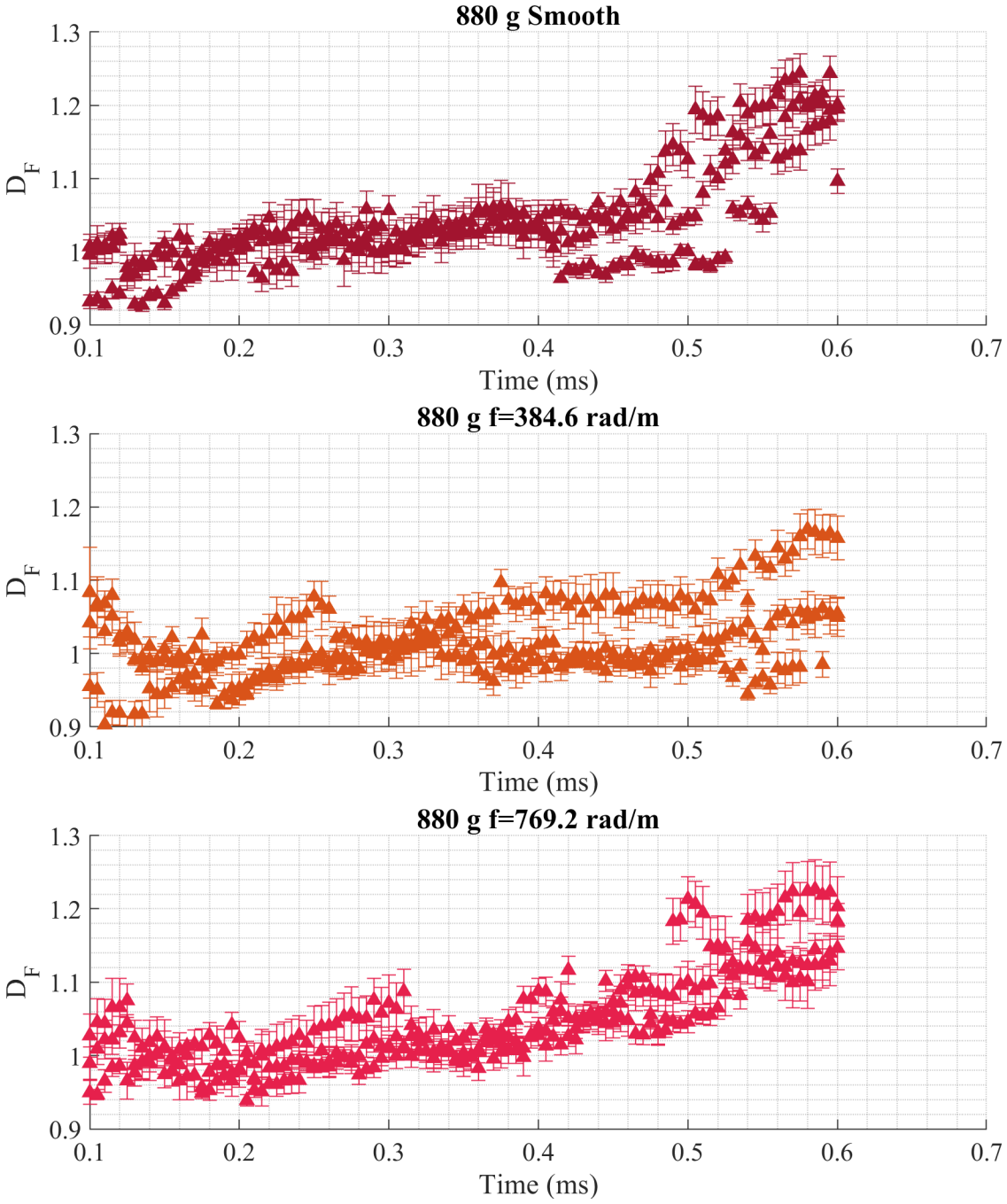

Figure 6.7: The fractal dimension of reported tests broken down by mass and perturbation for the perturbed 880 g C4 spheres.

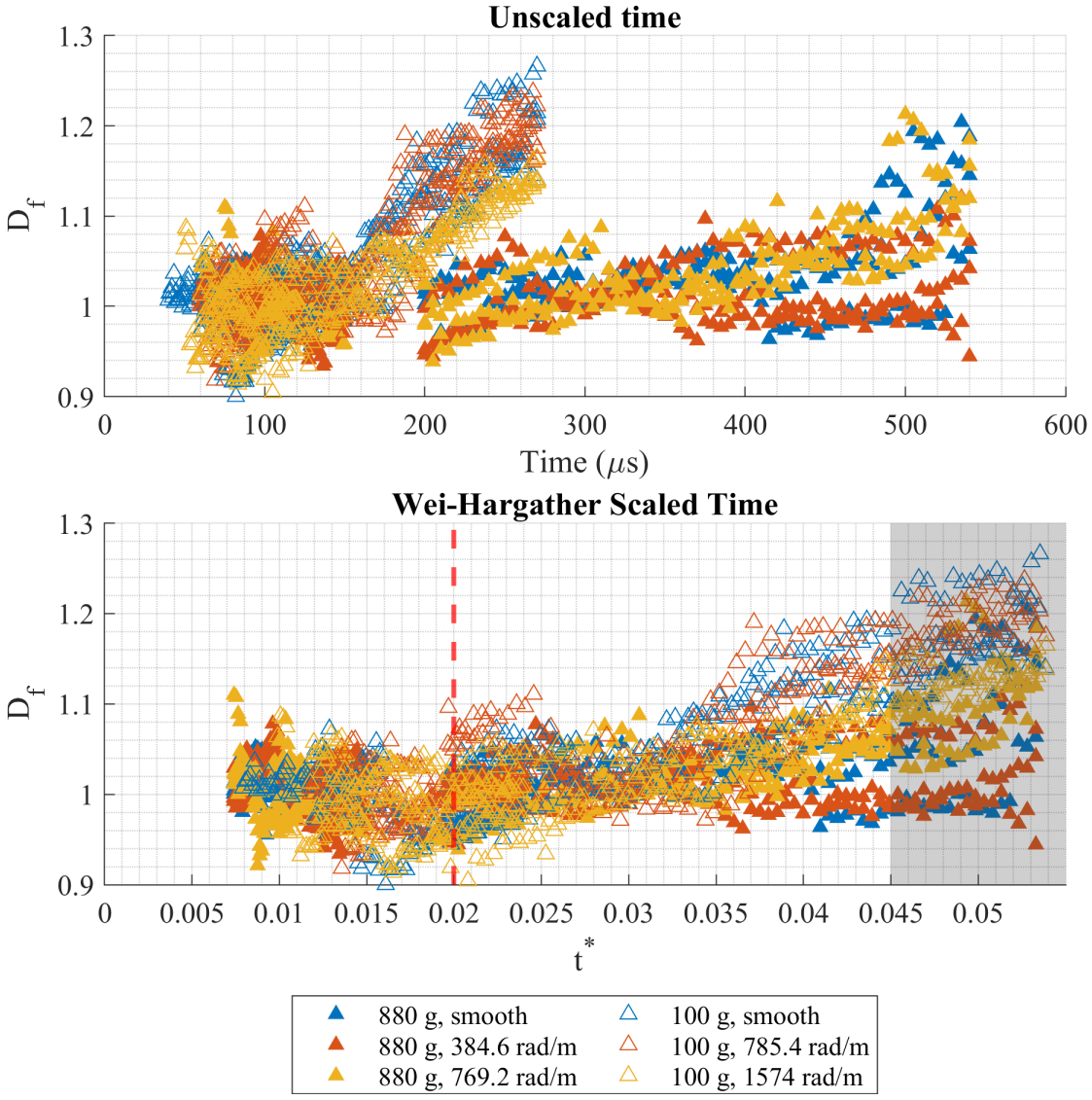

Figure 6.8: When treated with both scalings, the behavior of the 105 g and 880 g charges weakly collapse. The red dashed line indicates the transition from the strong shock to the weak shock regime in Wei-Hargather scaling. The shaded region indicates shock separation from the fireball

the time evolution of the fractal dimension was conducted by dividing the time t by the total energy raised to an arbitrary exponent. Figure 6.9 shows the impact of varying the exponent between 0.35 and 0.5. The mass of the charge is the only variation between the 105 g and 880 g C4 charges, so this minimal description is representative of the impact of varying the scaling on the full scaling. Varying the exponent appears to improve the alignment of both the inflection point and the slope between the two masses. More analysis should be performed to identify the correct exponent, but the value is likely between 0.4 and 0.5. The physical meaning of this exponent is not explored in this work.

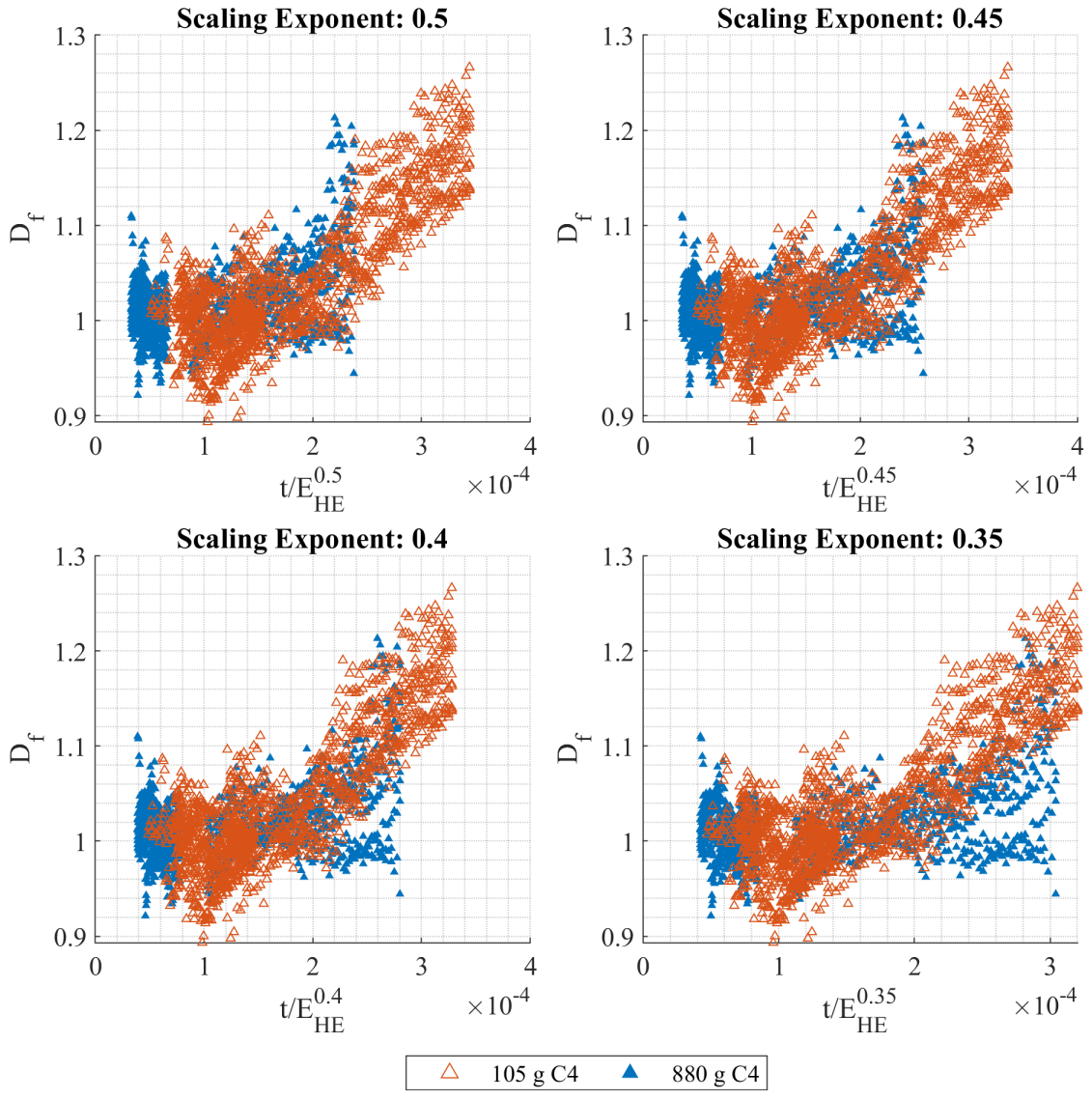

Figure 6.9: Variation the scaling exponent on the explosive energy term between and exponent 0.35 and 0.5.

The addition of the fractal dimension from the PBXN-113 tests reinforces that the fractal dimension of the contour does not scale with shock scaling criteria. Figure 6.10 shows the PBXN-113 tests following a slow but consistent increase in fractal dimension. As will be further discussed in the next section, the fractal dimension is tied to evolution of mixing region decoupling from the primary shock, so scaling with these criteria was not expected.

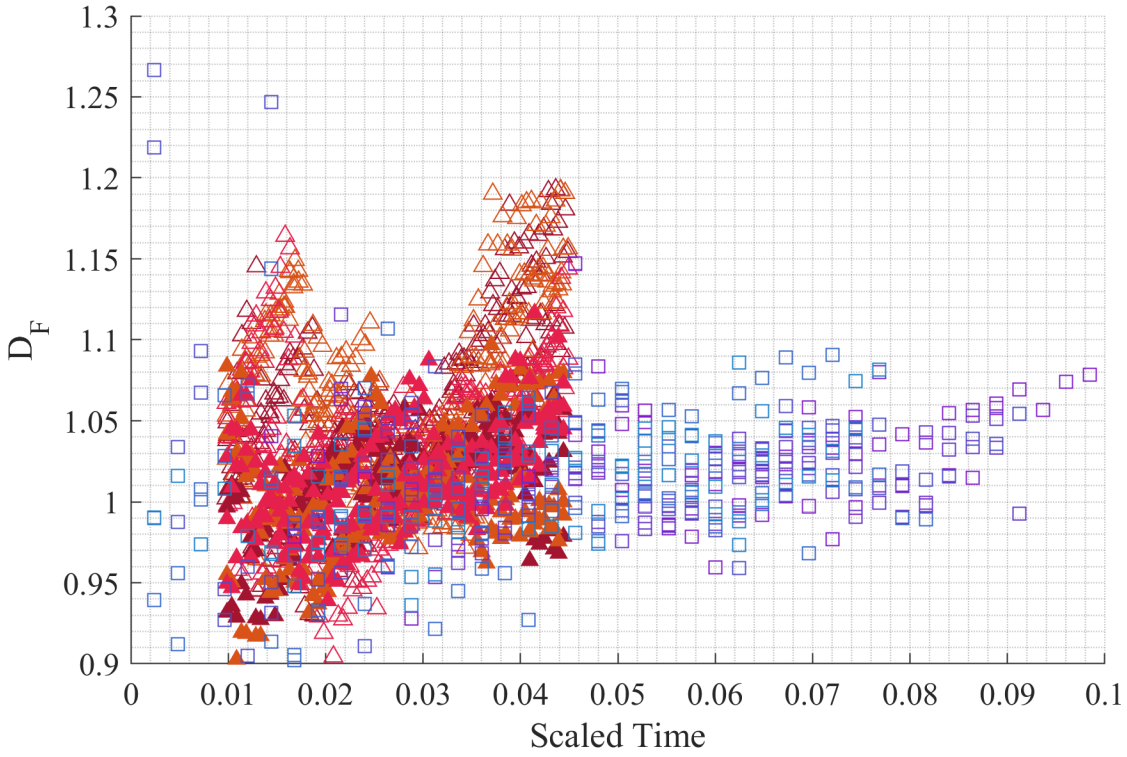

Figure 6.10: The addition of the (blue) PBXN-113 tests to the (red) perturbed sphere test.

6.4 Fractal dimension as a function of mixing width

The scaling of the fractal Hausdorff dimension with standard explosive scaling laws during early time evolution is a step towards understanding how the evolution of the explosively driven product gases mix and combust with the ambient air. The rapid expansion of the detonation products drives both the shock wave formation and the transition to turbulent mixing on the contact surface, so before shock separation from the fireball the two processes linked. The fractal behavior appears to be decoupled from the initial surface perturbations of the charges, as the fractal trends developed at the same rate within error regardless of the charge geometry. Figures 6.11 and 6.12 show the evolution of the fractal

dimension with respect to unscaled mixing region width for the 105 g and 880 g charges, respectively. Uncertainties for the 105 g charge mixing region width are small enough to allow the identification of data trends. Conclusions drawn from the 880 g charges are limited due to the very high uncertainty in the mixing width estimates, but the different tests do appear to be tracking a similar trend to the 105 g charges. When plotted as a function of the normalized mixing width $h^* = h/R_0$, shown in Figure 6.13 for perturbed spheres, the evolution of the fractal dimension is seen to be weakly linearly linked to the evolution of the mixing region width. As the fireball surface transitions from initial rapid expansion towards a regime dominated by surface mixing, the fractal dimension of that surface increases. The increase in fractal dimension is mirrored by a change in the growth rate of the mixing region. The addition of the PBXN-113 data plotted against normalized mixing width in Figure 6.14 reinforces the trend. As the relative width of the mixing region grows, the ratio of contact surface length to circumference also grows, driving an increase in the fractal dimension. The evolution makes sense both geometrically, in terms of the projected outline of an increasingly complex sphere, as well as physically, in terms of the barolinic torque being applied to the greater angle of a the perturbation waves as the relative thickness increases.

The fractal dimension of early time fireball can be consistently measured from multiple viewing angles of the same detonation event. Applying shock scaling criteria to the measured fractal dimension does not cause a collapse between tests with different explosives masses (105 g versus 880 g), or with different explosives (C4 versus PBXN-113). Scaling the fractal dimension by the mean radius normalized mixing width however, showed a noisy but effective collapse.

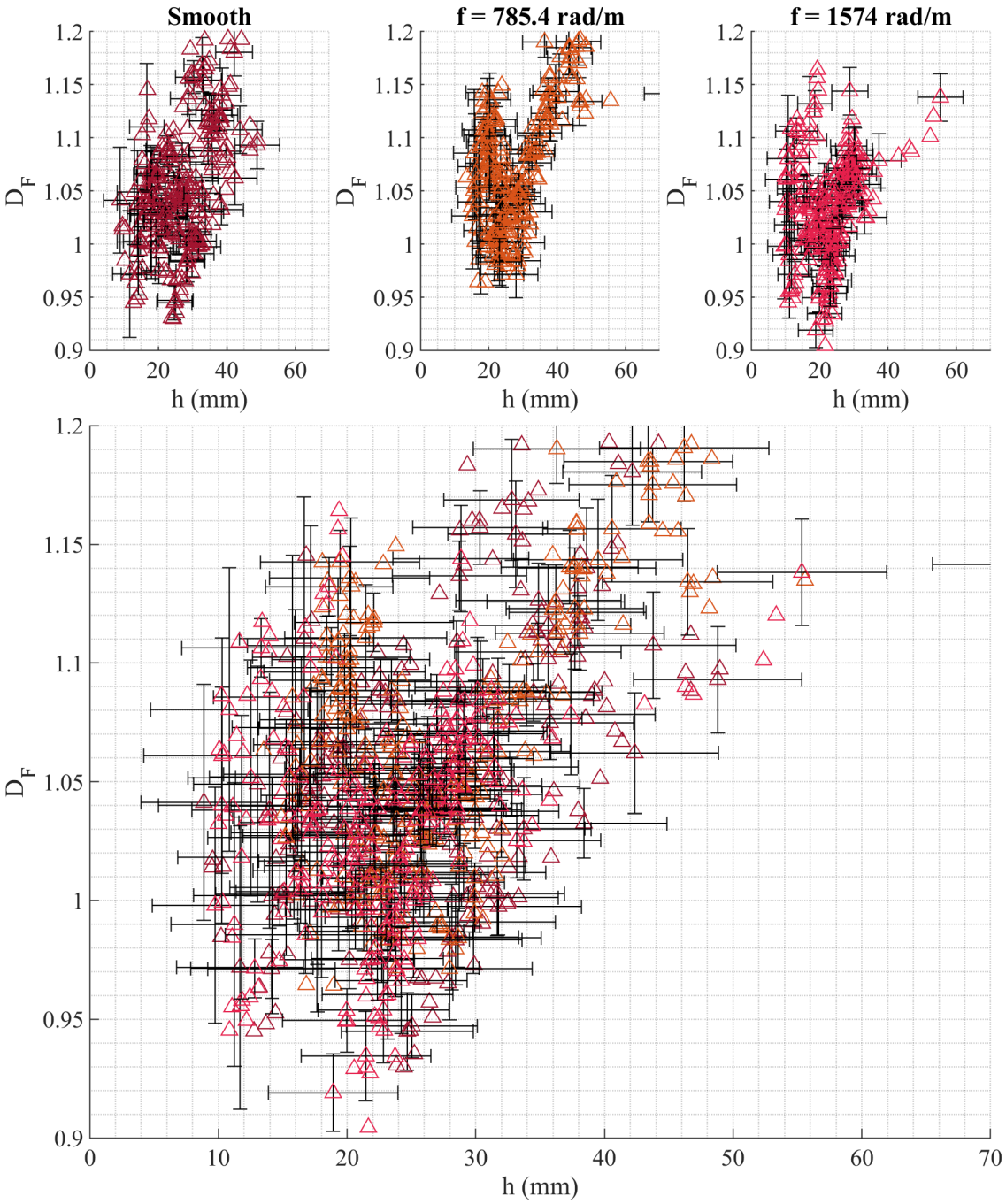

Figure 6.11: The evolution of the fractal dimension for 105 g charges as a function of unscaled mixing region width (top) by perturbation. When (bottom) all perturbations are overlaid, it is evident that the fractal dimension is a function of mixing region width.

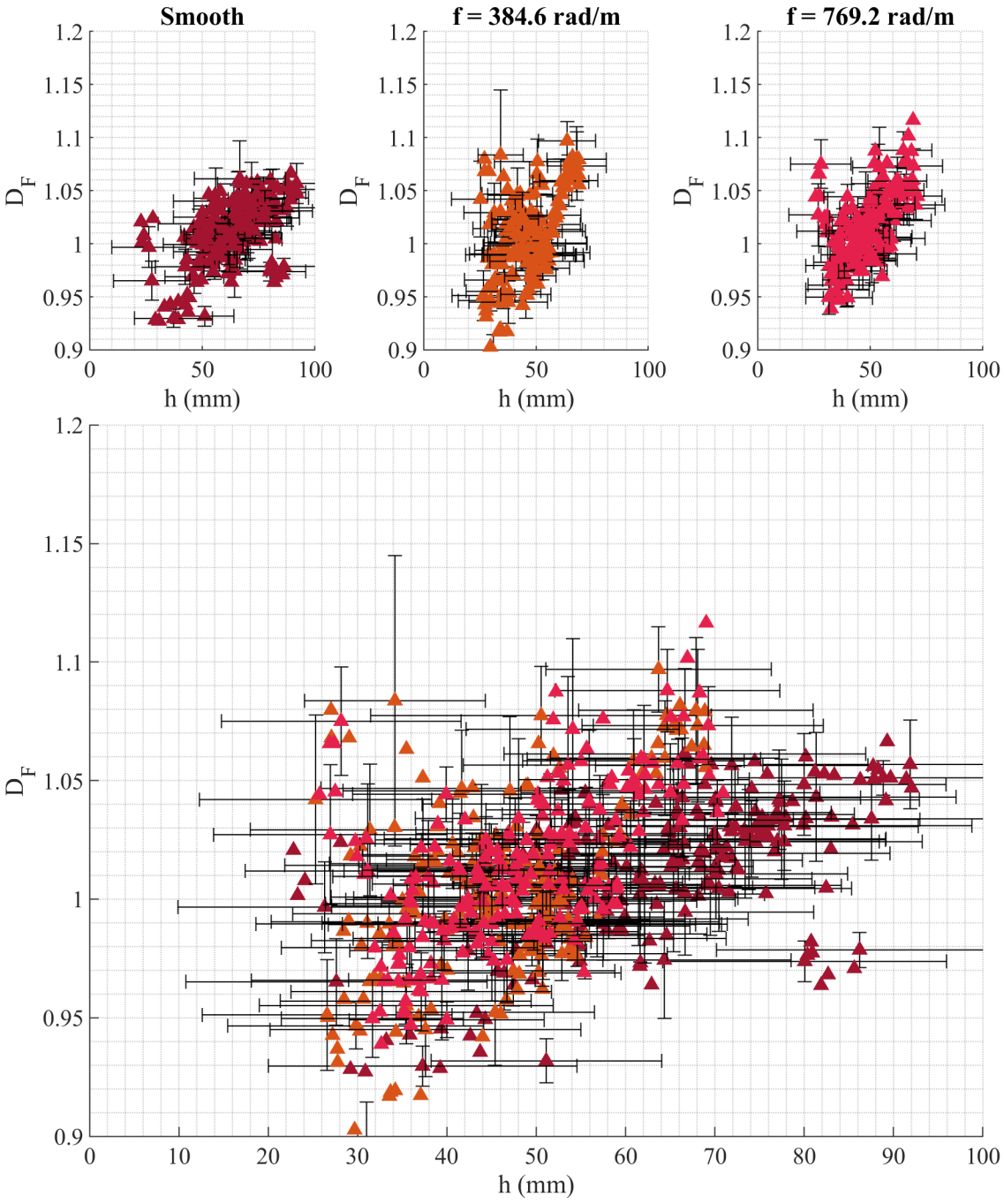

Figure 6.12: The evolution of the fractal dimension for 880 g charges as a function of unscaled mixing region width (top) by perturbation. Overlaying (bottom) all perturbations on the same axes shows a weak trend.

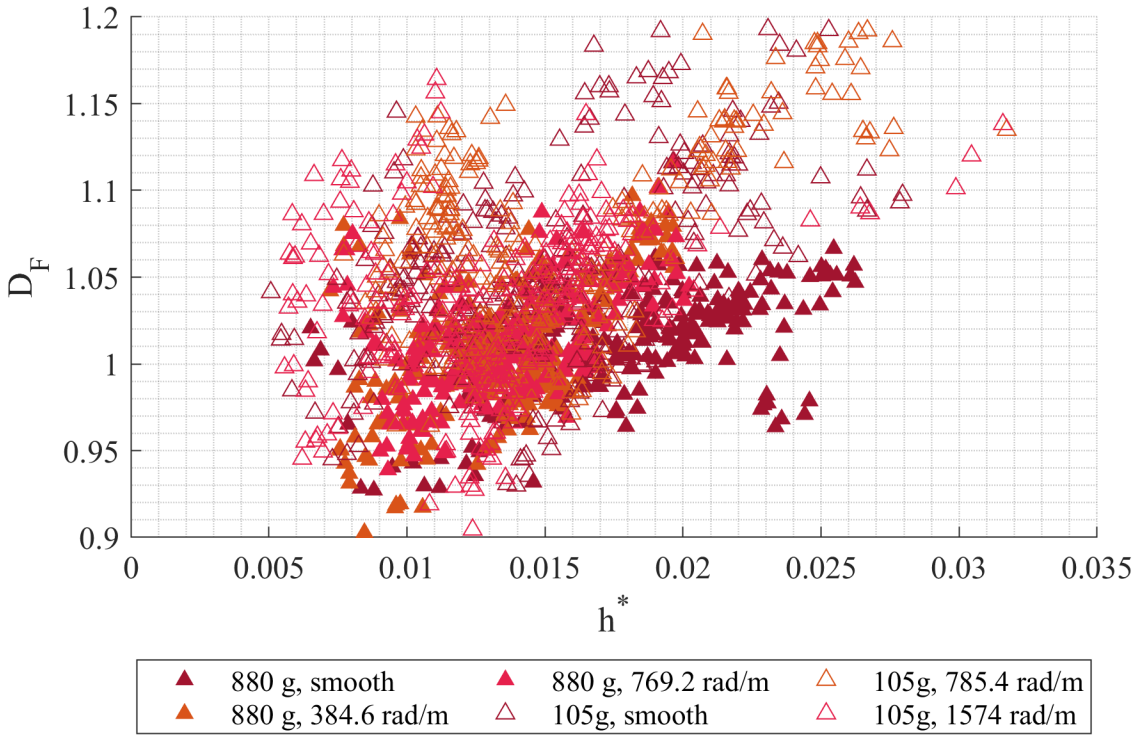

Figure 6.13: The fractal dimension of both smooth and perturbed spheres as a function of the normalized mixing region width.

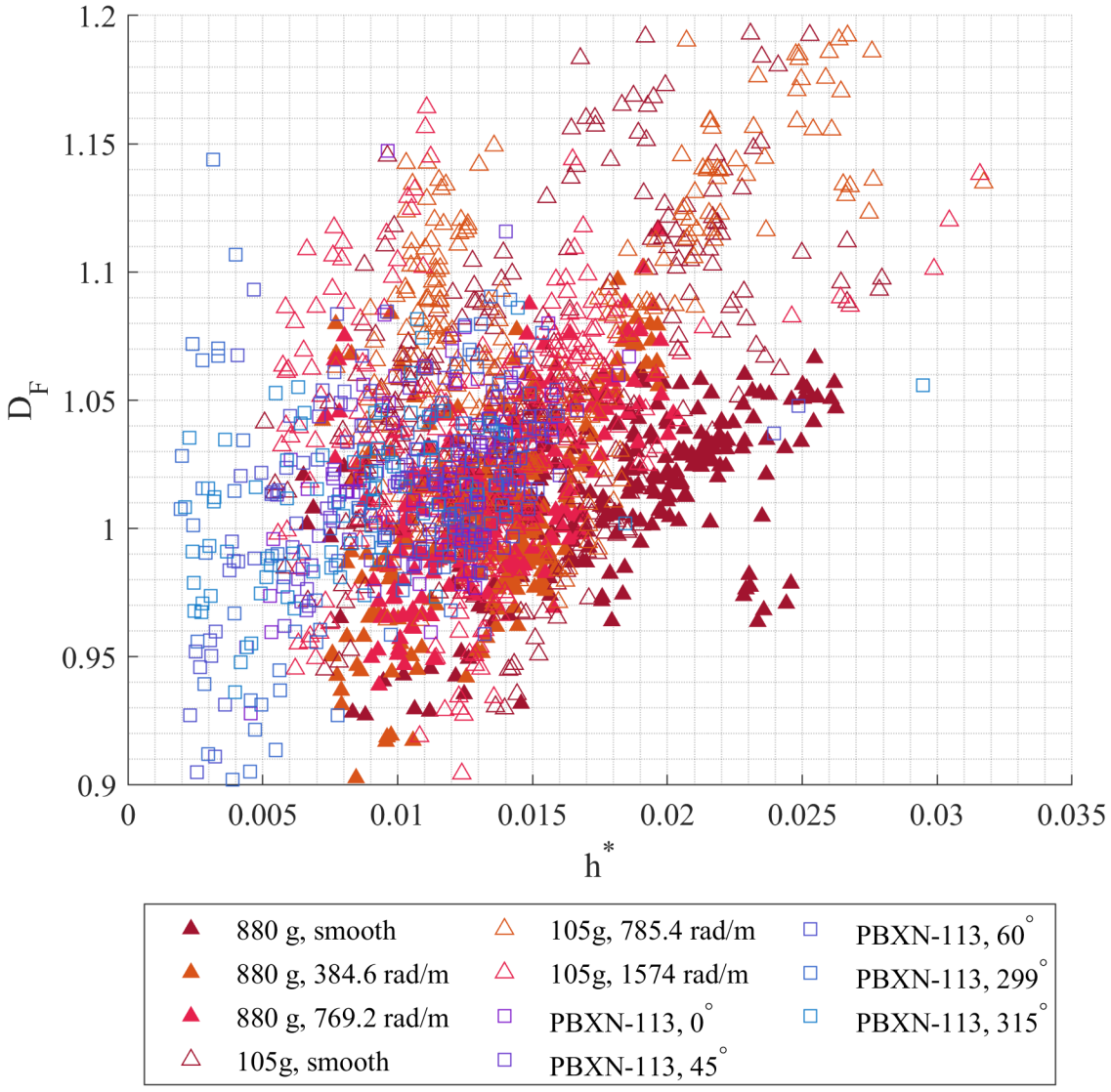

Figure 6.14: The fractal dimension of the (red) perturbed spheres and (blue) PBXN-113 tests.

CHAPTER 7

CONCLUSIONS

The growth and evolution of the interface between detonation products and ambient air was measured for experiments with varying charge mass, explosive formulation, and initial geometry. The explosive charges spanned over three orders of magnitude in mass variation and a factor of two in specific explosive energy variation. The resulting expansion of the detonation gases was found to be repeatable and scalable. Classical perturbation evolution models for the growth of the mixing region, with the addition of an initial growth rate term, were fit to experimental data. The resulting form of the models shows that the Atwood number variation with time and initial growth terms are critical to consider for the early-time expansion across varied experimental setups. The interface contours are ultimately found to have a time-varying fractal dimension, which scales with the mixing region growth, as the surface evolves from a smooth perturbation towards fully-developed turbulence.

7.1 Validity of analytical mixing growth models for real explosives

Explosive charges with initial perturbations ranging from $h_0/\lambda = 0.061$ to $h_0/\lambda = 0.25$ were studied here. These values were chosen because they straddled the standard validity criteria for analytical models of linearized perturbation growth, with smaller perturbations expected to follow the linearized model and larger ones potentially behaving differently. The breakdown of linearized models is associated with the flow transitioning towards turbulent mixing, and is expected to cause a change in the growth rate of the mixing region. The model for growth of a perturbation on a spherical surface was found to capture the behavior of early mixing width results, but not to capture the plateauing of the mixing region width. The values of the geometric constant c for the early times are indicative of the complex transitions in the dominant instabilities on the surface of a fireball, as the over expansion of the detonation products causes an inversion in the relative densities at the contact surface. The fit can be improved by modulating the initial contact surface growth rate using the k term. However, the addition of this term does not improve the predictive capabilities of the model into the weak non-linear regime.

The impact of several treatments of the Atwood number on the model was studied. Modeling the Atwood number as varying with time improved the agreement of the model with the data. Calculating the Atwood number with respect to the density of the air immediately behind the shock wave resulted in underestimation of the mixing width when the model was initialized from pre-detonation conditions, but good agreement was found when initial conditions were taken from early experimental data. The good agreement indicates that the large perturbations are still dominating the evolution of mixing regime. The change in model slope near the end of the data further indicates a change in the length scales driving the mixing evolution towards smaller scales.

The initial perturbation of the explosive charge did not impact the agreement between the analytical model and the measured mixing width. The lack of variation between perturbed and unperturbed mixing regions is in agreement with numerical analyses performed on idealized one dimensional models [31, 32].

7.2 Application of shock scalings to non-shock phenomena

The behavior of the expanding fireball immediately post detonation is closely linked to the formation and behavior of the shock wave. However, the parameters that dominate the expansion and mixing of the fireball are not necessarily the same parameters that govern the shock wave. The initial expansion of the fireball appears to scale reliably with the same scaling criteria as used for shock wave propagation. The limitations of shock scaling become evident as the fireball transitions from momentum based expansion regime to a viscosity dominated mixing regime.

The effectiveness of a shock scaling for describing the evolution of the non-shock phenomena associated with the fireball is dependent on the time scale. In the early evolution of the fireball, it is effectively attached to the shock, and expands at a comparable rate. For the duration of the early linear perturbation growth regime, the fireball is governed by similar parameters as the shock. The initial impulsive acceleration of detonation is determined by explosive energy, and the drag based deceleration is dependent upon atmospheric conditions. Initial density ratios are determined by explosive density and ambient conditions, so the the Atwood number is constant early. Once the fireball has detached from the shock however, bulk fireball behavior still appears to obey shock scaling for turbulent mixing, but the behavior of mixing on the surface of the fireball evolves through mechanisms not scaled by the shock scaling.

The breadth of scaled times covered by this effort is too narrow to draw conclusions about the effectiveness of shock scaling after shock detachment from the fireball. The behavior observed in Figure 4.8 is indicative of potentially asymptotic behavior as the gram scale fireballs stabilized, but without additional fireball data extending out to those scaled times, no definitive conclusion can be drawn.

7.3 The fractal dimension as a metric for mixing growth

The fractal dimension is ultimately representative of the development of structures on the surface of the fireball that are self similar through multiple scales. The connection to turbulence and mixing through the diffusion of flow scalar properties indicates that at a base level, turbulent flows should have fractal properties. A digital image of a fireball identifies a region of high optical density that can be taken to be representative of the boundary between high temperature detonation products and ambient air. The results in Chapter 4 demonstrated that a fireball contour can be extracted that behaves as is expected based on fireball scaling in the literature. The behavior of the mixing region aligns with the behavior of predictive analytical models, leading to the conclusion that the extracted fireball contour is representative of the mixing behavior on the contact surface.

The fractal dimension grows as a function of the mixing width because the area covered by the boundary increases relative to the smooth surface idealization of the fireball determined from its average radius. This relationship will be true until either the scale of newly forming turbulent structures is below the resolving power of the camera, or the development of three-dimensionality on the surface occludes the tracking of the fireball contour. Based on these criteria, the fractal dimension is an enhancement of the mixing width measurement for the flow regime immediately after the linear regime. The initially smooth surface of the fireball results in a fractal dimension near unity primarily driven by an increase in h. As mixing width growth rate transitions away from the exponential growth of the linear models, the non-linearities of the flow cause an increase in contact surface complexity, which corresponds to an increase in contact surface length in the same projected area. This increase in length per area translates to an increased fractal dimension. The optimal application for the direct imaging fractal diagnostic is this early transition time. Because the measurement of the fractal dimension is an imaging based diagnostic that does not place requirements on the experimental configuration, it can be calculated for archival test data to identify changes in the mixing regime on the fireball surface. Higher imaging resolution can improve the quality and capacity of this measurement up to a point, but there is an upper limit to effective application time.

The lower bound is related to the transition away from the linear perturbation growth regime, as identified by analytical model effectiveness. The analytical models for mixing region growth are ultimately assuming that the fireball surface can be accurately described using a spherical harmonic Y_n, and that the growth of the harmonic amplitude η accurately describes the growth of the mixing region as a whole. These models are therefore more effective when describing a flow with a smooth contact surface well described by the spherical harmonics. Once these models break down, the previously discussed increased complexity of the contact surface lends itself to being described by a fractal. This is a useful distinction for visual characterization of a fireballs evolution, and is a principal result of this work. The flow characteristics that contribute to a mixing region becoming non-linear and turbulent also contribute to the increase in the fractal dimension.

Therefore, a marked change in the fractal dimension of a flow may be used as an indicator that a linear analytical model will no longer be appropriate.

The upper bound for application time is driven by the size of initial perturbations on the surface of the explosive, the presence of symmetry in the initial charge, and the orientation of any symmetry features relative to the diagnostic camera. In future work, a rigorous exploration of this upper bound may be conducted using simulations to track fireball isosurfaces and identify when occlusion becomes a substantial contributor to the estimated fireball contour.

The fractal dimension calculated from extracted fireball contours shows that the early time fireball is largely non-fractal. The rapid expansion rate and initial dominance of the gas cloud momentum result in a relatively smooth fireball surface. As the fireball slows, viscous affects accentuate the differences in velocity on the surface to drive the formation of turbulent structures that are visible on the scale of a digital image. This increases the width of the mixing region while simultaneously increasing the number of length scales which exist on the fireball surface, increasing the fractal dimension of the fireball contour. At a certain point, the complexity of the surface causes the projection of the surface seen by a camera to no longer be representative of the boundary between the detonation products and the ambient air. Once this point is reached the fractal dimension of the contour becomes disconnected from the fluid mechanics of the fireball.

7.4 Future work

A first next step would be the establishment of a relationship between the mass of the explosive charge, pixel resolution of the recording camera, and expected fractal offset. As was seen with applying the box counting methodology to known fractals, the method tends to systematically over or under predict the fractal dimension. This is resolvable for mathematically defined fractals, but connecting the characteristics of a given data set to the expected fractal offset would enhance the precision of the diagnostic.

The characterization of the fractal dimension evolution has relied on direct imaging to extract fireball contours from experimental data. An exploration into the upper bound of the validity range could be done with computational studies on the evolution of specific isosurfaces of temperature or concentration in a fireball. Similarly, the lower bound of camera resolution could be more effectively explored through simulated cameras on a repeatable surface. Simulation efforts would also enable refinement of assumptions built into the analytical models such as evenly expanding density gradient.

A second, parallel thrust could be the development of more robust experimental techniques for the extraction of a mixing width in a full blast environment. Experiments with hemispherical explosive charges detonated above a transparent surface, similar to the variable gas confinement experiments conducted for

this work, could provide experimental validation to the computational identification of more rigorously defined isosurfaces. Surface registration and tomographic techniques, while eventually excluded from the present effort, remain a potential tool for removing the requirement for the assumptions of dimensional symmetry for utilizing the two-dimensional contour slices of the full surfaces.

Further refinement of the testing methodology used to generate the perturbed C4 spheres will allow a deeper exploration of the real effects of repeatable surface perturbations on the evolution of fireball mixing. Machined molds would increase the available resolution for the forming processing, allowing the creation of smaller and higher fidelity perturbations. Additionally, perturbations without an axis of rotational symmetry were not explored in the current effort and would provide additional insight into how the early time surface growth is related to the late time mixing on the surface.

REFERENCES

[1] Lewis Fry Richardson and Peter Lynch. *Weather Prediction by Numerical Process*. Cambridge University Press, 1922.

[2] Francois G. Schmitt. Turbulence from 1870 to 1920: The birth of a noun and of a concept. *Comptes Rendus Mécanique*, 345(9):620–626, 2017.

[3] François G. Schmitt. About Boussinesq's turbulent viscosity hypothesis: historical remarks and a direct evaluation of its validity. *Comptes Rendus Mécanique*, 335(9-10):617–627, 2007.

[4] U. Frisch and A. N. Kolmogorov. *Turbulence: The Legacy of A. N. Kolmogorov*. Cambridge University Press, 1995.

[5] J. von Neumann. Physical applications of the ergodic hypothesis. *Proceedings of the National Academy of Sciences*, 18(3):263–266, 1932.

[6] George I. Bell. Taylor instability on cylinders and spheres in the small amplitude approximation. Technical Report LA-1321, Los Alamos Scientific Laboratory of the University of California, 1951.

[7] A. M. Binnie. The stability of the surface of a cavitation bubble. *Mathematical Proceedings of the Cambridge Philosophical Society*, 49(1):151–155, 1953.

[8] Karnig Mikaelian. Rayleigh-Taylor and Richtmyer-Meshkov instabilites and mixing in stratified spherical shells. *Physical Review A*, 42(6):3400–3420, 1990.

[9] Karnig O. Mikaelian. Rayleigh-Taylor and Richtmyer-Meshkov instabilities and mixing in stratified cylindrical shells. *Physics of Fluids*, 17, 2004.

[10] M. S. Plesset. On the Stability of Fluid Flows with Spherical Symmetry. *Journal of Applied Physics*, 25(1):96–98, jan 1954.

[11] John William Strutt. Investigation of the character of the equilibrium of an incompressible heavy fluid of variable density. In *Scientific Papers*, pages 200–207. Cambridge University Press, 1883.

[12] Robert D. Richtmyer. Taylor instability in shock acceleration of compressible fluids. *Communications on Pure and Applied Mathematics*, 13(2):297–319, 1960.

[13] P. R. Chapman and J. W. Jacobs. Experiments on the three-dimensional incompressible Richtmyer-Meshkov instability. *Physics of Fluids*, 18(7):1–12, 2006.

[14] Ye Zhou. Rayleigh–Taylor and Richtmyer–Meshkov instability induced flow, turbulence, and mixing. i. *Physics Reports*, 720–722:1–136, 2017.

[15] Garrett Birkhoff. Note on Taylor instability. *Quarterly of Applied Mathematics*, 12:306–309, 1954.

[16] G. I. Taylor. The instability of liquid surfaces when accelerated in a direction perpendicular to their planes. I. *Proceedings of the Royal Society of London. Series A. Mathematical and Physical Sciences*, 201(1065):192–196, 1950.

[17] M. Lombardini and D. I. Pullin. Small-amplitude perturbations in the three-dimensional cylindrical Richtmyer–Meshkov instability. *Physics of Fluids*, 21(11):114103, 2009.

[18] J. Kane, R. P. Drake, and B. A. Remington. An evaluation of the Richtmyer-Meshkov instability in supernova remnant formation. *The Astrophysical Journal*, 511(1):335–340, 1999.

[19] Kane J., Arnett D., Remington B. A., Glendinning S. G., Bazan G., Muller E., Fryxell B. A., and Teyssier R. Two-dimensional versus three-dimensional supernova hydrodynamic instability growth. *The Astrophysical Journal*, 528(2):989–994, 2000.

[20] Snezhana I. Abarzhi, Aklant K. Bhowmick, Annie Naveh, Arun Pandian, Nora C. Swisher, Robert F. Stellingwerf, and W. David Arnett. Supernova, nuclear synthesis, fluid instabilities, and interfacial mixing. *Proceedings of the National Academy of Sciences*, 116(37):18184–18192, 2018.

[21] E. E. Meshkov. Instability of the interface of two gases accelerated by a shock wave. *Fluid Dynamics*, 4(5):101–104, 1972.

[22] Harold L. Brode. Blast wave from a spherical charge. *Physics of Fluids*, 2(2):217–229, 1959.

[23] K. A. Meyer and P. J. Blewett. Numerical investigation of the stability of a shock-accelerated interface between two fluids. *Physics of Fluids*, 15(5):753–759, 1972.

[24] Martin Brouillette. The Richtmyer-Meshkov Instability. *Annual Review Fluid Mechanics*, 2002.

[25] Paul C. Duffel. A one-dimensional model for Rayleigh-Taylor instability in supernova remnants. *The Astrophysical Journal*, 821(2):76, 2016.

[26] Richard L. Holmes, Guy Dimonte, Bruce Fryxell, Michail L. Gittings, David H. Sharp, Alexander L. Velikovich, Rober P. Weaver, and Qiang Zhang. Richtmyer-Meshkov instability growth: experiment, simulation, and theory. *Journal of Fluid Mechanics*, 389, 1999.

[27] O. E. Ivashnev. Mechanism of the Richtmyer-Meshkov instability. *Fluid Dynamics*, 46(4):514–524, 2011.

[28] Marco Latini, Oleg Schilling, and Wai Sun Don. Effects of WENO flux reconstruction order and spatial resolution on reshocked two-dimensional Richtmyer–Meshkov instability. *Journal of Computational Physics*, 221(2):805–836, 2007.

[29] Raaghav Ramani and Steve Shkoller. A multiscale model for Rayleigh-Taylor and Richtmyer-Meshkov instabilities. *Journal of Computational Physics*, 405:109177, 2020.

[30] G. A. Ruev, A. V. Fedorov, and V. M. Fomin. Development of and the Richtmyer-Meshkov Instability during interaction of the diffusion mixing layer of two gases with transient and reflected shock waves. *Journal of Applied Mechanics and Technical Physics*, 51(3):308–316, 2010.

[31] Mina R. Mankbadi and S. Balachandar. Compressible inviscid instability of rapidly expanding spherical material interfaces. *Physics of Fluids*, 24(3), 2012.

[32] M. R. Mankbadi and S. Balachandar. Viscous effects on the non-classical Rayleigh–Taylor instability of spherical material interfaces. *Shock Waves*, 23(6):603–617, 2013.

[33] D. Souffland, O. Grégoire, S. Gauthier, and R. Schiestel. A two-time-scale model for turbulent mixing flow induced by Rayleigh-Taylor and Richtmyer-Meshkov instabilities. *Flow, Turbulence and Combustion*, 69(2):123–160, 2002.

[34] Allen Kuhl, David Grote, and John Bell. Scaling turbulent combustion fields in explosions. *Applied Sciences*, 10(23):8577, 2020.

[35] Peter Vorobieff, Paul M. Rightley, and Robert F. Benjamin. Shock-driven gas curtain: fractal dimension evolution in transition to turbulence. *Physica D*, 1999.

[36] Ye Zhou, Robin J.R. Williams, Praveen Ramaprabhu, Michael Groom, Ben Thornber, Andrew Hillier, Wouter Mostert, Bertrand Rollin, S. Balachandar, Phillip D. Powell, Alex Mahalov, and N. Attal. Rayleigh–Taylor and Richtmyer–Meshkov instabilities: A journey through scales. *Physica D: Nonlinear Phenomena*, 423:132838, 2021.

[37] S. Courtiaud, N. Lecysyn, G. Damamme, T. Poinsot, and L. Selle. Analysis of mixing in high-explosive fireballs using small-scale pressurised spheres. *Shock Waves*, 29(2):339–353, February 2018.

[38] Samuel J. Grauer, Andreas Unterberger, Andreas Rittler, Kyle J. Daun, Andreas M. Kempf, and Khadijeh Mohri. Instantaneous 3D flame imaging by background-oriented schlieren tomography. *Combustion and Flame*, 196:284–299, 2018.

[39] K. R. Sreenivasan and R. A. Antonia. The phenomenology of small-scale turbulence. *Annual Review of Fluid Mechanics*, 29:435–472, 1997.

[40] Haris J. Catrakis and Paul E. Dimotakis. Mixing in turbulent jets: scalar measures and isosurface geometry. *Journal of Fluid Mechanics*, 317:369–406, 1996.

[41] Kenji Mukaiyama, Shimon Shibayama, and Kazunori Kuwana. Fractal structures of hydrodynamically unstable and diffusive-thermally unstable flames. *Combustion and Flame*, 160(11):2471–2475, 2013.

[42] Benoit B. Mandelbrot. *The fractal geometry of nature*. Freeman, San Francisco, CA, 1982.

[43] A. Bancaud, C. Lavelle, S. Huet, and J. Ellenberg. A fractal model for nuclear organization: current evidence and biological implications. *Nucleic Acids Research*, 40(18):8783–8792, 2012.

[44] A. Rinaldo, I. Rodriguez-Iturbe, R. Rigon, E. Ijjasz-Vasquez, and R. L. Bras. Self-organized fractal river networks. *Physical Review Letters*, 70(6):822–825, 1993.

[45] Javier Rodriguez, Leonardo Juan Ramírez López, and Gabriel Alberto Puerta Aponte. Analysis of acute heart dynamics in intensive care unit based on dynamic systems. *Informatics in Medicine Unlocked*, 19:100333, 2020.

[46] H. G. E. Hentschel and Itamar Procaccia. The infinite number of generalized dimensions of fractals and strange attractors. *Physica D: Nonlinear Phenomena*, 8(3):435–444, 1983.

[47] James Theiler. Estimating fractal dimension. *Journal of the Optical Society of America A*, 7(6):1055–1072, 1990.

[48] K. J. Falconer. *Fractal geometry: mathematical foundations and applications*. John Wiley & Sons, third edition edition, 2014.

[49] Nirupam Sarkar and B. B. Chaudhuri. An efficient differential box-counting approach to compute fractal dimension of image. *IEEE Transactions on Systems, Man, and Cybernetics*, 24(1):115–119, 1994.

[50] K. Foroutan-pour, P. Dutilleul, and D. L. Smith. Advances in the implementation of the box-counting method of fractal dimension estimation. *Applied Mathematics and Computation*, 105(2-3):195–210, 1999.

[51] K. R. Sreenivasan. Fractals in fluid mechanics. *Fractals*, 02(02):253–263, 1994.

[52] K. R. Sreenivasan. Fractals and multifractals in fluid turbulence. *Annual Review Fluid Mechanics*, 23:539–600, 1991.

[53] Hoi Dick Ng, Hamid Ait Abderrahmane, Kevin R. Bates, and Nikos Nikiforakis. The growth of fractal dimension of an interface evolution from the interaction of a shock wave with a rectangular block of SF6. *Communications in Nonlinear Science and Numerical Simulation*, 16(11):4158–4162, 2011.

[54] Mateo Gomez, Daniel K. Lauriola, Mikhail N. Slipchenko, Sukesh Roy, Steven F. Son, and Terrence R. Meyer. Spatiotemporally resolved 5-MHz visualization and particle image velocimetry in early time multiphase blasts. *Optics and Lasers in Engineering*, 161:107351, 2023.

[55] Hiroki Suzuki, Shinsuke Mochizuki, Yasuhiko Sakai, and Koji Nagata. Analysis and application of decaying turbulence with initial fractal geometry. *Intech Open*, 11:267–283, 2017.

[56] K. R. Sreenivasan and C. Meneveau. The fractal facets of turbulence. *Journal of Fluid Mechanics*, 173:357–386, 1986.

[57] Amitesh Roy and Raman I Sujith. Fractal dimension of premixed flames in intermittent turbulence. *Combustion and Flame*, 226:412–418, 2021.

[58] M. Bambauer, N. Chakraborty, M. Klein, and J. Hasslberger. Vortex dynamics and fractal structures in reactive and nonreactive Richtmyer–Meshkov instability. *Physics of Fluids*, 33(4):044114, 2021.

[59] V. Rodriguez, R. Saurel, G. Jourdan, and L. Houas. Impulsive dispersion of a granular layer by a weak blast wave. *Shock Waves*, 27(2):187–198, 2016.

[60] F. Ouellet, B. Rollin, R. B. Koneru, J. Garno, and S. Balachandar. Effects of perturbing the particle volume fraction distribution in blast-driven multiphase instability. *Shock Waves*, 31(4):337–360, 2021.

[61] H. Schardin. Die schlierenverfahren und ihre anwendungen. *Ergebnisse der Exakten Naturwissenschaften*, 20:303–439, 1942. Translated as NASA TT F-12731.

[62] J. H. Gladstone. XIV. researches on the refraction, dispersion, and sensitiveness of liquids. *Philosophical Transactions of the Royal Society of London*, 153:317–343, 1863.

[63] Gary S. Settles and Michael J. Hargather. A review of recent developments in schlieren and shadowgraph techniques. *Measurement Science and Technology*, 28(4):1–25, 2017.

[64] Frank Austin Mier and Michael J. Hargather. Color gradient background-oriented schlieren imaging. *Experiments in Fluids*, 57(6):1–14, 2016.

[65] Rory P. Bigger. Chemical vapor plume detection using the schlieren optical method. Master's thesis, Pennsylvania State University, 2008.

[66] G.S. Settles. *Schlieren and Shadowgraph Techniques: Visualizing Phenomena in Transparent Media*. Experimental Fluid Mechanics. Springer-Verlag Berlin Heidelberg, 1 edition, 2001.

[67] M. J. Hargather and G. S. Settles. A comparison of three quantitative schlieren techniques. *Optics and Lasers in Engineering*, 50:8–17, 2012.

[68] V. Dvořák. Ueber eine neue einfache art der schlierenbeobachtung. *Annalen der Physik und Chemie*, 245(3):502–511, 1880.

[69] M. J. Hargather and G. S. Settles. Retroreflective shadowgraph technique for large-scale visualization. *Applied Optics*, 48:4449–4457, 2009.

[70] James T. Heineck, Daniel W. Banks, Nathanial T. Smith, Edward T. Schairer, Paul S. Bean, and Troy Robillos. Background-Oriented Schlieren Imaging of Supersonic Aircraft in Flight. *AIAA Journal*, 59(1):11–21, 2021.

[71] Markus Raffel. Background-oriented schlieren (BOS) techniques. *Experiments in Fluids*, 56(3):1–17, 2015.

[72] John Canny. A computational approach to edge detection. *IEEE Transactions on Pattern Analysis and Machine Intelligence*, 8(6):679–698, 1986.

[73] The MathWorks Inc. Image processing toolbox version: 23.2.

[74] Irina Znamenskaya and Igor Doroschchenko. Edge detection and machine learning for automatic flow structures detection and tracking on schlieren and shadowgraph images. *Journal of Flow Visualization and Image Processing*, 28(4):1–26, 2021.

[75] S. E. Rigby, R. Knighton, S. D. Clarke, and A. Tyas. Reflected Near-field Blast Pressure Measurements Using High Speed Video. *Experimental Mechanics*, 60:875–888, 2020.

[76] Yuanhao Gong and Ivo F. Sbalzarini. Curvature Filters Efficiently Reduce Certain Variational Energies. *IEEE Transactions on Image Processing*, 26(4):1786–1798, 2017.

[77] Maurizio Lazzaro. Characterization of the liquid phase of vaporizing GDI sprays from Schlieren imaging. *Measurement Science and Technology*, 30(8):1–15, 2019.

[78] Michael R. Blanton, Eyal Kazin, Demitri Muna, Benjamin A. Weaver, and Adrian Price-Whelan. Improved background subtraction for the Sloan Digital Sky Survey Images. *The Astronomical Journal*, 142(1):31, 2011.

[79] J. M. Gordon, K. C. Gross, and G. P. Perram. Fireball and shock wave dynamics in the detonation of aluminized novel munitions. *Combustion, Explosion, and Shock Waves*, 49(4):450–462, 2013.

[80] Rafael C. Gonzalez. *Digital image processing*. Prentice Hall, 2008.

[81] Liangquan Wang, Fei Shang, and Deren Kong. An image processing method for an explosion field fireball based on edge recursion. *Measurement Science and Technology*, 33(9):095021, 2022.

[82] Robert C. Slaughter, Tyler R. Peery, and John W. McClory. Two-dimensional temperature analysis of nuclear fireballs using digitized film. *Journal of Applied Remote Sensing*, 9:1–11, 2015.

[83] Harold L. Brode. Fireball phenomenology. Technical Report P-3026, The RAND Corporation, 1964.

[84] Kevin C. Gross and Glen P. Perram. The phenomenology of high explosive fireballs from fielded spectroscopic and imaging sensors for event classification. *International Journal of High Speed Electronics and Systems*, 18(01):19–29, 2008.

[85] Jennifer Mott Peuker, Patrick Lynch, Herman Krier, and Nick Glumac. Optical depth measurements of fireballs from aluminized high explosives. *Optics and Lasers in Engineering*, 47(9):1009–1015, 2009.

[86] W. K. Lewis, C. G. Rumchik, and M. J. Smith. Emission spectroscopy of the interior of optically dense post-detonation fireballs. *Journal of Applied Physics*, 113(2):1–4, 2013.

[87] Robert C. Slaughter. *Multidimensional analysis of nuclear detonations*. PhD thesis, Air Force Institute of Technology, 2015.

[88] A. L. Kuhl, J. B. Bell, V. E. Beckner, K. Balakrishnan, and A. J. Aspden. Spherical combustion clouds in explosions. *Shock Waves*, 23(3):233–249, 2012.

[89] Ashley J. Saltzman, Alex D. Brown, Kevin Wan, Julien L. Manin, Lyle M. Pickett, Marc C. Welliver, and Daniel R. Guildenbecher. Extinction Imaging Diagnostics for In Situ Quantification of Soot within Explosively Generated Fireballs. *Propellants, Explosives, Pyrotechnics*, 48:1–15, 2023.

[90] Grigory Isaakovich Barenblatt. *Scaling*. Cambridge University Press, 2003.

[91] Grigory Isaakovich Barenblatt. *Scaling, Self-similarity, and Intermediate Asymptotics*. Cambridge University Press, 1996.

[92] E. Buckingham. On physically similar systems: Illustrations of the use of dimensional equations. *Physical Review*, 4(4):345–376, 1914.

[93] Geoffrey Ingram Taylor. The formation of a blast wave by a very intense explosion I. Theoretical discussion. *Proceedings of the Royal Society of London. Series A. Mathematical and Physical Sciences*, 201(1065):159–174, 1950.

[94] Robert Green Sachs. The dependence of blast on ambient pressure and temperature. Technical report, Army Ballistic Research Lab, 1944.

[95] G. F. Kinney and K. J. Graham. *Explosive shocks in air*. Springer-Verlag, 1985.

[96] T. Wei and M. J. Hargather. A new blast wave scaling. *Shock Waves*, 31(3):231–238, 2021.

[97] S. Glasstone and P. J. Dolan. *The Effects of Nuclear Weapons. Third edition*. United States Department of Defense, 1977.

[98] Jacob A. McFarland, Jeffrey A. Greenough, and Devesh Ranjan. Computational parametric study of a Richtmyer-Meshkov instability for an inclined interface. *Physical Review E*, 84(2):026303, 2011.

[99] M. Lombardini and D. I. Pullin. Startup process in the Richtmyer–Meshkov instability. *Physics of Fluids*, 21(4):1–13, 2009.

[100] Dell Olmstead, Patrick Wayne, Jae-Hwun Yoo, Sanjay Kumar, C. Randall Truman, and Peter Vorobieff. Experimental study of shock-accelerated inclined heavy gas cylinder. *Experiments in Fluids*, 58(6):1–20, 2017.

[101] Christian Peterson, Veronica Espinoza, and Michael Hargather. Experimental evolution of explosively driven gas clouds in varying confinement. *Experiments in Fluids*, 63(12):1–11, 2022.

[102] Kyle Winter. *Irregular reflections of unsteady shock waves*. PhD thesis, New Mexico Institute of Mining and Technology, 2021.

[103] T. C. McGregor and K. A. Clark. Qualification testing for PBXN-113 containing reclaimed HMX. In *2006 NDIA-IMEMG Instensitive Munitions & Energetic Materials Technology Symposium*, 2006.

[104] B. M. Dobratz. LLNL explosives handbook: properties of chemical explosives and explosives and explosive simulants. Technical Report UCRL-52997, Office of Scientific and Technical Information, 1981.

[105] Teledyne-RISI. RISI catalog, 2022.

[106] Qioptiq Photonics GmbH. WinLens3D.

[107] Sivana M. Torres, Maria N. D'Orazio, and Michael J. Hargather. Focus enhancement in long schlieren imaging systems using corrector lenses. *Applied Optics*, 62(29):7744, 2023.

[108] Philip J. Rae and John M. McAfee. The blast parameters spanning the fireball from large hemispherical detonations of c-4. *Propellants, Explosives, Pyrotechnics*, 43(7):694–702, 2018.

[109] T. Mizukaki, K. Wakabayashi, T. Matsumura, and K. Nakayama. Background-oriented schlieren with natural background for quantitative visualization of open-air explosions. *Shock Waves*, 24(1):69–78, 2013.

[110] Michael John Hargather and Gary S. Settles. Natural-background-oriented schlieren imaging. *Experiments in Fluids*, 48(1):59–68, 2009.

[111] William H. Cabot and Andrew W. Cook. Reynolds number effects on Rayleigh–Taylor instability with possible implications for type -1a supernovae. *Nature Physics*, 2(8):562–568, 2006.

[112] John R. Taylor. *An introduction to error analysis*. University Science Books, 2. ed. edition, 1997.

[113] Philip R. Bevington and D. Keith Robinson. *Data reduction and error analysis for the physical sciences*. McGraw-Hill, 3. ed. edition, 2003.

[114] A. J. Eggers. One-dimensional flows of an imperfect diatomic gas. Technical Report 959, National Advisory Committee for Aeronautics, 1948.

[115] J. P. Wilkinson and J. W. Jacobs. Experimental study of the single-mode three-dimensional Rayleigh-Taylor instability. *Physics of Fluids*, 19(12):1–11, 2007.

[116] R. S. Davis. Equation for the Determination of the Density of Moist Air. *Metrologia*, 29(1):67–70, 1992.

APPENDIX A

TECHNICAL DATA SHEETS AND DRAWINGS

CUSTOMER APPROVAL	
Date	
Signature	

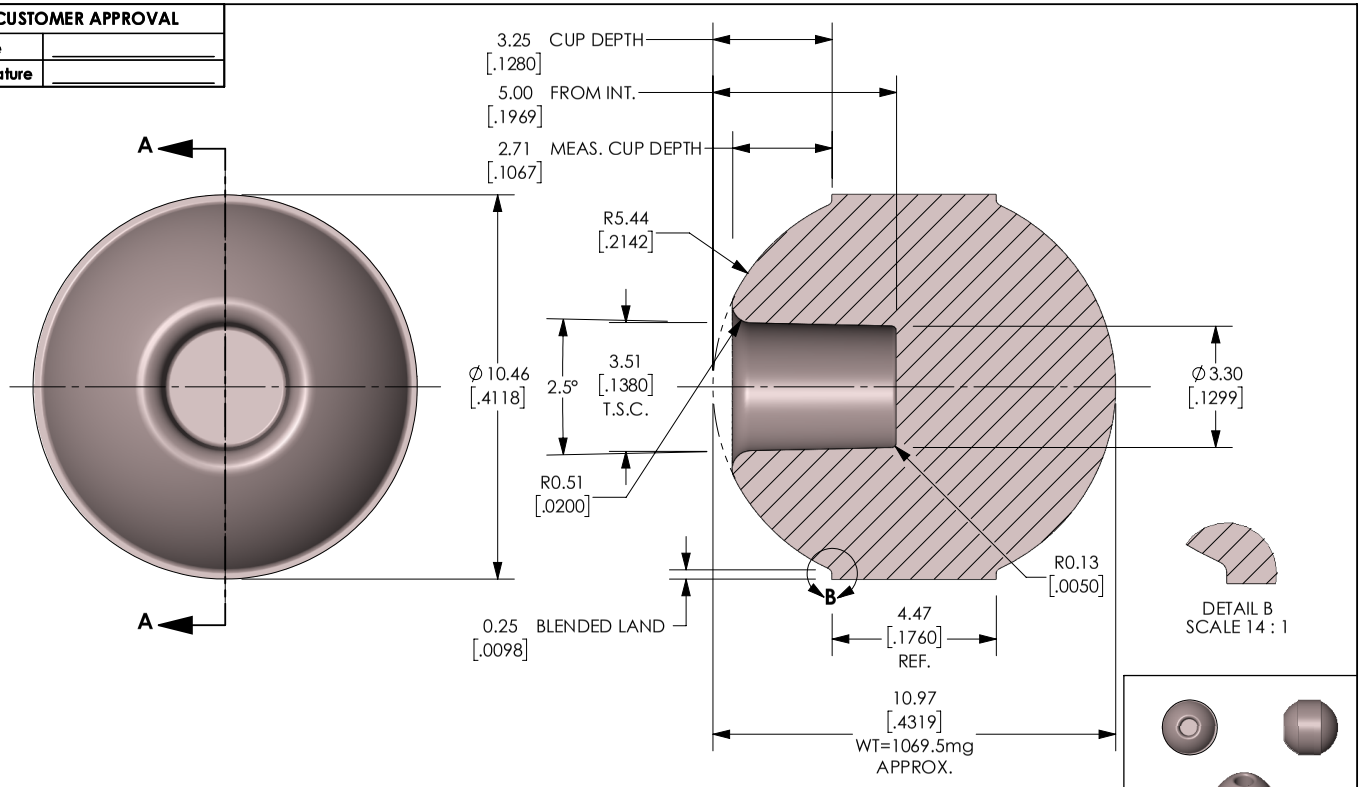

LOWER

NOTE:
TABLET DIMENSIONS ARE NOMINAL TOOL SIZE AND DO NOT INCLUDE TABLET EXPANSION OR CONTRACTION.

ENGINEERING DATA

HOB NUMBER : **194861**

DIE NUMBER :	106211
CUP VOLUME :	144.58 mm³[.00882 in.³]
CUP AREA :	119.11 mm²[.18463 in.²]
PERIMETER:	32.86 mm[1.29374 in.]
DIE HOLE SA:	85.93 mm²[.13319 in.²]

APPR BY: H M DATE: 2/22/2021

TOOLING SIZE DATA (STD)

UPPER TIP SIZE	+.0000/-.0127 [+.0000/-.0005]
LOWER TIP SIZE Ø 10.4292 Ø [.4106]	+.0000/-.0127 [+.0000/-.0005]
DIE SIZE Ø 10.46 Ø [.4118]	+.0127/-.0000 [+.0005/-.0000]

PRODUCT NAME: .

TOLERANCES UNLESS NOTED: DECIMAL TOL: ± .0762[.003] ANGULAR TOL: ± .33° | **UNITS: METRIC [INCHES]** **SCALE: 7:1**

NO.	REVISION	DATE
A	.	.
B	.	.

PUNCH TIP FORCE GUIDE (NATOLI FEA)

PUNCH MATERIAL	MAX. TIP FORCE (kN / US ton)
S7/S1 STEEL	12.9/1.45
440C/D2 STEEL	10.3/1.16
M340 STEEL	11.5/1.29
K340/DC53 STEEL	10.8/1.22

NATOLI ENGINEERING CO., INC.
28 RESEARCH PARK CIRCLE
ST. CHARLES, MO. 63304
PHONE (636) 926-8900 FAX (636) 926-8910
www.natoli.com email: sales@natoli.com

CUSTOMER **NEW MEXICO TECH**

DWN BY L. BALZA | DATE 2/19/2021

DESCRIPTION 10.46mm (.4118") DIA. BALL CONC.

DWG. NO. **194861** | REV. .

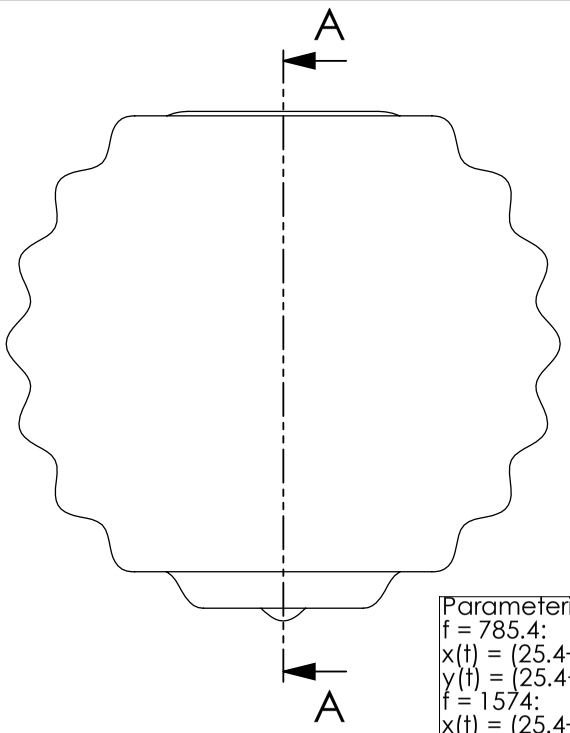

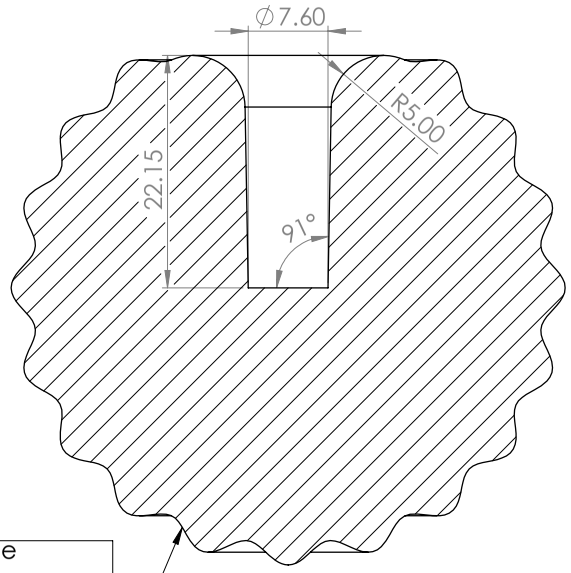

Parameteric profile
f = 785.4:
x(t) = (25.4+cos(20t))*cos(t)
y(t) = (25.4+cos(20t))*sin(t)
f = 1574:
x(t) = (25.4+cos(40t))*cos(t)
y(t) = (25.4+cos(40t))*sin(t)

SECTION A-A

DIMENSIONS ARE IN MILIMETERS

TITLE:

105 g Sphere

SIZE	DWG. NO.	REV
A		
SCALE: 2:1		SHEET 1 OF 1

DO NOT SCALE DRAWING

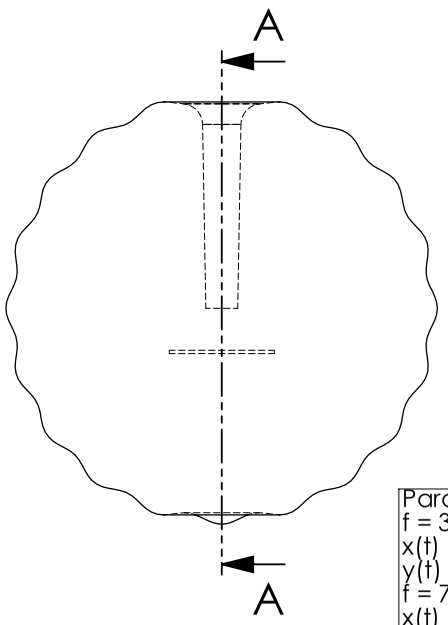

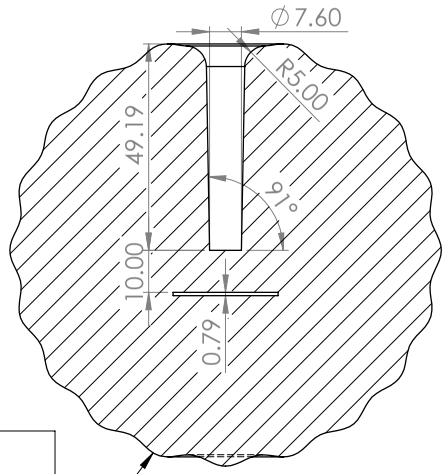

Parameteric profile
f = 384.6:
x(t) = (50.4+cos(20t))*cos(t)
y(t) = (50.4+cos(20t))*sin(t)
f = 769.2
x(t) = (50.4+cos(40t))*cos(t)
y(t) = (50.4+cos(40t))*sin(t)

SECTION A-A

DIMENSIONS ARE IN MILIMETERS

TITLE:

880 g Sphere

SIZE	DWG. NO.	REV
A		
SCALE: 1.25		SHEET 1 OF 1

DO NOT SCALE DRAWING

APPENDIX B

RADIUS DATA AND CHARACTERISTICS LENGTHS

B.1 Characteristic lengths and times

The characteristic lengths and times were calculated using the Wei-Hargather scaling [96]. The scaled radius was computed by:

$$R_c = \left(\frac{E_{HE}}{\rho_0 C_0^2} \right)^{1/3} \tag{B.1}$$

The characteristic time was computed by:

$$t_c = \frac{R_c}{C_0} \tag{B.2}$$

For example, to calculate the scaled time for a 105 g C4 test, the total explosive energy E_{HE} is computed from the explosive mass m_{HE} and specific explosive energy e_{HE}.

$$E_{HE} = (0.105 \text{ kg})(5.86 \text{ MJ/kg}) \tag{B.3}$$

$$= 0.615 \text{ MJ} \tag{B.4}$$

Air density ρ_0 is calculated using equations for moist air from Davis [116]. For the example test, the temperature was 21.4° C, the air pressure was 821.2 hPa, and the relative humidity was 42.3%. This gives an air density of $\rho_0 = 0.968 \text{ kg/m}^3$. The local speed of sound is calculated using:

$$a_0 = \sqrt{\gamma R T_0} \tag{B.5}$$

$$= 343.8 \text{ m/s} \tag{B.6}$$

The characteristic length and time is then calculated.

$$R_c = \left(\frac{(0.615 \text{ MJ})}{(0.968 \text{ kg/m}^3)(343.8 \text{ m/s})^2} \right)^{1/3} \tag{B.7}$$

$$= 1.75 \text{ m} \tag{B.8}$$

$$t_c = \frac{(1.75 \text{ m})}{(343.8 \text{ m/s})} \tag{B.9}$$

$$= 0.0051 \text{ s} \tag{B.10}$$

The characteristic values varied minimally between individual tests of a series. All characteristic values used are tabulated in Tables B.1, B.2, and B.3.

Table B.1: Characteristic lengths and times for PBXN-113 tests

	Test 1	Test 2	Test 3
l_c	2.907	2.907	2.907
t_c	0.0083	0.0083	0.0083

Table B.2: Characteristic lengths and times for perturbed C4 tests

105 g			880 g		
	l_c	t_c		l_c	t_c
Test 1	1.748	0.0050	Test 1	3.507	0.0101
Test 2	1.749	0.0050	Test 2	3.507	0.0101
Test 3	1.749	0.0050	Test 3	3.502	0.0101
Test 4	1.749	0.0050	Test 4	3.502	0.0101
Test 5	1.749	0.0050	Test 5	3.503	0.0101
Test 6	1.750	0.0051	Test 6	3.504	0.0102
Test 7	1.751	0.0051	Test 7	3.505	0.0100
Test 8	1.751	0.0051	Test 8	3.504	0.0100
Test 9	1.752	0.0051	Test 9	3.506	0.0100
Test 10	1.752	0.0051			
Test 11	1.752	0.0051			
Test 12	1.752	0.0050			

Table B.3: Characteristic lengths and times for gram scale tests

	l_c	t_c
Test 1	0.379	0.0011
Test 2	0.379	0.0011

APPENDIX C

PERMISSIONS

A large portion of Section 5.1.1 and Section 5.1.1 is reprinted from Christian Peterson, Veronica Espinoza, and Michael Hargather. Experimental evolution of explosively driven gas clouds in varying confinment, Experiments in Fluids, 63(12):1-11, 2022, Reproduced with permission from Springer Nature.

CHARACTERIZATION OF THE INTERFACE BETWEEN DETONATION PRODUCT GASES AND AMBIENT AIR IN AN EXPLOSION

by

Christian Peterson